Marcio Jorge Teles da Costa

First-principles studies of local structure effects in magnetic materials

Abstract

This thesis focus on the magnetic behavior, from single atoms to bulk materials. The materials considered in this thesis have been studied by computational methods based on ab initio theory, density functional theory (DFT), including treatment of the spin-orbit coupling, non-collinear magnetism, and methods capable of treating disorded systems. Furthermore strongly correlated materials have been investigated using the dynamical mean field theory (DMFT). The uniaxial magnetic anisotropy energy (MAE) of the Fe_2P was investigated using the full-potential linear muffin tin orbital (FP-LMTO) method. Based on a band structure analysis, the microscopical origin of the large magnetic anisotropy found for this system is explained. It is also shown that by straining the crystal structure, the MAE can be enhanced further. This opens up for the possibility of obtaining a room temperature permanent magnet based on the Fe_2P. The spectral properties of Fe impurities in a Cs host have been investigated, for both surface and bulk systems, by means of combination of density-functional theory in the local density approximation and the dynamical mean-field theory (LDA+DMFT), using two different impurity solvers, the Hubbard I approximation (HIA) and the Exact Diagonalization (ED) method. It is shown that noticeable differences can be seen in the unoccupied part of the spectrum for different positions of Fe atoms inside the host. The calculations show good agreement with the experimental photoemission spectra. The stability of the 12-fold metal-phosphorous coordination, existing in the meteorite mineral melliniite has been investigated trough total energy calculations using the coherent potential approximation (CPA) combined with an analysis of the chemical bonds, performed by balanced crystal overlap population (BCOOP). It was shown that its uniquely high metal-phosphorous coordination is due to a balance between covalent Fe-P binding, configurational entropy and a weaker nickel-phosphorus binding. Supported clusters have drawn a lot of attention as possible building blocks for future data storage applications. This topic was investigated using a real space noncollinear formalism where the exchange interactions between Co atoms were shown to be tuned by varying the substrate surface composition. Furthermore the spin dynamics of small Co clusters an a Cu(111) surface have been investigated and a new kind of dynamics, where magnetization switching can be accelerated by decreasing the switching field, has been found. A method for calculating the electronic structure for both ordered and disordered alloys, the augmented space recursion (ASR) method, have been extended to treat non-collinear magnetic order. The method has been used to investigate the energy stability of non-collinear arrangements of MnPt and Mn_3Rh alloys.

In memory of my grandmother Maria.

List of papers

This thesis is based on the following papers, which are referred to in the text by their Roman numerals.

I **Augmented space recursion formulation of the study of disordered alloys with noncollinear magnetism and spin-orbit coupling: Application to MnPt and Mn$_3$Rh**
S. Ganguly, M. Costa, A. B. Klautau, A. Bergman, B. Sanyal, A. Mookerjee and O. Eriksson
Phys. Rev. B 83, 094407 (2011).

II **On the icosahedral metal-phosphorus coordination in melliniite: a gift from the sky for materials chemistry**
K. Kadas, M. Costa, L. Vitos, Y. Andersson, A. Bergman and O. Eriksson
J. Mater. Chem. 22, 14741 (2012).

III **On the large magnetocrystalline anisotropy of Fe$_2$P**
M. Costa, O. Grånäs, A. Bergman, P. Venezuela, P. Nordblad, M. Klintenberg and O. Eriksson
Phys. Rev. B 86, 085125 (2012).

IV **Correlated electronic structure of Fe in Cs**
M. Costa, P. Thunström, I. Di Marco, A. Bergman, A. B. Klautau, and O. Eriksson
In manuscript

V ***Non-Newtonian* magnetization dynamics, a way to accelerate the switching of logical units**
C. Etz, M. Costa, O. Eriksson and A. Bergman
Submited to Nature Nanotechnology

VI **Exchange competition of supported transition metal clusters**
M. Costa, A. B. Klautau, P. Venezuela.
In manuscript

Reprints were made with permission from the publishers.

Contents

1. Introduction

This thesis deals with a more less sparse subjects from bulk (3D) material to adatoms (1D) passing through surfaces (2D) objects. Nevertheless all the work done here is linked by two fields, the quantum mechanical theory of matter and magnetism. The quantum mechanical theory is a very powerful toll to understand nature and one of the most successful theories ever produced. Nevertheless, often when working with Quantum Mechanics one stumbles into situations which are counterintuitive and difficult to have any parallel with classical thinking. In situations like this the mathematical framework gives the support necessary to overcome our reluctance in accepting these new concepts. Unfortunately these quantum mechanical equations are, in most of the cases, impossible to solve. Approximations are unavoidable if one want to solve them.

In this work the density functional theory (DFT) was used. The DFT is a so called *Ab initio* method, and in principle one can calculate the most stable arrangement of Fe atoms by only taking information from the Periodic Table. In practice this it is not so simple, DFT does not work for all possible systems and is important to know the theory and it's applicability. The Quantum Mechanics and DFT will be discussed in chapter 2.

One of the most exciting discoveries from the last century is the transistor, which was conceived and invented in Bell's Laboratory in the late 40's. The transistor is based on a semiconductor, which can be described by the Quantum Mechanics. The invention of the transistor simply changed the modern society and it is responsible for all the electronics gadgets that we use every day, including the computers used to perform the calculations and to write this thesis.

Permanent magnets are fundamental for all modern applications, from wind turbines to computer hard drives. The market of permanent magnets are dominated by the rare-earth based materials and the ferrites. In the beginning of the year 2000 the price of the rare-earth materials was very low. This low price combined with environmental pressure lead to the closure of many mining sites in United States and many other countries, the exception was China, as showed in figure 1.1. Which is a bit contradictory since some of the green energy technologies need rare-earth materials. Such as wind energy, since the more efficient wind turbines uses rare-earth permeant magnets, also electrical cars need an considerable amount of rare-earth compounds. In the last 30 year China

increased the production and now controls something around 97% of the mining. And the price of these commodities skyrocketed in the last few year, due to a combination of demand and exports control done by China.
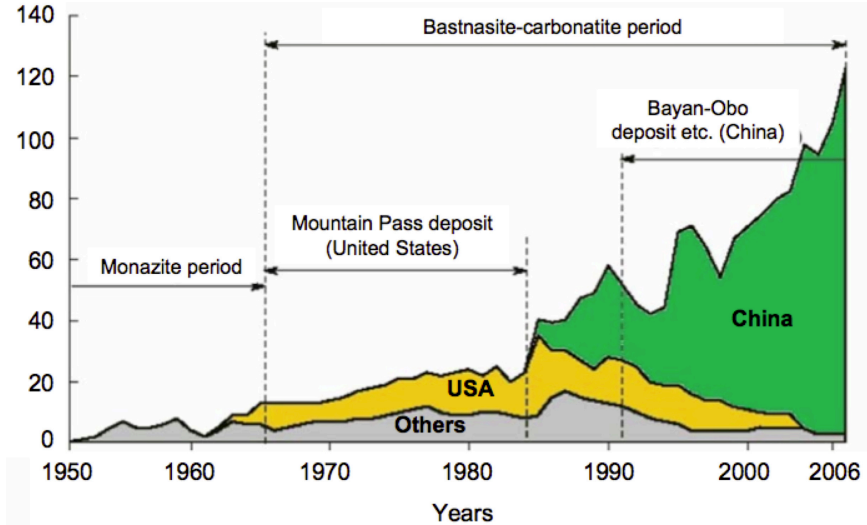
Figure 1.1. The Chinese market share increase, particularly since 2002, when the US mine was closed due to environmental problems and low competitiveness because of low Chinese prices. Adapted from [1]

With this scenario much effort is being done to find a solution to the rare-earth problem, not only in the permanent magnet area. In chapter 7 we investigate the microscopical origin of the large magneto anisotropy energy (MAE), which is one the characteristics of hard permanent magnets, of the di-iron phosphide (Fe_2P). We also show how one can influence the MAE, in a related topic to the iron-pnictides. In chapter 8, we investigate the origin of an unusual twelve-fold coordination phosphourus-metal bond. This was observed in a meteorite named melliniite, found in North-west Africa. The problem was addressed by total energy calculations and also by analysis of the chemical bonds in this compound.

In chapter 6 the DFT failure to treat strong correlated materials is discussed. As will be mentioned a couple of times in this thesis, the DFT is a very successful theory. The failure is not on the DFT itself but on the approximations to include the exchange and correlation effects as the local density approximation (LDA). There are several initiatives to correct this problem in this work we use the so called dynamical mean-field theory (DMFT). The LDA+DMFT scheme is used to investigate the spectral properties of Fe impurities in a Cs host.

We also investigate the magnetization dynamics of small Co clusters (100 atoms) supported on a Cu surface. This is an interesting subject since this could be the next technology for data storage.

Sometimes is necessary to address the disorder that can arise in solid sate systems. For example it is not uncommon to see chemical disorder in binary alloys. We assisted in the implementation of a method to treat these chemical disorders in the presence of noncollinear magnetism, the so called augmented space recursion.

2. Theoretical Background

In the next few lines we will follow some of the facts that contributed to the creation of Quantum Mechanics. In 1905 Albert Einstein published a paper on the photoelectric effect [2], where he proposed the quantization of light waves. This is the so called light particle-wave paradox. In atomic physics the theories to explain the atom stability had many problems. In particular the collapse of electronic orbits predicted by Maxwell's electromagnetic theory. The enigma could be solved (by Niels Bohr) only by postulating the "stationary orbits". Following Einstein's work, in 1924 Louis de Broglie proposed that any moving particle, i.e. electrons, neutrons, etc, is associated with a wave [3], speculating about the existence of an analogous light particle-wave paradox. In 1926 a major breakthrough was achieved by Erwin Schrödinger, proposing an equation, named after him, to describe the behavior of matter waves: [4]

$$H\Psi = E\Psi \tag{2.1}$$

Despite the success of the Schrödinger's equation for simple systems, solving it for more complex systems, like molecules, solids, etc, was a difficult task and still is, even today. When P. M. Dirac declared that chemistry would have ended, if one was able to solve the Schrödinger equation for a generic system, he surely knew the difficulties of such a problem. The difficulty remains on the many-body nature of the problem, in principle the movement of one electron is affected by all the other electrons and vice-versa.

2.1 The Fully Relativistic Quantum Mechanics

When the Schrödinger equation was proposed, Einstein's relativity was already accepted. It was natural to try to connect these two theories in one framework. One of the first attempt was made by Klein and Gordon [5], by using the relativistic energy dispersion relation $E^2 = p^2c^2 + m^2c^4$ directly into the Schrödinger equation. However their description was a second order differential equation both in time and space, therefore leading to negative probabilities. Nevertheless their equation successfully describes spinless particles. In 1928 P. A. Dirac proposed his famous equation which accounted for the magnetism (spin) and relativistic effects [6], and also made the astonishing prediction of the existence of antiparticles. This famous equation reads

$$i\hbar\frac{\partial}{\partial_t}\Psi = H_D\Psi, \tag{2.2}$$

where H_D is given by

$$H_D = c\boldsymbol{\alpha}\cdot\boldsymbol{p} + \beta mc^2 + V \tag{2.3}$$

and c is the velocity of light in the vacuum, **p** is the momentum operator, m is the mass of the particle, V is the potential acting on the particle, $\boldsymbol{\alpha}$ and β are 4x4 matrices which can be written in terms of the Pauli matrices. The time dependence is left aside and only spacial dependency is treated. The solution of Eq.(2.2) is a four-component spinor

$$\psi = \begin{pmatrix} \phi \\ \chi \end{pmatrix} \tag{2.4}$$

with $|\chi\rangle$ and $|\phi\rangle$ state vectors in the Hilbert space of the spin. A matrix representation of the time independent Dirac equation takes the form

$$\begin{pmatrix} mc^2 + V(\vec{r}) & \vec{\sigma}\cdot\vec{p} \\ \vec{\sigma}\cdot\vec{p} & -mc^2 + V(\vec{r}) \end{pmatrix}\begin{pmatrix} \phi \\ \chi \end{pmatrix} = \epsilon\begin{pmatrix} \phi \\ \chi \end{pmatrix}, \tag{2.5}$$

so one obtains coupled equations for ϕ and χ. We do not intend to obtain the formal solution of Eq.(2.5), as one can find it in several references [7; 8]. However it is interesting to look for conserved quantities of the Hamiltonian H_D, particularly the orbital angular momentum $\vec{L}$ and spin operator $\vec{S}$. Using Einstein's notation the $\vec{L}$, $\vec{S}$ and H_D can be written as

$$L^i = -i\epsilon_{ijk}r^j\partial_k \tag{2.6}$$

$$S^i = \frac{1}{2}\gamma^5\alpha_i \tag{2.7}$$

$$H_D = -ic\alpha_l\partial_l + \beta mc^2 + V(\vec{r}) \tag{2.8}$$

where ϵ_{ijk} is the Levi-civita symbol[1] and γ^5 is a 4x4 matrix. We assumed that V is a central potential. Noether's theorems assures that a given operator is a constant of motion, if the operator does not change the action, e.g. $[\hat{A}, \hat{H}] = 0$. So let us compute the commutator of the orbital angular momentum and the spin operators with the Dirac Hamiltonian, where one can write

$$[L^i, H_D] = [-i\epsilon_{ijk}r^j\partial_k, -ic\alpha_l\partial_l]. \tag{2.9}$$

---

[1]$\epsilon_{ijk} = -1(1)$ for an even (odd) permutation of (123) and zero if $(i = j, i = k, j = k)$

From Eq.(2.8) the only nontrivial commutator will come from the first term of the right hand side. The other two will commute trivially, and therefore

$$[-i\epsilon_{ijk}r^j\partial_k, -i\alpha_l\partial_l] = -\underbrace{\epsilon_{ijk}r^j\alpha_l\partial_k\partial_l}_{=0} + \underbrace{\alpha_l\partial_l\epsilon_{ijk}r^j\partial_k}_{=\alpha_l\epsilon_{ijk}\delta_{lj}\partial_k} \tag{2.10}$$

$$[L^i, H_D] = \epsilon_{ijk}\alpha_j\partial_k. \tag{2.11}$$

Also for S^i the last two terms of Eq.(2.8) commute trivially, leading to

$$\begin{aligned} [S^i, H_D] &= -\frac{i}{2}[\gamma^5\alpha_i, \alpha_l]\partial_l \\ &= -\frac{i}{2}\gamma^5\underbrace{[\alpha_i, \alpha_l]}_{=2i\epsilon_{ijk}\alpha_k}\partial_l + \underbrace{[\gamma^5, \alpha_l]}_{=0}\alpha_i\partial_l \\ &= -\epsilon_{ikl}\alpha_k\partial_l. \end{aligned} \tag{2.12}$$

As a result neither $\vec{L}$ or $\vec{S}$ are good "quantum states". Nevertheless the total angular momentum $\vec{J} = \vec{S} + \vec{L}$ is a good "quantum state".

$$\begin{aligned} [J^i, H_D] &= [S^i, H_D] + [L^i, H_D] \\ &= -\epsilon_{ikl}\alpha_k\partial_l + \epsilon_{ijk}\alpha_j\partial_k \\ &= 0. \end{aligned} \tag{2.13}$$

Before proceeding, let us define a rotation operator. Infinitesimal rotations of an angle δ_θ around an axis $\hat{e}$ in a three dimensional space are defined as

$$U_R = \mathbb{1} - \frac{i}{\hbar}\delta_\theta\hat{e}\cdot\vec{\mathcal{J}} \tag{2.14}$$

where $\mathcal{J}_x$, $\mathcal{J}_y$ and $\mathcal{J}_z$ are the components of $\vec{\mathcal{J}}$ and are called generators of infinitesimal rotations. Their commutations relations are given by

$$[\mathcal{J}_i, \mathcal{J}_j] = i\hbar\epsilon_{ijk}\mathcal{J}_k, \tag{2.15}$$

which correspond to the commutations relations of an angular momentum, so one can construct the spin rotational operator by making $\vec{\mathcal{J}} = \vec{S}$ in Eq.(2.14) and integrating over the infinitesimal angular variations one obtains

$$U_S = exp\left(-\frac{i}{\hbar}\theta\hat{e}\cdot\vec{S}\right). \tag{2.16}$$

The commutator between the spin rotation operator and the Dirac Hamiltonian $[U_S, H_D]$ would be equal to the commutator $[\vec{S}, H_D]$, which was

shown to be not zero. This implies that in the Dirac equation the spin rotational symmetry is broken, only the total angular momentum is rotationally invariant. Taking the nonrelativistic limit, the Dirac Hamiltonian can be written as [7]

$$H = \frac{p^2}{2m} + V - \frac{p^4}{8m^3c^2} + \frac{\hbar^2}{8m^2c^2}\nabla^2 V - \frac{\hbar}{4m^2c^2}\vec{\sigma} \cdot \vec{p} \times \vec{\nabla} V \qquad (2.17)$$

where the last term of Eq.(2.17) is the so called spin-orbit coupling. For a spherical potential it can be rewritten as

$$H_{ls} = \frac{1}{2m^2c^2}\xi\vec{L}.\vec{S}, \qquad (2.18)$$

where ξ is named the spin-orbit coupling constant. In general, for $3d$ compounds it is common to introduce H_{ls} as a perturbation, since the band energies are, generally orders of magnitude larger than ξ. Typical values of ξ for the late $3d$ metals are 0.05 eV. The spin-orbit interaction is responsible for the symmetry breaking discussed above and therefore is of central importance for permanent magnets. We will continue this discussion in chapter 7, where the magnetocrystalline anisotropy the Fe_2P bulk is calculated.

2.2 The Many-Body Problem

Let us elaborate more on the Hamiltonian describing a solid. A solid can be described by the following Hamiltonian. Including both electrons and nuclei, we can write down

$$\begin{aligned}
\hat{H} = &-\sum_i \frac{\hbar^2}{2M_i}\nabla^2_{\vec{R}_i} + \frac{1}{2}\sum_{i \neq j} \frac{Z_i Z_j e^2}{|\vec{R}_i - \vec{R}_j|} - \sum_{i,j} \frac{e^2 Z_j}{|\vec{r}_i - \vec{R}_j|} \\
&- \sum_i \frac{\hbar^2}{2m_e}\nabla^2_{\vec{r}_i} + \frac{1}{2}\sum_{i \neq j} \frac{e^2}{|\vec{r}_i - \vec{r}_j|}
\end{aligned} \qquad (2.19)$$

where the $\vec{r}_i$ are the positions of the electrons, $\vec{R}_i$ and Z_i are the positions and atomic number of the nuclei, $\hbar$ is Planck's constant and e, m_e are electron's mass and charge respectively. The first approximation to be made is to decouple the electronic and ionic degrees of freedom, this is called the Born-Oppenheimer Approximation [9; 10]. The Physical justification behind it is that the nuclei are much heavier than electrons, so their kinetic energy can be neglected. One can rewrite Eq.(2.19) as:

$$\hat{H} = \hat{T}_e + \hat{V}_{ee} + \hat{V}_{ext} + E_{NN} \qquad (2.20)$$

where $\hat{T}_e$ is the kinetic energy of the electrons, $\hat{V}_{ee}$ is the electron-electron interaction, $\hat{V}_{ext}$ is electron-nuclei interaction and the last term E_{NN} is the nuclei-nuclei coulomb interaction, which enters as a fixed energy in this frozen nuclei approximation. Already at the first stages of Quantum Mechanics it was realized that solving Eq.(2.19) was a difficult task, mainly due to its many-body nature; consider that even in classical physics a many-body problem has no analytical solution. The term V_{ee} represents the major difficulty, due to its many-body nature. Decoupling the electronic movement, similarly to what was done for the electronic and nuclear degrees of freedom, would lead to a poor description of the cohesive energies, bond distances, etc.

2.3 Density Functional Theory

To solve the Schrödinger or Dirac equations one needs, in principle, to calculate the many body wave function Ψ. The number of constituents in real solids are in the order of 10^{23}, and solving the previous equations for such a big system is in fact an impossible task. The density functional theory (DFT) changes the perspective from the wave function to the electron density. The DFT has proven very successful and nowadays is a well established theory, used in many fields from physics to chemistry passing throughout the material engineering. Several reviews on the theoretical framework and applications of DFT are available [8; 11; 12**?**]. In the following we will discuss some of these fundamental ideas.

2.3.1 Hartree-Fock Method

We start with discussing the Hartee-Fock (HF) method as some of its basic ideas are used to construct the DFT formalism. The HF method consists of approximating the many-body wave function (Ψ) by an appropriate product of single particle wave function (ϕ). By appropriate we mean, that the product of ϕ must satisfy certain rules, i.e. for fermionic particles the wave function must be anti-symmetric. The way to construct such a product is to use the so called Slater determinant:

$$\Phi(\mathbf{x_1}, \ldots, \mathbf{x_N}) = \frac{1}{(N!)^{1/2}} \begin{vmatrix} \phi_1(\mathbf{x_1}) & \phi_1(\mathbf{x_2}) & \ldots & \phi_1(\mathbf{x_N}) \\ \phi_2(\mathbf{x_1}) & \phi_2(\mathbf{x_2}) & \ldots & \phi_2(\mathbf{x_N}) \\ \vdots & \vdots & \vdots & \vdots \\ \phi_N(\mathbf{x_1}) & \phi_N(\mathbf{x_2}) & \ldots & \phi_N(\mathbf{x_N}) \end{vmatrix} \quad (2.21)$$

where $\mathbf{x_i}$ denotes the spin (σ_i) and position ($\mathbf{r_i}$) coordinates and $\phi_i(x_i) = \psi(\mathbf{r_i})\alpha(\sigma_i)$. Using the Dirac notation one can write the energy of a given system as

$$E = \langle \Psi | \mathcal{H} | \Psi \rangle \tag{2.22}$$

where $\mathcal{H}$ is given by Eq.(2.20), disregarding the nucleus-nucleus interaction. The energy minimum (E_{gs}) would only be obtained for the many-body ground state wave function (Ψ_{gs}), any other choice for the wave function will produce a higher energy. The HF strategy is to substitute Ψ_{gs} by Φ in Eq.(2.22) and minimize the energy using the Euler-Lagrange procedure. With respect to variations in $\psi^*(\mathbf{r})$ one obtains

$$\left(-\frac{\hbar^2}{2m}\nabla^2 + V_{ext}(\mathbf{r}) \right)\psi_i(\mathbf{r}) + \sum_{j=1}^{N} \int \psi_j^*(\mathbf{r}')\psi_j(\mathbf{r}')\frac{e^2}{|\mathbf{r}-\mathbf{r}'|}d\mathbf{r}'\psi_i(\mathbf{r})$$

$$-\sum_{j=1}^{N} \int \psi_j^*(\mathbf{r}')\psi_i(\mathbf{r}')\frac{e^2}{|\mathbf{r}-\mathbf{r}'|}d\mathbf{r}'\psi_j(\mathbf{r})\delta_{s_i s_j} = \epsilon_i\psi_i(\mathbf{r}). \tag{2.23}$$

One can define the Hartree $V_H^i(\mathbf{r})$ and the exchange $V_X^i(\mathbf{r})$ potentials for the i-th particle as

$$V_H^i(\mathbf{r}) = \sum_j \int |\psi(\mathbf{r}')|^2 \frac{e^2}{|\mathbf{r}-\mathbf{r}'|}d\mathbf{r}' \tag{2.24}$$

$$V_X^i(\mathbf{r}) = -\sum_j \int \psi_j^*(\mathbf{r}')\psi_i(\mathbf{r}')\frac{e^2}{|\mathbf{r}-\mathbf{r}'|}d\mathbf{r}'\delta_{s_i s_j}. \tag{2.25}$$

Some comments here are necessary: the Hartree potential is local and is equal to the Coulomb potential due to the charge distribution of all other electrons than i, whereas the exchange potential is non-local and acts on parallel spins. The exchange potential arises from anti-symmetrization of the wave function, and has an intimate relation to the Pauli exclusion principle. Furthermore it is the source of ferromagnetic behavior, since it can break the symmetry (spontaneously) for different spin directions. With this definition one can recast the eigenvalue problem as

$$\left[-\frac{\hbar^2}{2m}\nabla^2 + V_{eff}^i(\mathbf{r}) \right]\phi_i(\mathbf{r}) = \epsilon_i\phi_i(\mathbf{r}) \tag{2.26}$$

where $V_{eff}^i(\mathbf{r})$ is given by

$$V_{eff}^i(\mathbf{r}) = V_{ext}^i(\mathbf{r}) + V_H^i(\mathbf{r}) + V_X^i(\mathbf{r},\mathbf{r}'). \tag{2.27}$$

The HF method is simpler than the original problem, but still cumbersome to solve, as the size of the Slater determinant increases very fast

with the number of electrons. Even with modern computational algorithms, the HF method is mostly used only for small systems. Another drawback of the method is the absence of electronic correlation.

2.3.2 Hohenberg-Kohn Theorems

The first attempt to formulate a theory based on the density, rather than the wave function, was done by Thomas and Fermi [13; 14] in 1927. In their approach both the electronic exchange and correlations are completely missing. This crude approximation leads to the failure in calculating the cohesive energy of molecules, bond distances and so on. Nevertheless the possibility of using the electronic density as the fundamental quantity is very attractive. The usual thinking is: from a potential ($\hat{V}$) a Hamiltonian ($\hat{H}$) can be defined and used in a Schrödinger equation to obtain a wave function (Ψ) which finally leads to a density (n). This way of thinking is schematically represented in Eq.(2.28):

$$\hat{V} \rightarrow \hat{H} \rightarrow \Psi \rightarrow n \tag{2.28}$$

In 1964 Hohenberg and Kohn [15] announced two theorems that rigorously define the basis for the DFT. The first theorem asserts that the density univocally defines the external potential, apart from a trivial constant:

Theorem 1 *For any system of interacting particles subjected to an external potential $V_{ext}(\vec{r})$, the ground state density $n_0(\vec{r})$ univocally determines $V_{ext}(\vec{r})$, except for a trivial constant.*

Proof The proof will be done by *Reductio ad absurdum*. Suppose two external potentials $\hat{V}_{ext}^1$ and $\hat{V}_{ext}^2$, which differ by more than a constant, and result in two different Hamiltonians $\hat{H}^1$ and $\hat{H}^2$ with ground state wave functions given by Ψ^1 and Ψ^2, respectively. Let us suppose that Ψ^1 and Ψ^2 lead to an equal density $n_0(\vec{r})$. We are assuming that these states are non-degenerate, for the degenerate case see Ref. [16]. From the definition of the ground state we have that

$$E^1 = \langle \Psi^1 | H^1 | \Psi^1 \rangle < \langle \Psi^2 | H^1 | \Psi^2 \rangle \tag{2.29}$$

with some algebra we have that

$$E^1 = \langle \Psi^1 | H^1 | \Psi^1 \rangle < \langle \Psi^2 | H^1 | \Psi^2 \rangle + \langle \Psi^2 | H^2 - H^2 | \Psi^2 \rangle \tag{2.30}$$

$$E^1 < \langle \Psi^2 | H^2 | \Psi^2 \rangle + \langle \Psi^2 | H^1 - H^2 | \Psi^2 \rangle \tag{2.31}$$

20

$$E^1 < E^2 + \int d^3r [V_{ext}^1(\vec{r}) - V_{ext}^2(\vec{r})] n_0(\vec{r}). \qquad (2.32)$$

Analogously for E^2 we have

$$E^2 < E^1 + \int d^3r [V_{ext}^2(\vec{r}) - V_{ext}^1(\vec{r})] n_0(\vec{r}) \qquad (2.33)$$

Summing Eq.(2.32) and Eq.(2.33) one gets,

$$E^1 + E^2 < E^1 + E^2 \qquad (2.34)$$

which leads to a contradiction, therefore denying the proposition and prooving the theorem.

The second theorem asserts the existence of a total energy functional of the density E[n] which is minimized, globally, by the ground state density:

$$E_{HK}[n] = F_{HK}[n] + V_{ext}[n] \qquad (2.35)$$

where $F_{HK}[n]$ is the Hohenberg-Kohn functional and is the sum of kinetic and internal energies (electron-electron interaction): it is important to notice that $F_{HK}[n]$ functional is independent on the external potential, e.g. is material independent.

$$F_{HK}[n] = T[n] + V_{int}[n] \qquad (2.36)$$

Theorem 2 *For a particular potential V_{ext} an universal energy functional $E[n]$ can be defined. The ground state energy is the global minimum of this functional, with the particle number constrained. The density that minimizes this functional is the exact ground state density $n_0(\vec{r})$.*

Proof Consider a Hamiltonian H , which has ground state wave function Ψ_{gs} and a ground stated density n_{gs}. The total energy for H is given by

$$E_{gs}[n_{gs}] = \langle \Psi_{gs} | H | \Psi_{gs} \rangle. \qquad (2.37)$$

The expectation value of H with respect to any trial function Ψ, which is univocally determined by a density n, will produce a higher energy value than a ground state wave function Ψ_{gs}, for a non-degenerate ground state:

$$E_{gs}[n_{gs}] = \langle \Psi_{gs} | H | \Psi_{gs} \rangle \le \langle \Psi | H | \Psi \rangle. \qquad (2.38)$$

Applying a minimization procedure to the energy functional Eq.(2.38) one will obtain the ground state density n_{gs}.

The two Hohhenberg-Kohn theorems allow for a new schematic representation, where the density is the basic quantity:

$$n \to \hat{V} \to \hat{H} \to \Psi. \tag{2.39}$$

Notice that the exact form of $F_{HK}[n]$ is unknown, implying that one must make approximations in order to determine the electronic density through the Euler-Lagrange minimization procedure

$$\delta \left[E[n(\vec{r})] - \mu \int n(\vec{r}) d^3 r \right] = 0 \tag{2.40}$$

under the constraint

$$N = \int n(\vec{r}) d^3 r = constant \tag{2.41}$$

2.3.3 Kohn-Sham Equations

In 1965 Kohn and Sham [17] used the two Hohenberg-Kohn theorems in order to propose a practical approach for the minimization procedure in Eq.(2.40). They suggested to explicitly write the known terms of the energy functional $F_{KS}[n]$:

$$E[n] = V_{ext}[n] + T[n] + U[n] \tag{2.42}$$

with

$$V_{ext}[n] = \int V_{ext}(\vec{r}) n(\vec{r}) d^3 r. \tag{2.43}$$

Now one can substitute the sum of the true kinetic energy $T[n]$ and Coulomb interaction $U[n]$ by its non-interacting electronic version $T_S[n]$ and $U_H[n]$ plus an unknown term $E_{xc}(n)$, called exchange and correlation functional. We can rewrite

$$E[n] = V_{ext}[n] + T_S[n] + U_H[n] + E_{xc}[n] \tag{2.44}$$

where $E_{xc}[n]$ contains all the energetic contributions beyond the non-interacting system. Substituting Eq.(2.44) into Eq.(2.40). We get

$$\int \delta n(\vec{r}) \left[\frac{\delta V_{ext}}{\delta n} + \frac{\delta T_S}{\delta n} + \frac{\delta U_H}{\delta n} + \frac{\delta E_{xc}}{\delta n} - \mu \right] d^3 r = 0 \tag{2.45}$$

and with some algebra

$$\int \delta n(\vec{r}) \left[V_{ext}(\vec{r}) + \frac{\delta T_S}{\delta n} + \int \frac{n(\vec{r'}) d^3 r'}{|\vec{r} - \vec{r'}|} + \frac{\delta E_{xc}}{\delta n} - \mu \right] d^3 r = 0. \tag{2.46}$$

$$v^{KS}(\vec{r}) = V_{ext}(\vec{r}) + \int \frac{n(\vec{r'}) d^3 r'}{|\vec{r} - \vec{r'}|} + v_{xc}(\vec{r}) \tag{2.47}$$

defining $v_{xc}(\vec{r}) = \delta E_{xc}/\delta n$, the minimization condition is

$$v^{KS}(\vec{r}) + \frac{\delta T_S}{\delta n} = \mu \tag{2.48}$$

which is the condition for non-interacting particles under the action of the potential v^{KS}, called Kohn-Sham potential. A Schrödinger like equation can be written as

$$\left[-\frac{1}{2}\nabla^2 + v^{KS}(n) \right] \phi_i(\vec{r}) = \epsilon_i \phi_i(\vec{r}) \tag{2.49}$$

where the $\phi(\vec{r})$ are the single particle orbitals and the electron density is given by

$$n(\vec{r}) = \sum_i^N |\phi_i(\vec{r})|^2. \tag{2.50}$$

The Eq.(2.49) is the famous Kohn-Sham equations. Notice that the inter-dependence of v^{KS} and $n(\vec{r})$ calls for a *self-consistent* solution. From an initial density $n^i(\vec{r})$ one computes the Kohn-Sham potential and solves the KS equation, obtaining the single particle orbitals $\phi_i(\vec{r})$ and then a new density $n^{i+1}(\vec{r})$. This process goes on until the difference between two consecutive densities is smaller than a given convergence criterion (λ), i.e. $|n^i(\vec{r}) - n^{i+1}(\vec{r})| < \lambda$.

2.3.4 Exchange and Correlation Functional

As far as the solution to the Hamiltonian of Eq.(2.20) is concerned, no approximations have been performed. We simply sum up all the unknown interactions in an energy functional of the density $E_{xc}[n]$. In practice one needs either to know the exact form of the exchange and correlational functional or find suitable approximations. For suitable we mean accurate, computationally feasible and physically transparent. Notice that even if one knew the exact form of $E_{xc}[n]$ the Kohn-Sham equations would end up to have the same complexity level of the original problem. In the following section we will discuss the two most popular approximations for $E_{xc}[n]$.

2.3.5 Local Density Approximation

The Local Density Approximation (LDA) was proposed by Kohn and Sham in their original paper. It is defined as

$$E_{xc}[n] = \int n(\vec{r})\epsilon_{xc}(n)d^3r \tag{2.51}$$

where $\epsilon_{xc}(n)$ is the exchange and correlation density of the homogeneous electrons gas. The XC functional for a given density, in a volume V, is approximate by the integrated XC density of the homogeneous electrons gas with the same density. This seems to be a very crude approximation but as pointed out by Kohn and Sham solids are close to the limit of the homogeneous electron gas. In that limit a local approximation as Eq.(2.51) is valid. One can write the XC density $\epsilon_{xc}(n)$ as a sum of exchange $\epsilon_x(n)$ and correlation $\epsilon_c(n)$

$$\epsilon_{xc}(n) = \epsilon_x(n) + \epsilon_c(n). \qquad (2.52)$$

For the homogeneous electron gas one can obtain an analytical solution for the exchange term. The more complicated correlation term can be computed by quantum Monte-Carlo (QMC) calculations and reacted in a parametrized form [18; 19]. One would expected that LDA should not work for systems where the density is rapidly varying, but even in this regime LDA has often proven to give very good results. One can easily extend the above treatment for spin polarized systems, and obtain the Local Spin Density approximation (LSDA).

2.3.6 Generalized Gradient Approximation

Another approach is the so called generalized gradient approximation (GGA) where one includes non-local (semi-local) terms to take into account the inhomogeneity in the electronic density, the functional form of the GGA is

$$E_{xc}[n, \vec{\nabla}n] = \int n(\vec{r}) f_{xc}(n, |\vec{\nabla}n|) d^3 r. \qquad (2.53)$$

The generalized form of the functional is constructed in order to reproduce some of the LDA properties that was known to be the reason for its success. There are various forms to construct such a functional. A very used one is due to Perdew *et. al.* [20]. In general GGA improves the chemical bond over LDA, as for the spin and orbital moment they give very similar results.

3. Computational Aspects

In this chapter the computational aspects of the solution of the Kohn-Sham equations are treated in more details.

3.1 Basis Set

A straightforward way of solving differential equations, such as the Kohn-Sham equations, is to expand their solution in a given basis, leading to the following equation:

$$\hat{H}^{KS} \sum_j c_j |\psi_j\rangle - \epsilon_i \sum_j c_j |\psi_j\rangle = 0 \tag{3.1}$$

where the KS wave functions, Ψ_i are expanded in terms of basis functions ψ_j, and ϵ_i are the corresponding eigenvalues. In principle an infinite number of basis functions would be necessary to span the whole Hilbert space formed by the solutions of the KS equation. In practice one needs to truncate the series at some point and the number of basis states necessary to properly describe the problem is, obviously, related to how the ψ_j are constructed. Before going into the details of the basis set, we notice that the Eq.(3.1) can be written in a more convenient form, by multiplying the equation from the left by $\langle \psi_l |$:

$$\sum_j c_j [\langle \psi_l | \hat{H}^{KS} | \psi_j \rangle - \epsilon_i \langle \psi_l | \psi_j \rangle] = 0. \tag{3.2}$$

If $H_{lj} = \langle \psi_l | \hat{H}^{KS} | \psi_j \rangle$ and $O_{lj} = \langle \psi_l | \psi_j \rangle$ are the hamiltonian and the overlap matrix elements, respectively, then Eq.(3.2) becomes

$$\sum_j c_j (H_{lj} - \epsilon_i O_{lj}) = 0. \tag{3.3}$$

The above equation defines a secular equation, where the eigenvalues can be determined by

$$\det |H_{lj} - \epsilon_i O_{lj}| = 0. \tag{3.4}$$

The procedure to obtain the eigenvalues stated in this format is well suited for modern computational algorithms, using linear algebra packages such as LAPACK or BLAS. Once the ϵ_i's are determined the coefficients c_j can be obtained, i.e the wave function Ψ_i can be constructed.

There are several choices for the basis functions such as linear combination of atomic orbitals (LCAO) and linear combination of augmented plane waves (LAPW)[8]. Our main focus will be on the so called muffin-tin orbital (MTO) basis.

3.1.1 Linear Muffin-tin Orbital

A solid can be viewed as an array of atoms. A natural choice to describe the action of an ionic electrostatic potential is to divide the space into two regions: a spherical region centered on the ions, called muffin-tin sphere (MT) and an interstitial region, between the MT. Inside the MT an electron is subjected to an atomic-like potential, in DFT the Kohn-Sham potential (V_{KS}), while in the interstitial region a constant potential (V_0) is defined. The assumption of a flat potential in the interstitial region is quite reasonable, since the Coulomb potential due to the ions is screened by the charge inside the MT, and also partially by the interstitial charge itself. Therefore we have

$$
V(r) = \begin{cases} V_{KS}(r) & r < S \\ \\ V_0 & r > S \end{cases}
\tag{3.5}
$$

where S is the radius of the sphere centered at the site $\mathbf{R}$, as defined in Fig.(3.1). This approximation is called atomic sphere approximation (ASA) and is very successful in describing closed packed system, where the sum of the muffin-tin volumes is almost equal to the solid volume. We are considering only non-overlapping muffin-tin spheres. Nevertheless the muffin-tin approach does not imply any structural limitation. For open structures or depending on the level accuracy desired one should take a step further and consider a non-constant potential in the interstitial region, which lead to the so called Full Potential (FP) approach.
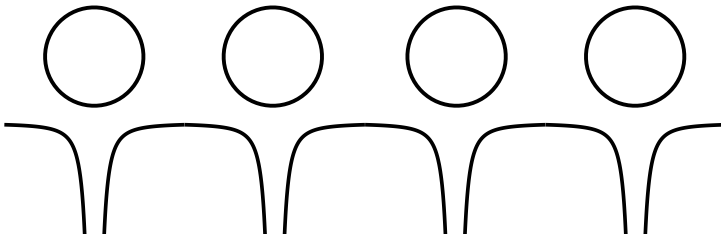

Figure 3.1. Representation of the muffin-tin sphere of radius S, centered at the atoms. The interstitial region is the space between the muffin-tin spheres. The lower panel shows the potential inside the muffin-tin (V_{KS}) and the constant potential in the interstitial region (V_0).

The basis set in the two approaches differs only in the interstitial region, as their definition is exactly the same, within the two muffin-tin spheres.

3.1.2 Muffin-tin Basis Set

The strategy is to construct a basis function able to describe the electron density inside the MT and interstitial region. A natural choice inside the muffin-tin is to take solutions of the radial Schrödinger equation

$$\left[\frac{\hbar^2}{2m}\left(\frac{d^2}{dr^2} - \frac{l(l+1)}{r^2} + V_{KS}(r) - \epsilon\right)\right]r\phi_l(r,\epsilon) = 0 \qquad (3.6)$$

multiplied by spherical harmonics. In the interstitial region the electrons can be seen as "free electrons" under a constant potential V_0, and therefore we can use solutions to the Helmholtz equation

$$\left[\left(\frac{d^2}{dr^2} - \frac{l(l+1)}{r^2} + \kappa^2\right)\right]rf(r) = 0, \qquad (3.7)$$

where κ^2 is given by

$$\kappa^2 = \frac{2m}{\hbar^2}(\epsilon - V_0). \qquad (3.8)$$

The solutions to Eq.(3.7) are spherical Bessel $j_l(\kappa r)$ and Neumann $n_l(\kappa r)$ functions times spherical harmonics. If $\kappa^2 < 0$ the spherical Neumann functions should be substituted by spherical Henkel functions $h_l(\kappa r)$ of first kind ($h_l = n_l - ij_l$), as Neumann functions does not form bound states. A solution can be constructed as

$$\psi_L(\epsilon, \kappa, r) = \mathcal{Y}_{lm}(\hat{r}) \begin{cases} \phi_l(\epsilon, r) & r < S \\ \mathcal{K}_l(\kappa, r) + \mathcal{J}_l(\kappa, r) & r > S \end{cases} \qquad (3.9)$$

the capital index L stands for $\{l, m\}$ quantum numbers. Following Andersen's [21] original formulation we define a modified version of the spherical harmonics, Bessel and Neumann (or Henkel) functions

$$\mathcal{Y}_{lm}(\hat{r}) = i^l Y_{lm}(\hat{r}) \qquad (3.10)$$

$$\mathcal{J}_l(\kappa, r) = \kappa^{-l} j_l(\kappa r) \qquad (3.11)$$

$$\mathcal{K}_l(\kappa, r) = \kappa^{l+1} \begin{cases} n_l(\kappa r) & \kappa^2 > 0 \\ h_l(\kappa r) & \kappa^2 < 0. \end{cases} \qquad (3.12)$$

Imposing continuity and differentiability of Eq.(3.9) everywhere and particularly at the boundary $(r = S)$ one obtains:

$$\psi_L(\epsilon, \kappa, r) = \mathcal{Y}_{lm}(\hat{r}) \begin{cases} \phi_l(\epsilon, r) & r \leq S \\ \mathcal{K}_l(\kappa, r) - cot[n_l(\epsilon)]\mathcal{J}_l(\kappa, r) & r \geq S \end{cases} \qquad (3.13)$$

where the $cot[n_l(\epsilon)]$ is defined as

$$cot[n_l(\epsilon)] = \frac{n_l(\kappa r)}{j_l(\kappa r)} \frac{D_l(\epsilon) - \kappa D_{n_l}(\kappa)}{D_l(\epsilon) - \kappa D_{j_l}(\kappa)} \qquad (3.14)$$

and D_l are the logarithmic derivatives at the sphere boundary. The function ψ_L is not suited to form a basis as for negative energies as it is not normalizable. In fact Bessel functions $j_l(\kappa, r)$ do not form bound states, except for the eigenvalues of the spherical well $(\epsilon = V_0)$, where $cot[n_l(\epsilon)]$ vanishes. Andersen proposed to remove the Bessel function contribution from the partial waves ψ_L:

$$\chi_L(\epsilon, \kappa, r) = \mathcal{Y}_{lm}(\hat{r}) \begin{cases} \phi_l(\epsilon, r) + cot[n_l(\epsilon)]\mathcal{J}_l(\kappa, r) & r \leq S \\ \mathcal{K}_l(\kappa, r) & r \geq S. \end{cases} \qquad (3.15)$$

From this physical picture it is clear that the solutions inside a given muffin-tin, so called "head", is modified by the "tails" of the other atomic sites. Using the expansion theorem one can expand the tail of a given MT centered at site $\mathbf{R}$ around another MT centered at $\mathbf{R}'$, or any other site:

$$N_L(\kappa, \mathbf{r} - \mathbf{R}) = \sum_{L'} B_{L'L}^{\mathbf{R}'\mathbf{R}}(\kappa) \; J_{L'}(\kappa, \mathbf{r} - \mathbf{R}') \qquad (3.16)$$

where $K_L(\kappa, r)$ and $J_L(\kappa, r)$ are the Neumann and Bessel functions times the modified spherical harmonics, respectively. A similar expression can be obtained for the Henkel functions. The $B_{L'L}^{\mathbf{R}'\mathbf{R}}(\kappa)$ are called *structure constants*, and are defined as

$$B_{LL'}^{\mathbf{R}'\mathbf{R}}(\kappa) = 4\pi \sum_{L''} G_{LL'L''} \; N_{L'}^*(\kappa, \mathbf{R} - \mathbf{R}'), \qquad (3.17)$$

where $G_{LL'L''}$ are the Gaunt coefficients. The MTO χ_L is no longer an eigenstate of the Hamiltonian inside a single muffin-tin, as the wave function is modified by the atoms in its vicinity. This is expected since we are dealing with a many-site problem and information about the structure must be taken into account in some way. By this construction the muffin-tin orbitals are normalizable, continuous and differentiable

inside, outside and at the boundaries of the MT. Nevertheless $\chi_L(\epsilon, \kappa, r)$ is energy dependent and this lead to a non-linearity in Eq.(3.2), e.g. increasing the complexity. Moreover the structural constants $B_{L'L}^{\mathbf{R'R}}(\kappa)$ are not really constant since they are energy dependent. These non-linear equations are known as KKR equations. The first step to construct an energy-independent basis is to fix κ, i.e. κ becomes a parameter and ϵ and κ are not interdependent variables anymore. This procedure will introduce errors and will be discussed later. Still the heads of the MTO are energy dependent, so Andersen proposed a Taylor expansion for the solution of the radial Schrödinger equation at an arbitrary energy ϵ_ν:

$$\phi_l(r, \epsilon) = \phi_l(r, \epsilon_\nu) + (\epsilon - \epsilon_\nu)\dot{\phi}_l(r, \epsilon_\nu) \tag{3.18}$$

where $\dot{\phi}_l = \partial\phi/\partial\epsilon$ at a given energy ϵ_ν. This linearization procedure is very convenient since $\phi_l(r, \epsilon_\nu)$ and $\dot{\phi}_l(r, \epsilon_\nu)$ are mutually orthogonal, and also orthogonal to the core states of their own muffin-tin sphere [22]. A independent energy basis must have $\dot{\chi}_L = 0$, to first order in $(\epsilon - \epsilon_\nu)$. Substituting Eq.(3.18) in Eq.(3.20) and imposing continuity and differentiability at the boundaries of the muffin-tin, one obtains the augmented Bessel functions ($\mathcal{J}_L^{aug}$)

$$\mathcal{J}_l^{aug}(\kappa, \mathbf{r}) = \begin{cases} \dfrac{-\dot{\phi}_l(\epsilon_\nu, r)}{\kappa \ \dot{cot}(n_l(\epsilon_\nu))} & r \leq S \\ \\ \mathcal{J}_l(\kappa, r) & r \geq S. \end{cases} \tag{3.19}$$

Augmented Henkel and Neumann functions can be computed in an analogous way and one can finally define an energy independent basis:

$$\chi_L(\epsilon_\nu, \kappa, r) = \mathcal{Y}_{lm}(\hat{r}) \begin{cases} \phi_l(\epsilon, r) + cot[n_l(\epsilon)]\mathcal{J}_l^{aug}(\kappa, r) & r \leq S \\ \\ \mathcal{K}_l^{aug}(\kappa, r) & r \geq S. \end{cases} \tag{3.20}$$

The simplest choice of ϵ_ν, for example the center of the band, already gives good results for most problems. On the other hand tail energies κ should be choosen more carefully, especially if subtle structural properties are under focus.

3.2 Bloch's Theorem

This is one of the most important theorems in solid state physics and it was stated by Bloch in 1929. A crystal can be seen as an ordered arrangement of atoms. Due to the periodicity one can construct vectors ($\vec{a}_i$) that can generate the entire crystal, starting from a primitive unit

cell. These vectors are called Bravais lattice vectors. In a 3-dimensional crystal one can write

$$\vec{R}_j = n_j\vec{a}_1 + m_j\vec{a}_2 + l_j\vec{a}_3, \tag{3.21}$$

where n_j, m_j and l_j are integers that determine the translation index. If an electron is under the action of a potential V at a point $\vec{r}$ it will feel the same potential at $\vec{r} + \vec{R}_j$. The periodicity of the crystal is shared by its potential

$$V(\vec{r} + \vec{R}_j) = V(\vec{r}). \tag{3.22}$$

The Bloch's theorem states that with a potential given by Eq.(3.22), the wave function will show the same periodicity of the potential with a proper phase

$$\psi_{n\mathbf{k}}(\vec{r} + \vec{R}_j) = e^{i\vec{k}\cdot\vec{R}_j}\psi_{n\mathbf{k}}(\vec{r}) \tag{3.23}$$

with that one can define the so called *reciprocal lattice* as

$$\vec{K} = g_1\vec{b}_1 + g_2\vec{b}_2 + g_3\vec{b}_3, \tag{3.24}$$

where g_1, g_2 and g_3 are integers and one can obtain the reciprocal vectors $\vec{b}_i$ by

$$\vec{b}_1 = 2\pi\frac{\vec{a}_2 \times \vec{a}_3}{\vec{a}_1 \cdot (\vec{a}_2 \times \vec{a}_3)}, \tag{3.25}$$

$$\vec{b}_2 = 2\pi\frac{\vec{a}_3 \times \vec{a}_1}{\vec{a}_1 \cdot (\vec{a}_2 \times \vec{a}_3)}, \tag{3.26}$$

$$\vec{b}_3 = 2\pi\frac{\vec{a}_1 \times \vec{a}_2}{\vec{a}_1 \cdot (\vec{a}_2 \times \vec{a}_3)}. \tag{3.27}$$

With the above construction one can simplify an impossible problem, that is to solve the Schrödinger equation in an infinite periodic lattice. In this way the problem can be solved in a section called the Brillouin zone. Unfortunately one can not assume translational symmetry for all systems, e.g. for surfaces and embedded impurities the translational symmetry is broken. In such cases the most common approach in the DFT community is to impose an artificial translational symmetry by creating a large unit cell an repeating it, which is called supercell approach. One must be careful because this artificial periodic boundary condition can introduce spurious interactions, and therefore the supercell must be large enough to minimize them. Another approach is to solve the DFT problem in real-space and this method will be introduced in the next chapter.

4. Green Functions

The Green function can be defined as

$$[z - \mathcal{L}(\mathbf{r})]G(\mathbf{r}, \mathbf{r}', z) = \delta(\mathbf{r} - \mathbf{r}') \tag{4.1}$$

where z is a complex variable, $\mathcal{L}(r)$ is a linear, time independent and hermitian operator. Assuming that has a complete set of solutions such as

$$\mathcal{L}(\mathbf{r})\psi_n(\mathbf{r}) = \lambda_n \psi_n(\mathbf{r}) \tag{4.2}$$

and

$$\sum_n \psi_n(\mathbf{r})\psi_n(\mathbf{r}') = \delta(\mathbf{r} - \mathbf{r}') \tag{4.3}$$

4.1 Green Functions in Real Space

4.1.1 The Chain Model

In this section we will introduce the Haydock recursion method, used in the RS-LMTO-ASA code [23]. The main idea of this method is to write a Hamiltonian ($\mathbf{H}$) in a given orthonormal basis $\{\mathbf{u}_i\}$, where in this new basis $\mathbf{H}$ has a tridiagonal form (Jacobi form). Initially we choose a given orbital $|\mathbf{u}_n\rangle$ that represents the atomic site we want to calculate the local density of states, and construct recursion relations as

$$\mathbf{H}|\mathbf{u}_n\rangle = a_n|\mathbf{u}_n\rangle - b_{n+1}|\mathbf{u}_{n+1}\rangle + b_{n-1}|\mathbf{u}_{n-1}\rangle \tag{4.4}$$

assuming the orthonormality of the basis $\langle \mathbf{u}_n|\mathbf{u}_m\rangle = \delta_{nm}$ and that $|\mathbf{u}_{-1}\rangle = 0$. Applying it recursively one can obtain $|\mathbf{u}_0\rangle, |\mathbf{u}_1\rangle, ..., |\mathbf{u}_n\rangle$. In this basis the Hamiltonian $\mathbf{H}$ becomes tridiagonal.

$$\mathbf{H} = \begin{bmatrix} a_0 & b_1 & 0 & 0 & \cdots \\ b_1 & a_1 & b_2 & 0 & \cdots \\ 0 & b_2 & a_2 & b_3 & \cdots \\ 0 & 0 & b_3 & a_3 & \cdots \\ \vdots & \vdots & \vdots & \vdots & \ddots \end{bmatrix} \tag{4.5}$$

The recursion parameters a_n and b_n can be interpreted as the on site energy and the hopping parameter respectively. One can interpret this model as the electron at a site $(n = 0)$ propagates throughout the system by hopping to it's nearest neighbors. So is expected that at one point the b_n parameters will become not so important. To calculate the recursion parameters one can take $n = 0$

$$\mathbf{H}|\mathbf{u}_0\rangle = a_0|\mathbf{u}_0\rangle - b_1|\mathbf{u}_1\rangle \tag{4.6}$$

and multiply the Eq.(4.4) from the left by $\langle \mathbf{u}_0|$

$$a_0 = \langle \mathbf{u}_0|\mathbf{H}|\mathbf{u}_0\rangle \tag{4.7}$$

and the b_1 is given by

$$b_1|\mathbf{u}_1\rangle = (\mathbf{H} - a_0)|\mathbf{u}_0\rangle \tag{4.8}$$

squaring Eq.(4.8) the b_1^2 is obtained

$$b_1^2 = \langle \mathbf{u}_0|(\mathbf{H} - a_0)^\dagger(\mathbf{H} - a_0)|\mathbf{u}_0\rangle. \tag{4.9}$$

With the a_0 and b_1 parameters the $|u_1\rangle$ can be calculated as

$$|\mathbf{u}_1\rangle = \frac{(\mathbf{H} - a_0)}{b_1}|\mathbf{u}_0\rangle \tag{4.10}$$

applying the above set procedure recursively the a_n, b_n and $|\mathbf{u}_n\rangle$ can be written as

$$a_n = \langle \mathbf{u}_n|\mathbf{H}|\mathbf{u}_n\rangle \tag{4.11}$$

$$b_{n+1}^2 = [\langle \mathbf{u}_n(\mathbf{H} - a_n)^\dagger - \langle \mathbf{u}_{n-1}|b_n^\dagger][(\mathbf{H} - a_n)|\mathbf{u}_n\rangle - b_n|\mathbf{u}_{n-1}\rangle] \tag{4.12}$$

$$|\mathbf{u}_{n+1}\rangle = \frac{(\mathbf{H} - a_n)|\mathbf{u}_n\rangle - b_n|\mathbf{u}_{n-1}\rangle}{b_{n+1}} \tag{4.13}$$

the above set of equations 4.11-4.13 one can construct the tridiagonal Hamiltonian. Using Hamiltonian one can construct the Green function of a differential linear operator, as the Kohn-Sham Hamiltonian (H) is defined as:

$$\mathbf{G} = [E + i\epsilon - \mathbf{H}]^{-1} \tag{4.14}$$

where E is the energy and $i\epsilon$ is a complex (ϵ is real and positive) energy used to avoid the singularities at the real axis. In principle one should diagonalize $[E + i\epsilon - \mathbf{H}]^{-1}$, to obtain the full Green function ($\mathbf{G}$). In

general such operation is very computational demanding due to the size of this matrix, containing several thousand of elements for a solid state system (bulk, surfaces, etc.). Fortunately one can relate the diagonal terms of $\mathbf{G}$ to local properties. An element of $\mathbf{G}$ is defined as

$$G_{\mathcal{U}\mathcal{V}} = \langle \mathcal{U}|[E - H]^{-1}|\mathcal{V}\rangle \tag{4.15}$$

which gives the propagator between sites $\mathcal{U}$ and $\mathcal{V}$. Particulary if $\mathcal{U}=\mathcal{V}=\mathcal{U}_0$ (represents the orbital of the chain's central atom). The term $G_{\mathcal{U}_0 \mathcal{U}_0}$ (G_{00}) is related to the local density of states as

$$\rho(E) = -\frac{1}{\pi} \lim_{\epsilon \to 0} \mathbf{Im}[G_{00}(E + i\epsilon)] \tag{4.16}$$

$$G(E) = \begin{bmatrix} E - a_0 & -b_1 & 0 & 0 & \dots \\ -b_1 & E - a_1 & -b_2 & 0 & \dots \\ 0 & -b_2 & E - a_2 & -b_3 & \dots \\ 0 & 0 & -b_3 & E - a_3 & \dots \\ \vdots & \vdots & \vdots & \vdots & \ddots \end{bmatrix}^{-1} \tag{4.17}$$

Defining $D_n(E)$ as the determinant of the matrix (E-$\mathbf{H}$) with the first n rows and columns deleted one can write G_{00} as

$$C_{00}(E) = \frac{D_1(E)}{D_0(E)} \tag{4.18}$$

using the cofactor expansion (Laplace expansion) $D_0(E)$ can be written as

$$D_0(E) = (E - a_0)D_1(E) - b_1^2 D_2(E) \tag{4.19}$$

as $\mathbf{H}$ is tridiagonal the only nonzero cofactors are the C_{00} and C_{01}, so G_{00} becomes

$$G_{00}(E) = \frac{1}{E - a_0 - b_1^2 \frac{D_2(E)}{D_1(E)}} \tag{4.20}$$

repeating this process a continued fraction is obtained

$$G_{00}(E) = \cfrac{1}{E - a_0 - \cfrac{b_1^2}{E - a_1 - \cfrac{b_2^2}{E - a_2 - \cfrac{b_3^2}{E - a_{3-\dots}}}}} \tag{4.21}$$

In principle the continued fraction is infinite, in practice it is limited by the finite cluster size. Each term included is a new hopping site and it is

expected that at some point sufficiently distant from the central site the coefficients a_i and b_i will converge. So one needs to truncate the infinite continuated fraction with a terminator $t(E)$.

$$G_{00}(E) = \cfrac{1}{E - a_0 - \cfrac{b_1^2}{E - a_1 - \cfrac{b_2^2}{E - a_{n-1} - \cfrac{b_n^2}{E - a_n + t(E).}}}} \qquad (4.22)$$

In this work the so called Beer-Pettifor terminator t(E) is used where

$$t(E) = \frac{b_N^2}{E - a_N - t(E)} \qquad (4.23)$$

Assuming that after N terms of the continued fraction the coefficients a_i and b_i are constants, for any $n > N$. After some algebraic manipulation

$$t(E) = \frac{1}{2}\left[(E - a_N) \pm \sqrt{(E - a_N - 2b_N)(E - a_N + 2b_N)}\right] \qquad (4.24)$$

this terminator will produce an continuous spectrum for the density of states, in the interval:

$$a_N - 2b_N \leq E \leq a_N + 2b_N \qquad (4.25)$$

This terminator is constructed for metallic systems, there are other terminator choice better suited to treat systems with gaps and highly localized systems.

t

5. Formation, interaction and ordering of local magnetic moments

In the itinerant picture one assumes that the electrons move nearly freely trough the crystal, one can wonder about the conditions to the formation of a ferromagnetic order in such system. As pointed out by Wigner [24], in a free electrons gas the formation of a ferromagnetic state is suppressed by the electron-electron correlation. This implies that, the formation of a ferromagnetic state must be related with the some degree of electronic localization around the atomic sites.

5.1 Stoner Criteria

The magnetic moment of free atoms can be obtained from the Hund's rule, and is given by the sum of the spin (S) and angular (L) momenta. In general for transition metals solids, the orbital moment is almost completely suppressed and L is not a good quantum number. Extrapolating the spin moment given by the Hund's rule to a solid, would lead to a completely failure. A value of 4 μ_b is predicted from the Hund's rule for the Fe ion spin moment. The Fe bcc magnetic moment is experimentally determined as 2.2 μ_b per Fe atom. In 1939 Stoner proposed a model to explain, and predict, the formation of a ferromagnetic state, e.g. local magnetic moments in solids, in the same spirit of the Weiss model Stoner introduced a molecular field,

$$\mathcal{H}_{stoner} = \mathcal{I}M \tag{5.1}$$

where $\mathcal{I}$ is the so called Stoner parameter and M is the magnetization (which is computed as the difference between the spin up and down occupation), the Stoner molecular field breaks the symmetry of the spin up and down bands, and takes into account the electronic interaction. A model of a non-magnetic density of states (DOS) is showed at Fig 5.1 a). Applying an external magnetic field (H), electrons from the spin down band are promoted to the spin up bands as showed in Fig 5.1 b). The total energy in the presence of an external magnetic field (H) can be written as:
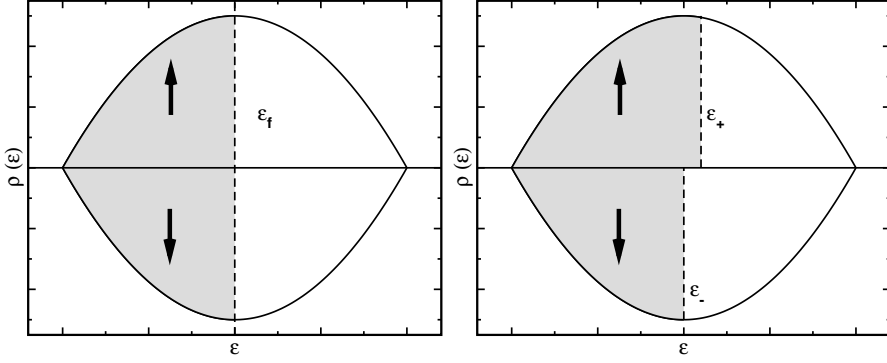
Figure 5.1. Splitting of the spin up and down bands due to an external field H.

$$E = \int_0^{\epsilon_f} \epsilon \rho(\epsilon) d\epsilon + \int_{\epsilon_f}^{\epsilon_+} \epsilon \rho(\epsilon) d\epsilon + \int_0^{\epsilon_f} \epsilon \rho(\epsilon) d\epsilon - \int_{\epsilon_-}^{\epsilon_f} \epsilon \rho(\epsilon) d\epsilon - \frac{1}{2} \mathcal{I} M^2$$
(5.2)

Where $\rho(\epsilon)$ is the density of sates, ϵ_f is the non magnetic Fermi energy and ϵ_+ (ϵ_-) is the Fermi energy for the spin up (down) bands, these are proportional to the H as $\epsilon_\pm = (\epsilon_f \pm \mu_\beta H)$. The second (last) term of Eq. 5.2 are the energy gain (lost) by the spin up (down) bands. Considering a rectangular DOS and integrating Eq. 5.2 one obtains:

$$E(H, M) = E_P + \mu_b^2 \rho(\epsilon_F) H^2 - \frac{1}{2} \mathcal{I} M^2$$
(5.3)

where E_P is the paramagnetic contribution to the total energy. From Eq. 5.3 in the absence of interactions, i.e. no molecular field, the Pauli paramagnetic susceptibility ($\chi^{-1} = \partial^2 E / \partial H^2$) is obtained : $\chi_P = 2\mu_b^2 \rho(\epsilon_F)$. Using this to write H in terms of the magnetization one obtain

$$E(M) = E_P + \frac{M^2}{2\chi_P} - \frac{1}{2} \mathcal{I} M^2,$$
(5.4)

since $M = \chi_P H$. Computing the new susceptibility, in the presence of the a molecular field.

$$\chi = \frac{\chi_P}{1 - \chi_P \mathcal{I}}$$
(5.5)

For the nonmagnetic state to be unstable is necessary that $\chi < 0$. From Eq.(5.5) is clear that the instability condition is given by

$$2\mu_b^2 \rho(\epsilon_F) \mathcal{I} > 1$$
(5.6)

this is the Stoner criteria. Where $\mathcal{I}$ is the Stoner parameter and it is nearly an atomic property. Although the Stoner criteria works quite well in predicting the formation of local moments at 0 K, it does not work for finite temperatures given T_C values order of magnitudes higher than the experimental values. Is important to stress that this criteria is obtained in the itinerant electron picture. As will be shown in the chapter 9 this criteria does not work in strongly localized systems.

5.2 Exchange Interactions

To calculate the exchange parameter one needs to determine the energy variation due to a small rotation of the magnetic moments, for the Heisenberg model and in the LDA. Later one can compare these two equations in order to obtain a expression to the J_{ij}. Consider two local spins at sites i and j. In the Heisenberg model

$$H = -\sum_{ij} J_{ij}\vec{e}_i \cdot \vec{e}_j \tag{5.7}$$

the energy variation due to a rotation, on opposite angles $\pm\theta/2$ is given by

$$\delta E_{ij} = J_{ij}(1 - cos(\theta)) \approx \frac{1}{4}J_{ij}\theta^2. \tag{5.8}$$

Now one need to compute the energy variation in the LSDA approach, which is rather complicated. As we are interested only in small deviations from the ground state the "local force theorem" can be used. This was proposed by Liechtenstein *et. al.* [25]. This calculation is better evaluated in the multiple scattering framework, for a review on this subject see [26]. One can relate the multiple scattering parameters to the orthogonal LMTO basis used in the RS-LMTO-ASA code [27]. So the energy variation is written as

$$\delta E_{ij} \simeq \frac{1}{\pi} \int_{-\infty}^{\epsilon_F} d\epsilon \mathbf{Im} Tr_l[\delta_i(\epsilon)G_{ij}^{\uparrow\uparrow}\delta_j(\epsilon)G_{ij}^{\downarrow\downarrow}]\frac{\theta^2}{4} \tag{5.9}$$

where l is the orbital index, $G_{ij}^{\sigma\sigma}$ is the propagator for the electron with spin σ between the sites i and j and δ_i is given by

$$\delta_{li}(\epsilon) = \frac{C_{li}^{\downarrow}\Delta_{li}^{\uparrow} - C_{li}^{\uparrow}\Delta_{li}^{\downarrow} + (\Delta_{li}^{\downarrow} - \Delta_{li}^{\uparrow})\epsilon}{(\Delta_{li}^{\downarrow}\Delta_{li}^{\uparrow})^{\frac{1}{2}}} \tag{5.10}$$

and C_{li}^{σ}, Δ_{li}^{σ} are the potential parameters in the orthogonal LMTO basis. Comparing equations 5.8 and 5.9 one obtains

$$J_{ij} = -\frac{1}{4\pi}\mathbf{Im}Tr_l \int_{-\infty}^{\epsilon_F} d\epsilon \delta_i(\epsilon)G_{ij}^{\uparrow\uparrow}\delta_j(\epsilon)G_{ij}^{\downarrow\downarrow}. \qquad (5.11)$$

One should always calculate the J_{ij} from a ferromagnetic state, as the above expression is only valid for small deviations from the ferromagnetic ground state. A negative J_{ij} value indicates an instability of this state, e.g. and anti-ferromagnetic configuration is favored.

5.3 Noncollinear Ordering

When we introduced the Kohn-Sham equations in chapter 2, for simplicity, it was done using the charge density $n(\vec{r})$, one can generalize the charge density to treat magnetic systems as

$$\rho(\vec{r}) = \sum_{i=1}^{N} \begin{pmatrix} \rho_{\phi\phi} & \rho_{\phi\chi} \\ \rho_{\chi\phi} & \rho_{\chi\chi} \end{pmatrix}. \qquad (5.12)$$

Using the spinor structure of Eq.(2.4) and the Eq.(2.50) one can rewrite $\rho(\vec{r})$ as

$$\rho(\vec{r}) = \sum_{i=1}^{N} \begin{pmatrix} |\phi_i(\vec{r})|^2 & \langle\phi_i(\vec{r})|\chi_i(\vec{r})\rangle \\ \langle\chi_i(\vec{r})|\phi_i(\vec{r})\rangle & |\chi_i(\vec{r})|^2 \end{pmatrix}. \qquad (5.13)$$

one can recast the charge density $n(\vec{r})$ and write the generalized charge density as

$$\rho(\vec{r}) = \frac{1}{2}[n(\vec{r}) + \vec{m}(\vec{r}) \cdot \vec{\sigma}] \qquad (5.14)$$

Using Eq.(4.16) one can write the magnetization in terms of the local Green's function (G) and the Pauli matrices (σ)

$$\vec{m}(\epsilon) = -\frac{1}{\pi}\mathbf{Im}Tr[\sigma G(\epsilon)]. \qquad (5.15)$$

For a collinear magnetic state only one spin quantization axis is allowed and the Eq.(5.15) is reduced to

$$m(\epsilon) = -\frac{1}{\pi}\mathbf{Im}Tr[\sigma_z G(\epsilon)]. \qquad (5.16)$$

the choice of σ_z is arbitrary, could have used any of the other two Pauli matrices. For the noncollinear case in principle one should compute the full Green's function with all the off diagonal terms. This can be done but is more computationally costly. The approach used here is to rotate the spin density matrix so that the local and global spin axis coincides.

With such a rotated spin matrix the recursion scheme can be applied and one would obtain a magnetization density $m_x(\epsilon)$, $m_y(\epsilon)$ and $m_z(\epsilon)$. This approach is necessary only due to the recursion method. For most other methods it is usually mostly about doubling the dimensions of the Hamiltonian when you go to a spinor formalism. For certain systems the noncollinear arrangement is the ground state, due to band effects, frustration and competition interactions. In chapter 10, this effects will be explored.

6. Dynamical Mean Field Theory

The DFT approach is a mean field like theory that incorporates part of the many-body effects through the potential V^{LDA} (or GGA). Despite its success LDA can not describe all the different energy scales of the solid state, and this leads to failure for many physical systems. For example the insulating behavior of some transition metal oxides (Mott insulators), rare-earth compounds, high-T_c superconductors and systems with localized impurities in general are poorly described in the LDA approach. The inability of the LDA to describe these systems is related to the localized character of d and f electrons, which enhances correlations between them. It should be noted that it is not only the mean field nature to be responsible for the failure in describing strongly correlated systems, since mean field solutions to model Hamiltonians usually give a much better description of their physics. Moreover it is intriguing that some of these models are constructed using DFT parameters. It was pointed out by Lopez-Aguilar *et al.* [28] that the lack of a Hubbard type term in the DFT Hamiltonian is the cause of the failure in describing strongly correlated systems. A different view on the problem is related to the self-interaction. When the Hartree energy is calculated, the electrostatic interaction of a given electron with itself is included. In principle this should be canceled out by the exchange potential, as it occurs for the Hartree-Fock method. In the HF equations the entire spurious self-interaction energy is compensated by the exchange interaction, but unfortunately this compensation is only partial in the basic LDA potential. For localized systems the contribution of this self interaction can become very large. Some approaches were proposed to correct this deficiency, one of the most successful one being the Self Interaction Correction (SIC) method [29]. However, as we will see in the next section this problem is automatically solved by introducing a Hubbard type term in the DFT Hamiltonian, and that is why we are going to focus on this kind of approach.

6.1 LDA + U

Despite the fact that we do not use the LDA + U approach in this work it is worth to spend a few words on one of the first successful methods to incorporate the Hubbard physics into the DFT framework.

Anisimov and coworkers [30] corrected the LDA Hamiltonian ($\hat{H}_{LDA}$), with an explicitly term for the Coulomb repulsion between the localized electrons. The obtained equations can be easily extended to LSDA and GGA functionals. The general strategy is to choose the set of orbitals which the Hubbard term will act on, i.e. the so called correlated orbitals ($|\mathbf{R}, \xi_i\rangle$). In general these are atomic-like d or f but other choices are possible on the basis of physical guidelines. The LDA + U Hamiltonian can be written as

$$\hat{H}^{LDA+U} = \hat{H}_{LDA} + \frac{1}{2} \sum_{\mathbf{R}} \sum_{\xi_1 \xi_2 \xi_3 \xi_4} U_{\xi_1 \xi_2 \xi_4 \xi_3} c^\dagger_{R,\xi_1} c^\dagger_{R,\xi_2} c_{R,\xi_4} c_{R,\xi_3} \quad (6.1)$$

where H_{LDA} is given by Eq.(2.49), ξ_i denotes the orbital and spin index and the U-matrix is defined in similar way as the Hartree energy in the HF equations Eq.(2.23), but instead of the full Coulomb interaction one should use a screened Coulomb interaction $U_S(\mathbf{r} - \mathbf{r}')$:

$$U_{\xi_1 \xi_2 \xi_3 \xi_4} = \delta_{\sigma_1 \sigma_3} \delta_{\sigma_2 \sigma_4} \int d\mathbf{r} d\mathbf{r}' \chi^*_{L_1}(\mathbf{r}) \chi^*_{L_2}(\mathbf{r}') U_S(\mathbf{r} - \mathbf{r}') \chi_{L_3}(\mathbf{r}) \chi_{L_4}(\mathbf{r}')$$
$$(6.2)$$

This choice is due to the fact that only the Coulomb interaction on the subspace of the correlated orbitals is considered explicitly, and therefore all other electrons, e.g. s and p, should be integrated out. In principle one can be as *Ab Initio* as possible by calculating the U-matrix through the constrained LDA or RPA [31; 32; 33] schemes, although it is more usual to use U as a free parameter. Needless to say that the U value must be chosen wisely otherwise one can end up with meaningless results. Another drawback of the method is the so called double-counting (DC) problem. The V^{XC} potential calculated within the LDA takes wrongly into account the Coulomb interaction for the correlated orbitals, and therefore this wrong contribution must be subtracted in the LDA+U scheme. This results into a major difficulty, since LDA gives a spherical V^{XC} and thus it is not possible to track the orbital resolved contributions from the Coulomb interaction. There are several schemes to deal with such a problem and they will be discussed later.

6.2 Hubbard Model and The Self-energy

This section will introduce the concept of self-energy, deriving the equations from the famous Hubbard model. This model was proposed by Hubbard in 1963 [34; 35; 36] and, even being one of the most studied models, no analytical solution can in general be found for dimensions higher than one. The Hubbard model in real space can be written as:

$$\mathcal{H} = \sum_{ij\sigma} t_{ij} c_{i\sigma}^{\dagger} c_{j\sigma} + \frac{1}{2} U \sum_{i\sigma} n_{i\sigma} n_{i\bar{\sigma}} - \mu \sum_{i\sigma} c_{i\sigma}^{\dagger} c_{i\sigma} \qquad (6.3)$$

where i and j label the lattice sites, σ ($\bar{\sigma} = -\sigma$) the spin degrees of freedom, the kinetic energy term (hopping term) is described by t_{ij} and $c_{i\sigma}^{\dagger}$ ($c_{i\sigma}$) is the creation (annihilation) operator. Given that we assume a single orbital in this model, the Hubbard parameter U is approximated as a single number instead of the matrix Eq.(6.2). The particle number operator and the chemical potential are labeled by n and μ respectively. The last one is introduced to fix the number of particles. All the operators are written in the Heisenberg picture. So far we have defined the strong correlation in a handwaving way; with the Hubbard model one can give a better definition of what is meant by strongly or weakly correlated system. The hopping (t_{ij}) can be defined as

$$t_{ij} = -\int d\mathbf{r} \chi_L^*(\mathbf{r} - \mathbf{r}_i) \left(\frac{\hbar^2 \nabla^2}{2m} \right) \chi_{L'}(\mathbf{r} - \mathbf{r}_j) \qquad (6.4)$$

where $\chi_L(\mathbf{r} - \mathbf{r}_i)$ is a MTO (or Wannier-like orbital) centered at $\mathbf{r}_i$ and L denotes the l,m quantum numbers. So the hopping integral is proportional to the overlap. The regimes of strong and weak correlations are defined by the relation between t and the U. The strong and weak correlation regimes are characterized by $t << U$ and $t >> U$, respectively. Despite the aim of this work is not the Hubbard model itself, it is very instructive, and simpler, to work with this system, as the conclusions can be extrapolated to other systems as well. The Green's function can be written as

$$G_{ij}^{\sigma}(t - t') = \langle\langle c_{i\sigma}(t); c_{j\sigma}^{\dagger}(t') \rangle\rangle = -i\langle T\{c_{i\sigma}(t); c_{j\sigma}^{\dagger}(t')\}\rangle. \qquad (6.5)$$

Here $\{\hat{A}, \hat{B}\}$ is the anti-commutator, and T can be the normal, advanced or retarded ordering operator. Instead of computing directly the Green's function, let us focus on its time evolution. We can take the time derivative of Eq.(6.5)

$$i\frac{d}{dt} G_{ij}^{\sigma}(t, t') = \delta(t - t')\langle\{c_{i\sigma}(t); c_{j\sigma}^{\dagger}(t')\}\rangle + \left\langle\left\langle \frac{d}{dt} c_{i\sigma}(t); c_{j\sigma}^{\dagger}(t') \right\rangle\right\rangle. \quad (6.6)$$

The time evolution of a Heisenberg operator is given by,

$$i\frac{d}{dt} \hat{A}(t) = [\hat{A}(t), \hat{H}]. \qquad (6.7)$$

If $\hat{H}$ does not explicitly depend on time, one can write $[\hat{A}(t), \hat{H}] = [\hat{A}, \hat{H}](t)$, so Eq. (6.6) is rewritten as

$$i\frac{d}{dt}G_{ij}^{\sigma}(t,t') = \delta(t-t')\langle\{c_{i\sigma}(t);c_{j\sigma}^{\dagger}(t')\}\rangle + \left\langle\left\langle[c_{i\sigma},\mathcal{H}](t);c_{j\sigma}^{\dagger}(t')\right\rangle\right\rangle \quad (6.8)$$

To solve the above equation of motion one needs to calculate the commutator:

$$[c_{i\sigma},\mathcal{H}] = [c_{i\sigma},\sum_{lm\sigma'}t_{lm}c_{l\sigma'}^{\dagger}c_{m\sigma'}] + [c_{i\sigma},U/2\sum_{l\sigma'}n_{l\sigma'}n_{l\bar{\sigma}'}] - \mu[c_{i\sigma},\sum_{l\sigma'}c_{l\sigma'}^{\dagger}c_{l\sigma'}]$$

$$= \sum_{lm\sigma'}t_{lm}\delta_{il}\delta_{\sigma\sigma'}c_{m\sigma'} + U\sum_{l\sigma'}n_{l\bar{\sigma}}\delta_{il}\delta_{\sigma\sigma'}c_{l\sigma} - \mu\sum_{l\sigma'}\delta_{il}\delta_{\sigma\sigma'}c_{l\sigma}$$

$$(6.9)$$

substituting Eq. (6.9) back in Eq. (6.8),

$$i\frac{d}{dt}G_{ij}^{\sigma}(t,t') = \delta(t-t')\langle\{c_{i\sigma}(t);c_{j\sigma}^{\dagger}(t')\}\rangle + \sum_{m}t_{im}\left\langle\left\langle c_{m\sigma}(t);c_{j\sigma}^{\dagger}(t')\right\rangle\right\rangle +$$

$$+ U\left\langle\left\langle n_{i\bar{\sigma}}c_{i\sigma}(t);c_{j\sigma}^{\dagger}(t')\right\rangle\right\rangle - \mu\left\langle\left\langle c_{i\sigma}(t);c_{j\sigma}^{\dagger}(t')\right\rangle\right\rangle.$$

$$(6.10)$$

Rearranging the above equation and defining the two particle Green's function as

$$G_{ij}^{\bar{\sigma}\sigma}(t,t') = \left\langle\left\langle n_{i\bar{\sigma}}c_{i\sigma}(t);c_{j\sigma}^{\dagger}(t')\right\rangle\right\rangle \quad (6.11)$$

one obtains,

$$i\frac{d}{dt}G_{ij}^{\sigma}(t,t') = \delta(t-t')\delta_{ij} + \sum_{m}t_{im}G_{mj}^{\sigma}(t,t') - \mu G_{ij}^{\sigma}(t,t') + U G_{ij}^{\bar{\sigma}\sigma}(t,t').$$

$$(6.12)$$

Eq. (6.12) involves a higher order (two particle) Green's function $G_{ij}^{\bar{\sigma}\sigma}(t,t')$. Calculating the time evolution of $G_{ij}^{\bar{\sigma}\sigma}(t,t')$ would produce a even higher order Green's function, leading an infinite set of coupled equations. Obviously infinite terms can not be computed. Before introducing a new approach to this problem let us take the Fourier transformation of Eq. (6.12) with respect to the time and lattice variables.

$$\omega G_{\sigma}(\omega,k) = \mathbb{1} + \epsilon(k)G_{\sigma}(\omega,k) - \mu G_{\sigma}(\omega,k) + U G_{\bar{\sigma}\sigma}(\omega,k) \quad (6.13)$$

rearranging Eq. (6.13),

$$G_\sigma(\omega, k) = \frac{\mathbb{1} + UG_{\bar\sigma\sigma}(\omega, k)}{\omega - \epsilon(k) + \mu}. \tag{6.14}$$

Here and in the following we did not add the limit to avoid the discontinuity on the real energy axis [37]. This hierarchy of equations, e.g. the explicit dependence of the one particle GF on the two particle GF and so on, is due to the interaction term $n_{i\sigma}n_{i\bar\sigma}$. In principle all n particle processes should contribute to the GF, but in practice this series must be truncated. One can identify the non-interacting Green's function by setting U=0 in Eq. (6.14):

$$g_\sigma(\omega, k) = [\omega - \epsilon(k) + \mu]^{-1}. \tag{6.15}$$

Our approach is then constructed on the validity of the following decomposition:

$$UG_{\bar\sigma\sigma}(\omega, k) = \Sigma_\sigma(\omega, k)G_\sigma(\omega, k) \tag{6.16}$$

where all processes involving more than one particle are contained in $\Sigma_\sigma(\omega, k)$. This quantity is called self-energy. Using Eq.(6.15) and Eq.(6.16) into Eq.(6.14), and after some algebraic manipulation, the so called Dyson equation is obtained;

$$G^{-1}(\omega, k) = g^{-1}(\omega, k) - \Sigma(\omega, k), \tag{6.17}$$

where from now on the spin index will be suppressed. The self-energy corrects the non-interacting GF to obtain the one particle GF. The self-energy obtained here is a non-local ($\mathbf{k}$ dependent) and energy dependent operator. If one knew the exact form of the self-energy operator the theory would be exact, in the same spirit of the exchange-correlation potential in the Kohn-Sham equations. Unfortunately the full knowledge of $\Sigma(\omega, k)$ for lattice models is not possible and approximations are unavoidable.

6.2.1 Local Limit of The Self-energy

Calculating the full non-local self-energy of a system of interacting electrons is a daunting task. The most used method to calculate $\Sigma(\omega, k)$ in materials is the GW approximation [38; 39]. It is based on a generalized Hartree-Fock method. The electrons effectively interact through the screened Coulomb interaction, where the screening is calculated from the inverse dielectric function $\epsilon(\mathbf{r}, \mathbf{r}'; \omega)$, obtained with the random phase approximation. Some comments on the GW method are important here. The frequency dependence of the dielectric function will impose a frequency dependence on the screened Coulomb potential as well. This is natural since the response of the system to a charge excitation is

expected to be energy (frequency) dependent. This implies that any modeling of the relevant processes should be based on a U-matrix, see Eq.(6.2), which is frequency dependent as well. In spite of that, most applications of DMFT treat U as frequency independent. Recently the first treatment of the frequency dependency of U was reported [40]. The GW approach is a very computationally demanding method and is in general used for small systems. Moreover the GW approximation breaks down for strongly correlated systems, as in the case of NiO. While the GW equations make the method fully self-consistent, most of the GW calculations are performed in a perturbative fashion on top of DFT. If DFT gives unphysical results GW will not show much improvement. An alternative solution to the problem was presented by Metzner and Vollhardt [41] in what is considered as the "kick off" of the DMFT formulation. They showed that in the limit of infinite dimension ($d \to \infty$) the Hubbard Model off-site self-energy (Σ_{ij}) with $i \neq j$ is much smaller then the on-site ($\delta_{ij}\Sigma_{ij}$)

$$\Sigma_{ij}(\omega) \to \delta_{ij}\Sigma(\omega), \tag{6.18}$$

i.e. the self energy is purely local. As a result the Fourier transform in Eq.(6.18) becomes momentum-independent. This is similar to the infinite dimension limit of the Heisenberg model on a lattice.

6.3 DMFT Equations

The DMFT [42; 43; 44] approach maps the electronic problem in a lattice to the problem of a single impurity coupled to an effective bath. The focus is on the on site (local) Green's function, which is the conserved observable. The G_{ii} plays the role of the electron density ($\rho(\mathbf{r})$) in the DFT where the system is mapped into a effective potential (v_{xc}). The local Green's function is given by

$$G_{ii}^{\sigma}(\tau - \tau') \equiv \langle TC_{i\sigma}(\tau)C_{i\sigma}^{\dagger}(\tau') \rangle, \tag{6.19}$$

where τ and τ' are imaginary time in the Matsubara's formalism for finite temperature. The problem of a single impurity in an effective bath, is know as the Anderson impurity model [45] and can be described through the following Hamiltonian

$$H_{AIM} = Uc_{\uparrow}^{\dagger}c_{\uparrow}c_{\downarrow}^{\dagger}c_{\downarrow} + \sum_{\mathbf{k}\sigma} \epsilon_{\mathbf{k}} c_{\mathbf{k}\sigma}^{\dagger}c_{\mathbf{k}\sigma} + \sum_{\mathbf{k}\sigma} V_{\mathbf{k}\sigma}(a_{\mathbf{k}\sigma}^{\dagger}c_{\mathbf{k}\sigma} + c_{\mathbf{k}\sigma}^{\dagger}a_{\mathbf{k}\sigma}). \tag{6.20}$$

The first term is the onsite Coulomb interaction, the second term describes the bath degrees of freedom and the last term is the coupling

between the impurity and the bath. In the effective action formalism one can integrate out the the bath degrees of freedom:

$$S_{eff} = -\int_0^\beta d\tau \int_0^\beta d\tau' \sum_\sigma c_\sigma^\dagger(\tau)\mathcal{G}_0^{-1}(\tau-\tau')c_\sigma(\tau') + U\int_0^\beta d\tau n_\uparrow(\tau)n_\downarrow(\tau')$$

(6.21)

where the bares Green's function $\mathcal{G}_0^{-1}$ is given by

$$\mathcal{G}_0^{-1}(i\omega_n) = i\omega_n + \mu - \Delta(i\omega_n)$$

(6.22)

and $\Delta(i\omega_n)$ is called hybridization function and μ is the chemical potential and $i\omega_n$ are imaginary Matsubara frequencies [37]. The hybridization function connects the impurity to the bath and is defined as

$$\Delta(i\omega_n) = \sum_{\mathbf{k}} \frac{|V_{\mathbf{k}}|^2}{i\omega_n - \epsilon_{\mathbf{k}}}.$$

(6.23)

One can write a Dyson equation for the single impurity problem, similarly to what was done for the Hubbard Model on a lattice. However in this case a purely local impurity self energy $\Sigma_{imp}(i\omega_n)$ is obtained, giving:

$$G_{imp}^\sigma(i\omega_n)^{-1} = \mathcal{G}_0^\sigma(i\omega_n)^{-1} - \Sigma_{imp}^\sigma(i\omega_n).$$

(6.24)

All these equations are subjected to conservation of the local Green's function imposed in the DMFT:

$$G_{ii}^\sigma(i\omega_n) = G_{imp}^\sigma(i\omega_n).$$

(6.25)

In principle the self energy from the original lattice problem is $\mathbf{k}$-dependent, but we approximate it by a local, $\mathbf{k}$-independent self energy Σ_{ii}. As previously showed in the limit of infinite coordination number this approximation is exact.

Summarizing the procedure we have:

1. guess the initial self energy $\Sigma_{ii}(i\omega_n)$, in general zero;
2. project the global Green's function into the correlated orbitals of the impurity site to get $G_{ii}(i\omega_n)$ and adjust the chemical potential μ to get the corrected number of electrons;
3. compute the bath Green's function ($\mathcal{G}_0$) from the inverse Dyson equation

$$G_{ii}(i\omega_n)^{-1} = \mathcal{G}_0(i\omega_n)^{-1} - \Sigma(i\omega_n);$$

(6.26)

4. calculate $G_{imp}(i\omega_n)$ using an impurity solver to solve the Anderson impurity model.
5. compute the new self energy from the Dyson equation (6.17);
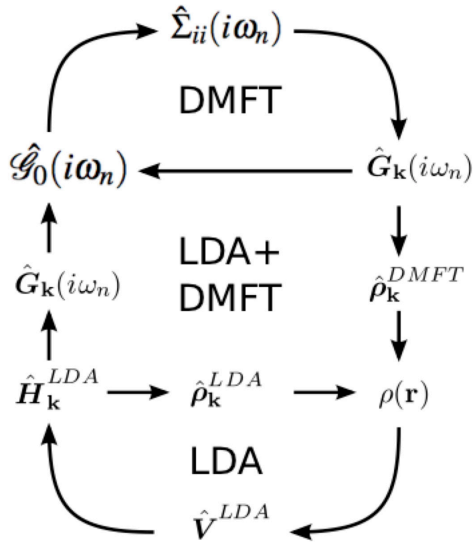6. run the cycle until the self-energy is converged.

$$\hat{\Sigma}_{ii}(i\omega_n)$$

DMFT

$$\mathcal{\hat{G}}_0(i\omega_n) \longleftarrow \hat{G}_{\mathbf{k}}(i\omega_n)$$

$$\hat{G}_{\mathbf{k}}(i\omega_n) \qquad \text{LDA+} \qquad \hat{\rho}_{\mathbf{k}}^{DMFT}$$

DMFT

$$\hat{H}_{\mathbf{k}}^{LDA} \longrightarrow \hat{\rho}_{\mathbf{k}}^{LDA} \longrightarrow \rho(\mathbf{r})$$

LDA

$$\hat{V}^{LDA}$$

Figure 6.1. LDA+DMFT schematic representation. Adapted from [46]

The Fig.6.1 shows the schematic merger between DMFT and LDA.

The Anderson impurity model has been studied extensively. Nevertheless still is a very complicated problem and several impurity solvers have been proposed. The choice of the impurity solver is related to the problem to be studied and will be discussed appropriety for each system.

7. Permanet Magnetic Materials

The present chapter is based on the following publication:

1. M. Costa, O. Grånäs, A. Bergman, P. Venezuela, P. Nordblad, M. Klintenberg and O. Eriksson. "On the large magnetocrystalline anisotropy of Fe_2P". Phys. Rev. B **86**, 085125 (2012).

Magnetic materials with large magnetic anisotropy (MAE) have been used in many applications. Until recently the dominating class of materials used for such applications, apart from hard ferrites, were rare-earth based magnets, e.g. $Nd_2Fe_{14}B$ [47], in which the large magnetic anisotropy energy is provided by the rare-earth atoms, and the large saturation moment (M_s) at finite temperature is due to the Fe atoms. It has however been pointed out that other permanent magnets should be investigated, from an application point of view, since a general access to rare-earth elements is far from guaranteed [48]. Among such materials the iron-phosphide Fe_2P stands out as a particularly interesting material, due to its known large MAE and sufficient large value of saturation moment. In addition Fe_2P is composed by cheap and widely available elements.

Transition metal pnictides and chalcogenides are not the only large MAE materials that have been investigated so far. For instance, a large saturation moment was suggested in a nano-laminate of a 3d metal (Fe) and a rare earth metal (Gd) in Ref.[49]. Also, a large magnetic anisotropy in FePt was verified experimentally as well as from first principles theory [50; 51; 52; 53; 54]. Furthermore, the predicted large MAE of a tetragonally strained FeCo-alloy [55] was verified experimentally [56]. The focus on Fe_2P, is due to it's unexpected large MAE and hitherto unexplained. And the aim of this study is to find a microscopic description for it's MAE.

7.1 Magnetic Anisotropy

In an ideal isotropic single domain ferromagnetic material the spontaneous magnetization (M_s) can be reoriented, by an external field, at no energy cost. The magnetic anisotropy implies an energy penalty to the reorientations of M_s. The magnetic anisotropy energy (MAE) is defined as the internal energy variation, of a ferromagnetic material, with respect
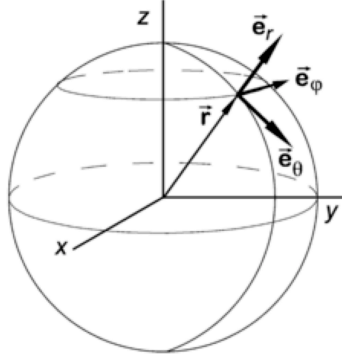
Figure 7.1. Magnetization in spherical coordinates.

to the spontaneous magnetization direction [57]. The magnetization ($\vec{M}$) of a given material can be written in spherical coordinates as,

$$\vec{M} = M_s[sin(\theta)\ sin(\phi)\ \hat{e}_x + sin(\theta)\ cos(\phi)\ \hat{e}_y + cos(\theta)\ \hat{e}_z] \qquad (7.1)$$

where θ and ϕ are the polar and azimuthal spherical coordinates respectively and $\hat{e}_i$ is the unitary vector in cartesian coordinates, i=x,y,z. Before investigating the origin of such anisotropy, one can parametrize the relation of the magnetization direction with the energy. Historically the parametrization was done as a power series of the cosine directions (α) of the magnetization. Consider a single magnetic domain, where all the spins are aligned, with a volume V. The energy density can be written as,

$$\frac{E}{V} = E_0 + \sum_{ij} b_{ij}\alpha_i\alpha_j + \sum_{ijkl} b_{ijkl}\alpha_i\alpha_j\alpha_k\alpha_l. \qquad (7.2)$$

Considering (some) symmetry properties only few terms need to be considered. Due to time-reversal symmetry any odd power of α must be zero, i.e. E($\vec{M}$) = E(-$\vec{M}$). If we consider an *uniaxial anisotropy* where the in-plane anisotropy can be neglected, this is the case for hcp Co. The anisotropy energy becomes

$$\frac{E}{V} = K_0 + K_1\ sin^2(\theta) + K_2\ sin^4(\theta) + K_3\ sin^6(\theta) \qquad (7.3)$$

where K_m are called anisotropy constants. In general only a few terms of equation (7.3) need to be considered. One can also formulate the expansion in Eq.(7.2) in terms of spherical harmonics, which posses the advantage of forming a complete set of orthonormal functions [58].

50

7.2 Physical Origin

There are several processes contributing to the magnetic anisotropy. One of them is magnetic dipole-dipole interactions. Assuming the existence of local magnetic moments (m_i) in a lattice, representing the integrated magnetization density within each atomic cell, around the lattice ions. The energy interaction of localized magnetic dipoles is given by,

$$E_{dipole} = \frac{\mu_\beta^2}{2} \sum_{ij} \frac{m_i m_j}{r_{ij}^3} (1 - cos^2\theta_{ij}) \qquad (7.4)$$

where r_{ij} is the distance between the dipoles and θ_{ij} is the angle between the line connecting the spins i and j and the magnetization direction $(\hat{e}_M)$. This clearly gives rise to a structure dependent energy term, however in general it contributes with a very small value [59]. In order to be the only responsible mechanism. When dealing with small particles, where the surface is large relatively to the volume, the so called *shape anisotropy* plays a role. The mechanism for the *shape anisotropy* is the dipole-dipole interactions. In a cubic symmetry only second order terms of Eq.(7.4) contributes, but that is not the case for small particles with spherical shapes. It was first suggested by Van Vleck *et. al.* that spin-orbit interactions was the responsible for the MAE, latter Van Vleck showed that indeed this was the case, this interaction is called *magnetocrystalline anisotropy.*

7.2.1 Magnetocrystalline Anisotropy

The magnetocrystalline anisotropy arises from the interaction of the electronic spin with the magnetic orbital moment, as the latter is localized at the lattice ions this interaction couples the electronic spin degrees of freedom to the lattice. The orbital moment arises from unfilled d and f shells, and due to the crystal field effect the orbital moment is suppressed. This is called quenching of the orbital moment. The Fig. 7.2.1 a) shows the spherical charge distribution of a free atom. As ions move towards the atom, forming an octahedral environment, the charge will be redistributed to avoid the ions, as in Fig. 7.2.1. As a consequence the atomic energy levels will change. For *d-states* the octahedral crystal field will raise the free atom ten-fold degenerated levels to a six and four-fold degenerated levels, moreover the spin-orbit coupling will split these states even further.

In a free atom the orbital moment is given by the Hund's rule. The Fe free atom in a d^6 configuration has a orbital moment of 2.0 μ_b and full rotational symmetry, e.g. MAE is zero. The bcc Fe has a orbital moment of 0.085 μ_b [60] and a MAE of 2.4 μeV/atom. The new generation of permanent magnets, rare-earth based materials, posses a large
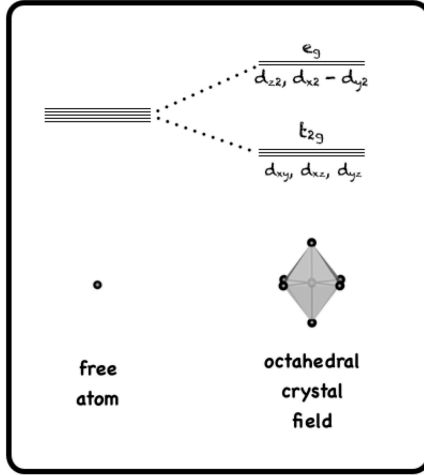
Figure 7.2. Crystal field spliting of the atomic energy levels of a d-shell.

orbital moment as the *f-states* are very localized and less sensitive to the crystal field splitting. As showed in chapter 2 the spin-orbit coupling Hamiltonian is given by $H_{SOC} = \xi \vec{L} \cdot \vec{S}$ and can be introduced as a perturbation.

$$H_{SOC} = \xi \vec{L} \cdot \vec{S} = \xi(L_x S_x + L_y S_y + L_z S_z). \tag{7.5}$$

In second order perturbation theory the energy correction due to the spin-orbit is,

$$\Delta E = -\xi^2 \sum_{u,o} \frac{|\langle o|H_{SOC}|u\rangle|^2}{\delta\epsilon_{uo}} \tag{7.6}$$

where u and o label the unoccupied and occupied states respectively and $\delta\epsilon_{uo}$ is the energy difference between the occupied and unoccupied eigenvalues. To better understand the theory one can define the so called ladder operators: $L_\pm$ and $S_\pm$.

$$L_\pm = L_x \pm iL_y \tag{7.7}$$
$$S_\pm = S_x \pm iS_y \tag{7.8}$$

the action of the ladder operators is given by,

$$L_\pm|lms\rangle = \hbar\sqrt{l(l+1) - m_l(m_l \pm 1)}\ |l\ (m_l \pm 1)\ m_s\rangle \tag{7.9}$$
$$S_\pm|lms\rangle = \hbar\sqrt{3/4 - m_s(m_s \pm 1)}\ |l\ m_l\ (m_s \pm 1)\rangle \tag{7.10}$$

where l, m_l and m_s stands for the orbital, azimuthal and spin quantum numbers respectively and $|lm_lm_s\rangle$ from an orthonormal basis. The spin-orbit Hamiltonian can be written as

$$H_{SOC} = \xi \left[\frac{1}{2}(L_+ S_- + L_- S_+) + L_z S_z \right] \tag{7.11}$$

Substituting Eq.(7.11) into Eq.(7.6) one obtains:

$$\Delta E = -\xi^2 \sum_{u,o} \frac{1}{2} \left[\frac{|\langle o|L_+ S_-|u\rangle|^2}{\delta \epsilon_{uo}} + \frac{|\langle o|L_- S_+|u\rangle|^2}{\delta \epsilon_{uo}} \right] + \frac{|\langle o|L_z S_z|u\rangle|^2}{\delta \epsilon_{uo}}$$
$$\tag{7.12}$$

From Eq.(7.12) due to the orthonormality of the basis $|lms\rangle$ some selection rules. If the unoccupied and occupied states have the same l,m and s quantum numbers, the only non-zero contribution comes from the last term of Eq.(7.12), favoring an magnetization along the z-axis.

7.3 Di-iron Phosphide (Fe$_2$P) Crystal Structure

The di-iron phosphide (Fe$_2$P) crystal structure is Hexagonal C$_{22}$ with space group P$\bar{6}$2m, No. 189. It was first determined in 1959 by Rundqvist *et. al.* [61] and refined by Carlsson *et al.* in 1975 [62]. Fujii *et al.*[63] determined the unit cell parameters at 295 K as: a= 5.868 Å and c=3.455 Å. The Fig. (7.3) shows the Fe$_2$P crystal structure, the unit cell is
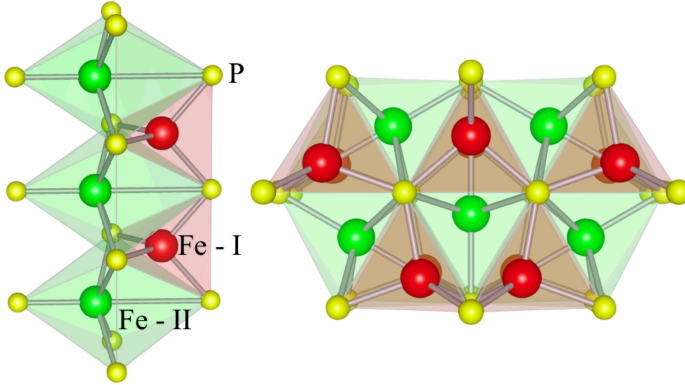

Figure 7.3. Fe$_2$P crystal structure (Hexagonal C$_{22}$, P$\bar{6}$2m, No. 189) Fe$_I$tetrahedral-sites (red), Fe$_{II}$ Pyramidal-sites (green) and P atoms (yellow).

composed of three Fe atoms occupying $3f$ sites (Fe$_I$), three Fe atoms occupying $3g$ sites(Fe$_{II}$), two P atoms at the $2c$ sites (P$_I$) and one P atom occupying $1c$ sites (P$_{II}$), 3 formula units (f.u.) in the unit cell. The two inequivalent Fe atoms have different environment. The Fe$_I$ atom is surrounded by four P atoms, with bonding distances ranging from 2.22 to 2.28 Å, as the P atoms form a tetrahedron structure, the Fe$_I$site is

called tetrahedron site. The Fe_{II} atom is coordinated by six P atoms, with bond lengths from 2.37 to 3.50 Å. The Fe_{II} site is called pyramidal site due to the arrangement of the P atoms.

The Fig. (7.4) shows the total energy as a function of the c/a ratio for the LDA, GGA and LDA + DMFT calculations. The LDA severely underestimates the c/a ratio, e.g. also underestimate the equilibrium volume (V_0) by 90 % see table 7.1. For GGA one obtains a better agreement withe the experimental value. The LDA+DMFT calculations show a general trend, as the U parameter increases the bulk modulus (equilibrium volume) decreases (increases).
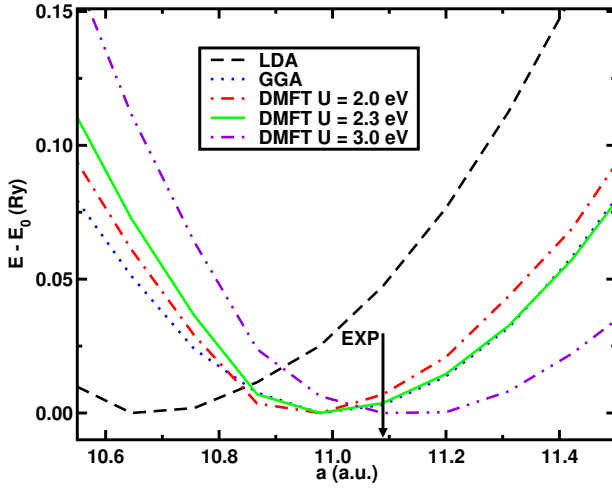

Figure 7.4. Total Energy versus c/a ratio for the Fe_2P LDA, GGA and LDA+DMFT for different Hubbard parameters U= 2.0 eV , 2.3 eV and 3.0 eV. The intratomic exchange parameter (J) is fixed at 0.9 eV.

Table 7.1. Fe_2P bulk modulus (GPa) and equilibrium volume V_0 ($\mathring{A}^3$).

	U (eV)	Bulk Modullus (GPa)	$V_0(\mathring{A}^3)$
GGA	-	201.4	100.78
LDA	-	258.6	92.21
exp.	-	174[a],165[b]	-
exp.	-	-	103.32[c]

[a]Paramagnetic, room temperature Ref.[64].
[b]Paramagnetic, room termperature Ref.[65].
[c]Paramagnetic, room termperature Ref.[63].

7.4 Magnetic Properties

There are several experimental studies concerning the ordering temperature, MAE, saturation moment, hyperfine field and isomer-shift of Fe_2P [66; 67; 68; 69]. In addition, a theoretical analysis was made earlier by Wohlfarth [70; 71], and a subsequent theoretical work addressed the magnetism of Fe_2P using electronic structure calculations [72; 73]. An excellent overview of the magnetic properties of Fe_2P and similar transition metal pnictides and chalcogenides can be found in Ref.[74].

Fe$_2$P is mainly ferromagnetic with a Curie temperature ($T_c = 216$ K) [74], at this temperature a first-order ferro-paramagnetic transition is observed, with a decrease of the a-axis and an increase of the c-axis [75], see Fig. (7.5). Small changes in the stoichiometry, by dopping or defects, can change the magnetic properties of Fe_2P. For 20% of As dopping, on the phosphorus site, the a (c) parameter increases (decreases) 1.85 % (0.96%), in a hexagonal structure. The altered structure leads to an increasing of the Curie temperature by 89% (T_c=411 K) and the total magnetic moment changes to 3.03 μ_b, an enhancement of almost 3%. A T_c of 450 K (370 K) is obtained by Si dopping with 8% (10%) concentration also in the P site [74].
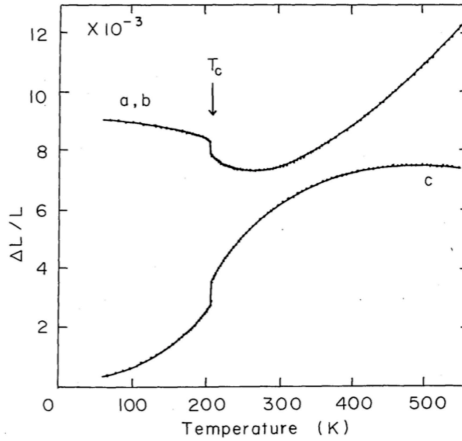

Figure 7.5. Lattice expansion of Fe_2P as a function of the temperature. adapted [75]

Table 7.2 shows LDA, GGA and LDA+DMFT total and site resolved magnetic moments, the calculations were performed at the experimental volume. The LDA+DMFT calculations were performed using the so called spin-polarized T-matrix fluctuation exchange solver (SPTF) [77] which is appropriate for moderate correlated systems. Furthermore the double counting problem was addressed using the so called sigma zero

Table 7.2. *Fe_2P total and site resolved spin moment, in μ_b.*

	Total	Fe_I	Fe_{II}	P_I	P_{II}
Ref.[76]⋆	2.94	0.69	2.31	-	-
Ref.[69]⋆	2.92	1.14	1.78	-	-
Ref.[72]†	2.94	0.96	2.04	-	-
GGA	3.03	0.84	2.24	-0.06	-0.05
LDA	2.96	0.84	2.14	-0.05	-0.04
U(eV)		LDA+DMFT			
2.0	2.98	0.83	2.17	-0.05	-0.05
2.3	2.98	0.83	2.18	-0.05	-0.05
3.0	2.99	0.82	2.20	-0.05	-0.05

* GGA † LDA ⋆ experimental

double counting [78], where we consider that LDA describes the well the orbital average zero frequency self energy (static self- energy).

All approximations give similar results for the Fe_I spin moment ad for the Fe_{II} LDA gives better results than GGA and DMFT. As the Hubbard parameter increases from 2.0 to 3.0 eV a slight increase in the total moment is observed. The agreement for site resolved spin moments is not so good, but the experimental value also have scattered data. Comparing the spin moment for different Fe sites one sees that Fe_{II} has a much bigger spin moment then Fe_I. For the Fe_I (tetrahedron) the proximity to the P atoms increases the hybridization, eg. the hopping, and the electrons can be seen as less spatially localized. Despite the fact that Fe_{II} is more localized, the difference in GGA and LDA spin moments is small the LDA + DMFT results are the middle way between the LDA and GGA results.

We investigated how the spin moment changes with the volume. Fig. (7.6) shows the total spin moment as a function of the volume. For smaller volumes the LDA, GGA and LDA+DMFT total spin moments approach the same value, due to the increasing Fe-P hybridization. In this regime electronic correlations are less pronounced and LDA, GGA and LDA + DMFT are expected to give similar results. In the opposite limit, large volumes, a similar behavior is observed, but in this case due to a saturation of the moments. The Fe_I and Fe_{II} site resolved spin moments are showed in the inset of Fig. (7.6). For the two sites a transition from a low to high spin state is observed. For the Fe_I a maximum value is observed and then a monotonically decrease. The maximum is different for the LDA, GGA and LDA + DMFT but the trend is the same. The Fe_{II} site a monotonical increase of the spin moment is observed for c/a ratio bigger then 11.0. The Fe_I and Fe_{II}
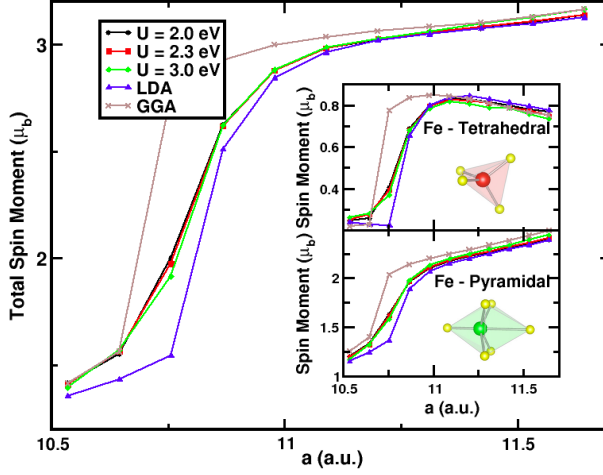
Figure 7.6. Total spin moment for LDA (blue) , GGA (brown) and LDA+DMFT for different Hubbard parameters U= 2.0 eV (black), 2.3 eV (red) and 3.0 eV (green). The insets show projected spin moment, for the Fe tetrahedral and pyramidal sites. The intratomic exchange parameter (J) is fixed at 0.9 eV.

GGA d-*states* projected density of states are showed in Fig. (7.7) for the smallest and largest volume. For both sites a narrowing of the d-band is observed as one goes from small to larger volume as expected.
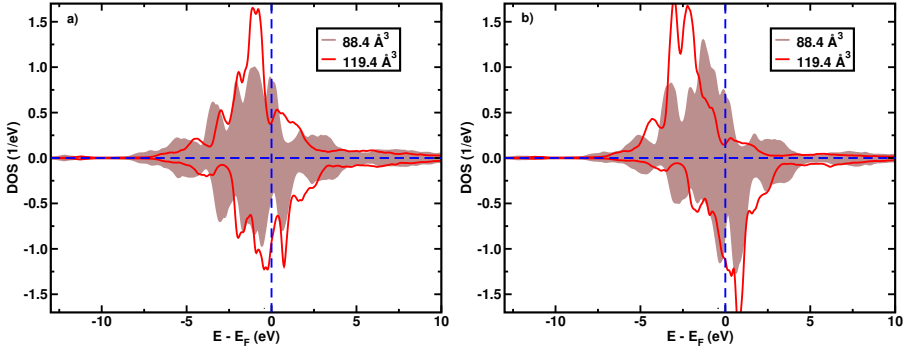

Figure 7.7. Site projected density of states (pdos) a) Fe_I and b) Fe_{II}. For the smallest (largest) volume shaded (red) area (lines).

7.5 First Principle MAE

The MAE was calculated by the magnetic force theorem [79]. Using Eq.(7) whereas $\hat{n}_1 = 001$ (c-axis) and $\hat{n}_2 = 100$. As Fe_2P shows an uniaxial magnetic anisotropy any choice of spin quantization axis in the

basal plane (ab-plane) will produce the same value of the MAE. On a simple model level, the uniaxial MAE can be treated in second-order perturbation theory, and computed as the difference of the second order correction to the energy ($E_q^{ss'}[\hat{n}]$) between two magnetization directions as in Eq.(7.13), with a sum over the sites q, over occupied (s) and unoccupied (s') spin characters, respectively; [80]

$$\Delta E_{SO} = \sum_{qss'} \Delta E_q^{ss'} = \sum_{qss'} \{E_q^{ss'}(\hat{n}_1) - E_q^{ss'}(\hat{n}_2)\}, \qquad (7.13)$$

where the energy correction is given by,

$$E_q^{ss'}(\hat{n}) = -\sum_{\mathbf{k}ij} \sum_{q'} \sum_{\{m\}} n_{\mathbf{k}is,qm,q'm'} n_{\mathbf{k}js',q'm'',q'm'''} \times$$
$$\frac{\langle qms|\hat{H}_{SOC}(\hat{n})|qm'''s'\rangle \langle q'm''s'|\hat{H}_{SOC}(\hat{n})|q'm's\rangle}{\epsilon_{\mathbf{k}j} - \epsilon_{\mathbf{k}i}}. \qquad (7.14)$$

In Eq.(7.14) there is a sum over $\mathbf{k}$ points in the Brillouin zone, i and j label the occupied and unoccupied states, s and s' run over the spin character of the states and m, m', m'', m''' run over the magnetic quantum numbers. The basis functions $|qlms\rangle$ are characterized by the site q, azimuthal (l), magnetic (m) and spin (s) quantum numbers and $\epsilon_{\mathbf{k}i}$ ($\epsilon_{\mathbf{k}j}$) are the electronic eigenvalues for the occupied (unoccupied) states. The hybridization is considered in the band character $n_{\mathbf{k}is,qm,qm}$, which allows mixing of basis functions on different sites. The $\hat{H}_{SOC}$ stands for the spin-orbit Hamiltonian.

The Fe environment plays a crucial role on the magnetic properties of Fe_2P, specially for the MAE. The MAE is mainly due to spin-orbit coupling (see 7.2). The material has an observed MAE of 500 μeV/f.u. [75] at T=4K, with the crystallographic c-axis being the magnetization easy axis. In general a large number of $\mathbf{k}$-points is necessary to guarantee the convergence of the calculated MAE. Fig 7.8 shows the MAE as function of the $\mathbf{k}$-point number, for T=295 K structural parameters. A value of 36002 $\mathbf{k}$-points , in irreducible part of BZ, was considered converged as the MAE deviates only 0.1 % in comparison with a 50626 $\mathbf{k}$-points calculation.

The main result is shown in Fig. 7.9, where the calculated MAE is displayed as a function of the strain. Note that here was used the room temperature lattice constant as reference level, having room temperature applications in mind. It is clear from the figure that theory reproduces the observed easy axis (0001) and that the calculated MAE is of the same order of magnitude as the experimental one. The theory overestimates the value of the MAE by 32 %, when a comparison is made between the experimental low temperature value (red square, taken at 4 K) and the
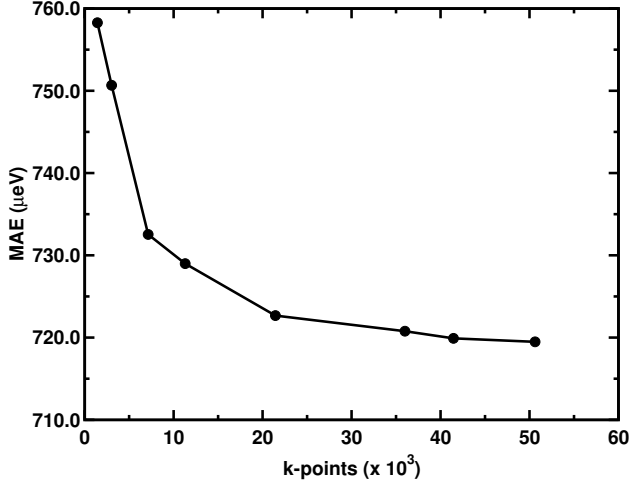
Figure 7.8. MAE as function of the **k**-points for the T=295 K structural parameters..

lattice parameters corresponding to this temperature (which in Fig. (7.9) corresponds to a - 0.55 %). The strain state of the low temperature lattice constant is calculated from the work of Fujii *et. al.* [68] who reported measurements for the thermal expansion of the Fe_2P in the temperature range of 60 to 550 K, see Fig (7.5). Using this thermal expansion data the 4 K lattice parameters were estimated. The agreement between calculated and measured MAE obtained here is typical, when compared to other calculations [51; 52; 81], and primarily reflects the extremely delicate nature of the MAE in general. A very important result shown in Fig. 7.9, however, is that with an applied strain to the lattice it is possible to influence the MAE quite substantially.

In these calculations, strain was applied, keeping a constant volume. Increasing the c value by 1% enhances the MAE by $\sim$ 15 %, which is the maximum value of the calculated MAE. For strain values higher than 1%, Fig. 7.9 shows that the MAE decreases almost linearly. Reducing the c-axis is not favorable for the MAE, here a monotonically decreasing trend is noticed, with a minimum observed at -8%. Unfortunately most dopings on the P site, e.g. with Si or B, results in a reduced c/a ratio [62; 63; 68; 75].

The magnetic moment of Fe_2P changes much less with strain when compared to the MAE, as the inset of Fig. 7.9 shows. At 1% strain the calculated moment is 3.03 μ_B/f.u., which is -0.4 % of the zero strained system. The magnetic moment increases however slightly for negative values of strain. Overall our calculated moments agree well with the observed number of 2.94 μ_B/f.u. [68].
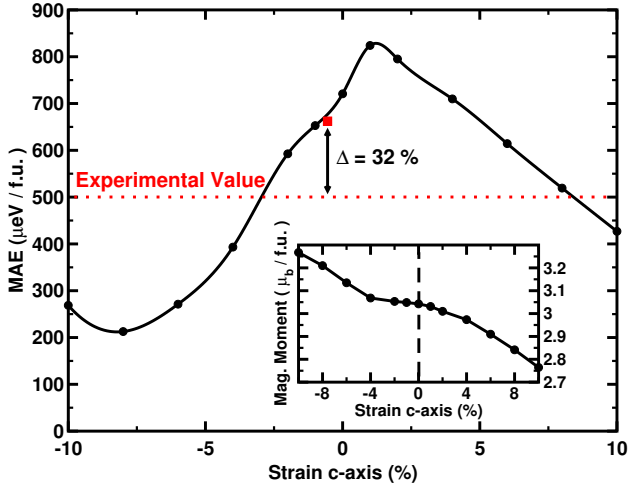
Figure 7.9. Calculated MAE as function of the strain. Positive values of the strain correspond to an increased c/a ratio (at constant volume). Positive values of the MAE correspond to the c-axis being the easy axis. The inset shows the calculated magnetic moment as a function of strain. The square (red) is the MAE value for the estimated 4 K lattice parameters.

The Fig. 7.9 shows data for a volume conserving strain (except the red square which corresponds to a volume which is minutely smaller than the volume used for the other data points). For comparison we also show in Fig. 7.10 the MAE as function of strain in two non-volume conserving regimes.

This involves strain of the c-axis while a and b are fixed as well as strain of the ab-axis while c axis is fixed. For c-axis (ab-axis) strain a maximum MAE value of 800 μeV (807 μeV) is obtained for 2% (-1%) strain. Experimental doping on the P site with B results in a reduced c/a axis (negative strain) and a reduced volume [62; 63; 68; 75], in this case a predicted MAE with doping is best evaluated by inspection of the non-volume conserving curve in Fig. 7.10. Doping with Si keeps the volume essentially constant while reducing the c/a ratio, and for this doping element the predicted MAE is best evaluated from the volume conserving curve, which shows a decreased MAE. The MAE was actually calculated using the structural cell parameters for 10 % Si doping [74], and 593 μeV MAE was obtained, showing the expected reduction. For 10% Si doping the experimental Curie temperature (T_c) is 370 K (an increase of 70 % when compared with the undoped case), which is promising for stabilizing a material which at room temperature has a large MAE. Further investigations are necessary to consider the chemical effect impact on the MAE.

Both these predicted changes of the MAE with doping rely on the applicability of the rigid band approximation. They have not been evaluated experimentally, and a verification or refutal of this prediction would be interesting.
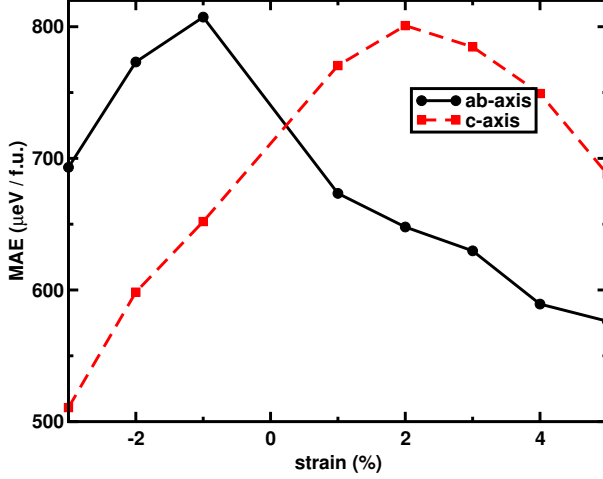

Figure 7.10. Calculated MAE as function of the strain of the c-axis with a and b fixed (red squares) and strain on the ab-axis with c fixed (black circles).

Since the electronic eigenvalues ($\epsilon_{\mathbf{k}i}$) appear in Eq.(7.14), it is relevant to inspect the band structure along the high symmetry lines of the hexagonal lattice. Hence, the calculated energy bands is showed in Fig. 7.11, where the thickness of the bands represents the weight of the Fe-II, l=2 and m=-2 state. The bands that contribute the most to the MAE are highlighted by the arrows 1 to 5. At $\frac{1}{4}$(K-M), arrow 1, the occupied and unoccupied bands have mainly character from l=2 and m=±2 quantum numbers, and these bands interact through the $l_z s_z$ term of the spin-orbit coupling (SOC) Hamiltonian, resulting in a large negative contribution. A similar mechanism is observed at $\frac{3}{4}$(Γ-A), arrow 4. This is illustrated further using a calculation with spin-orbit coupling included, in Fig. 7.12 a), in a region zoomed in around the Fermi level, see the highlighted areas. One can see the splitting of the bands when the spin quantization axis is along the 0001 crystallographic direction. The splitting of these bands is not observed for the 100 axis, as can be seen in Fig. 7.12 b). At arrows 2, 3 and 5 the occupied and unoccupied bands have different m quantum numbers, m=±2 and m=0 (m=±1) for the occupied (unoccupied) bands, the SOC interaction via the terms : $l_+ s_- + l_- s_+$, give large positive contributions. As a general rule if the occupied and unoccupied bands have the same (different) m quantum number, the magnetization is favored to lie along the 001 (100) axis [82].
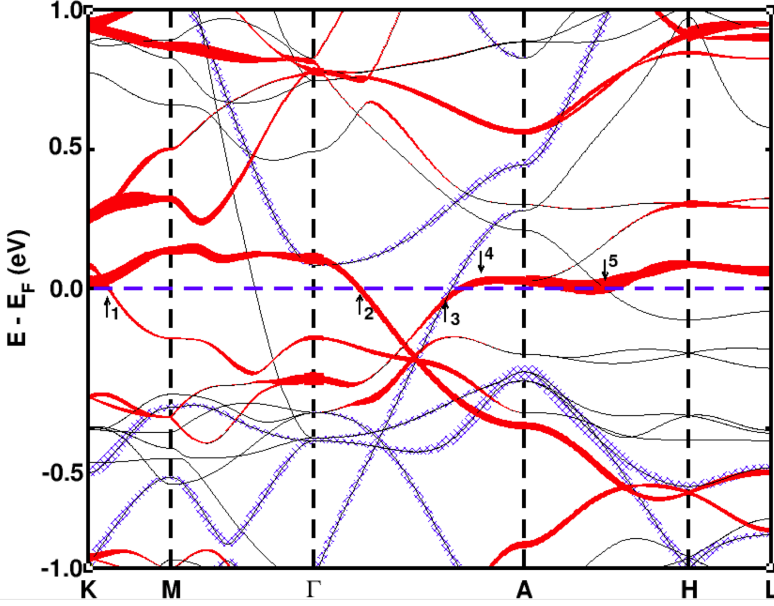
Figure 7.11. Band structure of Fe_2P calculated without spin-orbit coupling (the band thickness represents the weight of Fe-II, l=2 and m=-2 state). Red (solid) is the spin up character and blue (striped) is the spin down. The Fermi level (E_F) is placed at E=0.

To understand the enhancement of the MAE under uniaxial strain, the bandstructure was calculated for the 1 % volume conserving strain (Fig 7.13 a). The overall bandstructure is not changed, due to the strain, only a rigid shift is observed. Without SOC the flat bands around the A point lies on the Fermi level. As pointed out before these bands are split due to SOC for a magnetization along the 001 axis. One of the bands become fully occupied and the other fully unoccupied and given that these bands are very close in energy a large contribution to the MAE is expected. Indeed this is confirmed in Fig 7.13 b) (upper panel) where the MAE for each **k**-point ($E_{MAE}[\mathbf{k}]$) along the high symmetry lines of the hexagonal cell is showed, for the zero and 1% (volume conserving) strained system. For the zero strain one can see a sharp negative peak for the MAE (negative values favors the 001 axis) around arrows 1 and 4. For 1% strain the peak at arrow 4 gets broadened explaining the increasing of the MAE.

7.6 Conclusion

In conclusion the uniaxial MAE of Fe_2P was studied by *Ab Initio* calculations. The theory reproduces the observed 0001-easy axis with a MAE of 664 μeV/f.u. This should be compared to an experimental value of ~ 500 μeV/f.u. (2.32 MJ/m^3) This is an acceptable agreement between theory and experiment, when having in mind the extremely delicate nature of the MAE and the typical low energy differences associated with it. The size of the MAE of Fe_2P should be compared to other hard magnetic materials like FePt 1.2 meV/f.u. (6.6 MJ/m^3) [54] and $Nd_2Fe_{12}B$ 6.7 meV/f.u. (4.9 MJ/m^3) [83]. As to the magnetic moments our calculations give a value of 3.04 μ_B/f.u., which agrees well with the experimental moment of 2.94 μ_B/f.u.

The MAE origin was analyzed by a detailed band and **k**-point resolved property, and show that the positions of the different energy bands around the Fermi level critically determine that MAE. Since these bands can be moved up or down in energy with an applied strain, it seems that this is an important avenue with which to influence the MAE of Fe_2P and Fe_2P-based alloys. Consequently we find from our MAE calculations that it is possible to influence the MAE quite strongly with an applied strain, both in a volume conserving and a non-volume conserving mode. We showed that reducing the c value (in a volume conserving mode) by 1% enhances the MAE by $\sim$ 15 %. This opens up possibilities to use Fe_2P and alloys of this material, as a platform for searching for new permanent magnetic materials that don't contain rare-earth elements.
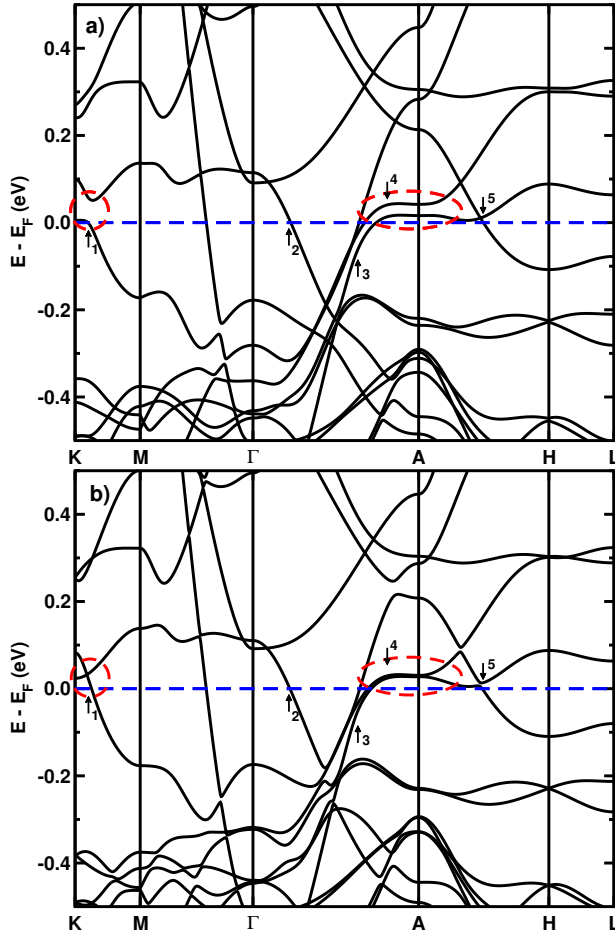
Figure 7.12. Zero strain band structure of Fe_2P calculated with spin-orbit coupling, magnetization along the a) 001 and b) 100 crystallographic axis. The Fermi level (E_F) is placed at E=0.
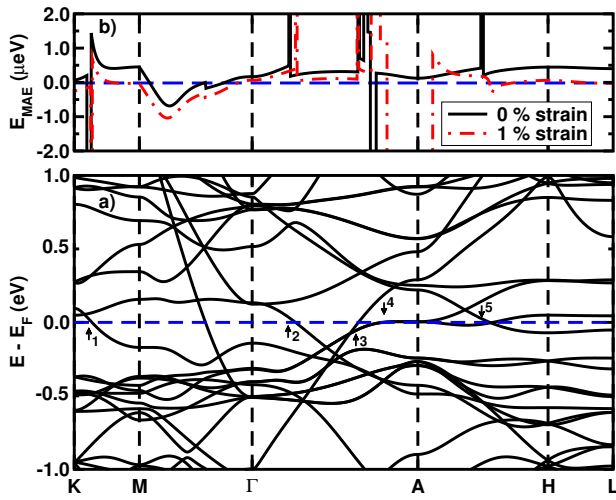
Figure 7.13. a) Band structure of Fe$_2$P calculated with 1 % of strain on the c-axis (the Fermi level (E$_F$) is placed at E=0) and b) MAE along the high symmetry directions.

8. On the icosahedral metal-phosphorus coordination in melliniite

The present chapter is based on the following publication:

1. K. Kadas, M. Costa, L. Vitos, Y. Andersson, A. Bergman and O. Eriksson. "On the icosahedral metal-phosphorus coordination in melliniite: a gift from the sky for materials chemistry". J. Mater. Chem. **22**, 14741 (2012).

8.1 Melliniite Properties and Crystal Structure

Recently a new mineral, melliniite, was reported in a meteorite from the Northwest Africa 1054 acapulcoite,[84] which belongs to the Collection of Meteorites of the Museo di Scienze Planetarie della Provincia di Prato. This mineral, which is unique in being found only in a meteorite sample, has ideally a chemical composition $(Ni,Fe)_4P$, with approximately 58 % Ni and 42 % Fe on the metal site (there is a very small amount of Co also on this site) [85]. The compound is reported to be opaque with a metallic luster, and the crystal structure was found to be cubic, space group $P2_13$, in the $AlAu_4$ structure type. In this structure the metal atoms occupy the 12b site which are effectively coordinated with fourteen neighboring atoms. Metal atoms are also found on the 4a site which is coordinated by three P atoms and nine metal atoms. The phosphorus atoms are located on the 4a site, and unlike other minerals on Earth, they are coordinated by twelve nearest neighboring metal atoms (the coordination is shown in Fig. 8.1). No other phosphide has been reported to have such high metal coordination. Generally phosphorus has nine metal neighbors, mostly in a tricapped triangular prismatic coordination [86]. In some very rare cases it can be ten-fold coordinated, e.g. in Co_2P [87].

Extraterrestrial iron-nickel phosphides have recently drawn significant attention due in part to the fact that it has been pointed out they are a possible source of phosphorus essential for the biomolecular building blocks of life [88] as well as being potential reservoirs of light elements in the Earth's core [85].

Until recently, five naturally occurring phosphides were known; schreibersite [88] (chemical formula $(Ni,Fe)_3P$), nickelphosphide [89] (chemical formula $(Ni,Fe)_3P$), barringerite [90](chemical formula $(Fe,Ni)_2P$), allabogdanite [86] (chemical formula $(Fe,Ni)_2P$) and florenskyite [91](chemical

formula FeTiP). Of these, schreibersite is the most commonly occurring mineral, and it is the most likely phase by which phosphorus was originally incorporated in deep planetary interiors [85]. The sixth naturally occurring phosphide is the recently reported melliniite [85]. The phase stability and in particular the crystal structure, as signalled by the phosphorous-metal coordination, of this newly discovered mineral is different from all known transition metal phosphides on Earth or synthesized in a laboratory, and is the focus of the present investigation.

The chemical binding between transition metals and elements with an open p-shell (e.g. pnictides) results in general in a strong covalent bond built up from d orbitals centered on the transition metal atoms and p orbitals centered on the element of the p-shell element [92; 93; 94; 95; 96]. This results in a directional bonding with a coordination lying between six (e.g. in TiC) and nine (e.g. in Fe_2P). It has been shown that a weaker, less directional metallic binding, primarily between the transition metal atoms, overlaps the covalent $d - p$ bond [97]. The dominance of the covalent $d - p$ bond is expected in transition metal phosphides, which is consistent with typical coordination numbers between six and nine. As mentioned, no compound have been found with a coordination exceeding ten [87]. In light of this paradigm, the recent discovery of a metal - phosphorous coordination of twelve in melliniite stands our as a chemical puzzle for this class of materials. An understanding of this seemingly new situation of the chemical bonding between transition metal atoms and pnictides, has relevance not only for geology and research on minerals. It could shine light on phenomena observed in physics, e.g. the superconductivity in magnetic Fe-pnictides,[98] as well as on engineering aspects of materials science, e.g. the potential of Fe_2P based materials as magneto-caloric cooling media [99]. We address this issue here, by first principles theoretical calculations, which are known to accurately describe the phase and structural stability, and in addition shine light on the nature of the chemical binding.

8.2 Balanced Crystal Overlap Orbital Poplulation

In order to investigate the nature of the chemical bonding between Fe-P (Ni-P) in Fe_4P (Ni_4P) compounds, we calculated the balanced crystal orbital overlap population BCOOP [100], which is a generalization of the crystal orbital overlap population (COOP) [101]. Consider the eigenvalues ϵ_n and eigenvectors $|n\rangle$ of the Kohn-Sham hamiltonian. As showed in chapter 3 the eigenvector can be expanded as

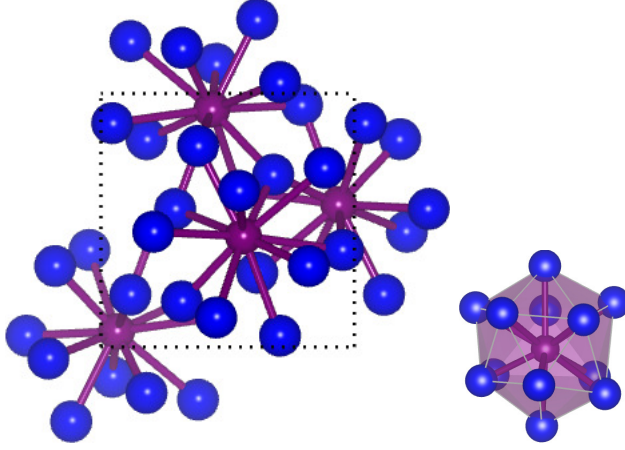$$|n\rangle = \sum_i c_i |i\rangle \tag{8.1}$$

Figure 8.1. The structure of melliniite. P and metal atoms are displayed by violet and blue, respectively. The right panel shows the icosahedral environment of the P atoms.

where the basis function $|i\rangle$ are atomic-like orbitals, in our particular case a muffin-tin orbital (MTO). The overlap between two basis states is

$$OP_{ij} = c_i^* c_j S_{ij} \qquad (8.2)$$

where the S_{ij} is the overlap between the state $|i\rangle$ and $|j\rangle$. The covalent bond is due to the overlap of wave function, so the OP_{ij} gives eigenvector contribution to the covalent bond between $|i\rangle$ and $|j\rangle$. For a solid one should take into account the **k**-dependence. So the COOP is defined as

$$COOP_{ij}(\epsilon) = \sum_{n\mathbf{k}} \delta(\epsilon - \epsilon_n(\mathbf{k})) c_i^* c_j S_{ij} \qquad (8.3)$$

where the COOP is positive for bonding contributions and negative for anti-bonding. In our case the full potential LMTO basis is used. Using such a basis the COOP for anti-bonding states shows a divergence, due to the non orthogonality. A more appropriate approach is the so called Balanced COOP (BCOOP). Before proceeding let us redefine the Kohn-Sham eigenvalues $\epsilon_n(\mathbf{k})$ and eigenvectors $|n,\mathbf{k}\rangle$ as

$$|\alpha\rangle = \sum_{i \in A(\alpha)} c_i(n, \mathbf{k})|i\rangle, \quad |n, \mathbf{k}\rangle = \sum_{\alpha} |\alpha\rangle \qquad (8.4)$$

where α stands for the type, azimuthal quantum number (l) and spin character. The BCOOP is defined as,

$$BCOOP_{\alpha_1\alpha_2}(\epsilon) = \sum_{n\mathbf{k}} \delta(\epsilon - \epsilon_n(\mathbf{k})) \frac{\langle\alpha_1|\alpha_2\rangle}{\sum_\alpha \langle\alpha|\alpha\rangle}, \qquad (8.5)$$

the denominator $\sum_\alpha \langle\alpha|\alpha\rangle$ is introduced in order to avoid the diverging due to non-orthogonality of the basis. The BCOOP follows the sign convention, as the COOP, positive (negative) values for bonding (anti-bonding) contributions.

8.3 Results and Discussion

The phase stability and electronic structure calculations were done by means of density functional theory using the PBEsol exchange-correlation functional.[102] The Kohn-Sham equations were solved using the Exact Muffin-tin Orbitals (EMTO) method.[103; 104; 105] The substitutional disorder of the metal atoms was taken into account using the Coherent Potential Approximation (CPA) [106; 107] as implemented in the EMTO-CPA method.[108] This scheme was proved to be an accurate approach in the theoretical description of the disordered solid solutions. In the self-consistent calculations, the one-electron equations were treated within the scalar relativistic and soft core approximations. The Green's function was calculated for 16 energy points. In the basis set s, p and d orbitals were included. All the EMTO calculations were spin polarized.

In addition to the EMTO calculations we performed calculations based on a full-potential linear muffin-tin orbitals method. These additional calculations we done primarily to analyze the chemical binding, by evaluation of the BCOOP. These calculations used 568 points in the irreducible part of the BZ, and involved an double spd-basis set for the transition metal atoms and a double sp-basis for the P atoms.

8.3.1 Phase Stability - $Ni_xFe_{1-x}P$

According to the measurements, $(Ni_{2.30}Fe_{1.64}Co_{0.01})_{\sum=3.95}P_{1.05}$ is the chemical formula of melliniite, ideally $(Ni,Fe)_4P$.[85] Here, metal atoms occupy 12b and 4a sites, but the distribution of Ni and Fe atoms over these sites are not known. Therefore, first, we examine the metal site preference in $(Ni,Fe)_4P$. In our calculations we considered Ni and Fe metallic components in the same ratio as in melliniite: $(Ni_{2.336}Fe_{1.664})P$. We considered three different structures. In the first structure, STR-I, Ni and Fe atoms are homogeneously distributed over the 12b and 4a

sites. In STR-II, only Ni atoms occupy metal 4a sites, and the remaining Ni atoms, as well as the Fe atoms are homogeneously distributed over the 12b sites. In STR-III, only Fe occupy metal 4a sites, and Ni and Fe atoms are homogeneously distributed over the 12b sites. Table 8.1 shows that STR-II is the most stable structure of these three, indicating that the metal 4a sites are preferably occupied by Ni atoms. The energy differences are rather small: 0.283 mRy/site for STR-I, and 1.059 mRy/site for STR-III. We calculate slightly different equilibrium volumes for these three structures, the differences being less than 2%. Within the present error bars, the theoretical bulk moduli are about the same. In the following, we consider STR-II as the ground state structure of $(Ni,Fe)_4P$.

Table 8.1. *Equilibrium volumes, total energies (with respect to the lowest configuration), and bulk moduli calculated for different structures of $(Ni,Fe)_4P$.*

Structure	V_{eq} ($Å^3$/atom)	E_{eq} (mRy/atom)	B (GPa)
STR-I	11.083	0.283	191.8
STR-II	11.158	0.000	191.4
STR-III	10.963	1.059	192.0

Next, we investigate the phase stability. First, we examine whether $(Ni,Fe)_4P$ is stable with respect to Ni_4P and Fe_4P standard states, i.e. the following reaction:

$$xNi_4P + (1-x)Fe_4P \rightarrow Ni_yFe_{4-y}P, \qquad (8.6)$$
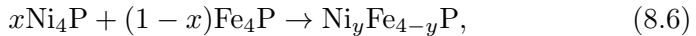
where x=0.584, and y=2.336. Here, Ni_4P and Fe_4P are calculated in the same structure as $(Ni,Fe)_4P$, i.e. cubic $P2_13$ structure.[85] We obtain for T=0 K a positive formation energy for reaction (8.6) with STR-II, ΔE_1=5.236 mRy/f.u., which means that at zero temperature $(Ni,Fe)_4P$ is not stable. However, at higher temperature, in fact already at room temperature, STR-II of $(Ni,Fe)_4P$ becomes stable, as it has negative free energy of formation (ΔF). For reaction (8.6), we calculate $\Delta F_1 = \Delta E_1 - TS$=-0.096 mRy/f.u. at T=310 K temperature, where the temperature effect is taken into account via the configurational entropy S.[109]

As a next step, we investigate the stability of the pure metal phosphides, Fe_4P and Ni_4P. To this end we calculate the formation energies of the following reactions:

$$Fe_3P + Fe \rightarrow Fe_4P, \qquad (8.7)$$

$$Ni_3P + Ni \rightarrow Ni_4P. \qquad (8.8)$$

Here, Fe_3P has I-4 structure with experimental lattice constants a=b=9.107 Å and c=4.460 Å.[110] Keeping the structure fixed, we determined the equilibrium volume, and obtained V_{eq,Fe_3P}=11.276 $Å^3$/atom for the equilibrium volume. We considered ferromagnetic Fe in body-centered cubic

(bcc) structure, and calculated $V_{\mathrm{eq,Fe}}$=11.151 Å^3/atom. Ni$_3$P is also of I-4 structure, with experimental lattice constants a=b=8.9499 Å and c=4.385 Å,[111] and we obtained $V_{\mathrm{eq,Ni_3P}}$=11.210 Å^3/atom for its equilibrium volume. Pure Ni was calculated in face-centered cubic (fcc) structure, with a theoretical volume of $V_{\mathrm{eq,Ni}}$=10.658 Å^3/atom.

We obtain at T=0 K a positive formation energy for reaction (8.7), ΔE_2=29.601 mRy/f.u., i.e. Fe$_4$P is not a stable compound. This is in line with the experimental Fe-P phase diagram,[112] according to which Fe$_3$P is the stable phase between 0 and 25 at.% P content.

For reaction (8.8), however, we calculate at T=0 K a negative formation energy, ΔE_3=-14.171 mRy/f.u. This means that Ni$_4$P is stable compared to Ni$_3$P and fcc Ni standard states. Nevertheless, in the experimental Ni-P phase diagrams [113; 114] Ni$_3$P is the stable phase between 0 and 25 at.% P content. Therefore our calculations predict a new phase in the Ni-P system, Ni$_4$P.

Finally, we examine whether (Ni,Fe)$_4$P is stable with respect to Ni$_3$P and fcc Ni, as well as Fe$_3$P and bcc Fe standard states, i.e. the following reaction:

$$x(\mathrm{Ni_3P + Ni}) + (1 - x)(\mathrm{Fe_3P + Fe}) \rightarrow \mathrm{Ni}_y\mathrm{Fe}_{4-y}\mathrm{P}, \qquad (8.9)$$
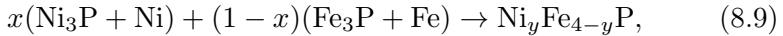
where x=0.584, and y=2.336. At zero temperature, the formation energy of reaction (8.9) is ΔE_4=9.274 mRy/f.u. for STR-II, indicating that (Ni,Fe)$_4$P is not stable. At elevated temperature, however, (Ni,Fe)$_4$P becomes stable: we calculate a negative ΔF_4 at temperatures larger than 540 K. The present phase stability calculations hence suggest that the stability of (Ni,Fe)$_4$P is due to its Ni content in combination with elevated temperatures and the configurational entropy, above 540 K. At room temperature this phase is meta-stable.

In Fig. 8.2 the calculated electronic density of states is shown for STR-II of (Ni,Fe)$_4$P. Here the spin-up and spin-down channels are displayed by black and red lines, respectively.The DOS is smoother than that of Fig. 8.3, due to alloying effects. We also note that no sharp peaks of the DOS curve are found at E_{F}, which is a pre-requisite for a material to be stable.[115] Furthermore, (Ni,Fe)$_4$P is magnetic: we calculate a magnetic moment of 2.24 μ_B for Fe atoms at 12b sites, and smaller magnetic moments for Ni atoms, 0.45 μ_B for Ni at 12b sites, and 0.21 μ_B for Ni at 4a sites.

8.3.2 Chemical Bond Analysis

A non spin-polarized BCOOP was calculated, and is analyzed below, with α_1= Fe 3d (Ni 3d) and α_2= P 2p. Fig. 8.3a (8.3b) shows the Fe$_4$P (Ni$_4$P) total density of states (DOS) and the Fe 3d (Ni 3d), P
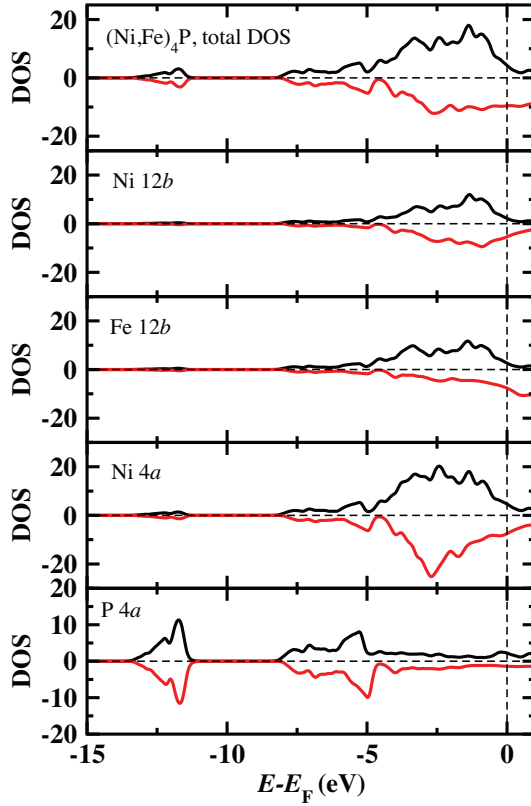
Figure 8.2. Electronic density of states calculated for structure STR-II (for details see text) of $(Ni,Fe)_4P$. Top: total DOS; lower panels: partial DOSs (in arbitrary units). E_F is denoted by a vertical dashed line.

$2p$ projected density of states (PDOS). The Fe $3d$ (Ni $3d$) states are located primarily around the Fermi level (E_F), starting from $\sim$ -5 eV and extending to a few electron volts above E_F. The P $2p$ states are located primarily between $\sim$ -8 and -5 eV. The hybridization (mixing of orbital characters) between the transition metal states and the P $2p$ states shows up in Fig. 8.3a (8.3b) as a tail of the P $2p$ PDOS that extends to higher energies and overlaps with the PDOS of Fe $3d$ states. This hybridization gives rise to a covalent bond, and one can from Figs. 8.3a and 8.3b note that the hybridization is stronger between Fe $3d$ and P $2p$ compared to that between Ni $3d$ and P $2p$. As a matter of fact, the hybridization between Ni $3d$ and P $2p$ is very weak, as Fig. 8.3b shows, suggesting a weaker covalent bonding in this situation.
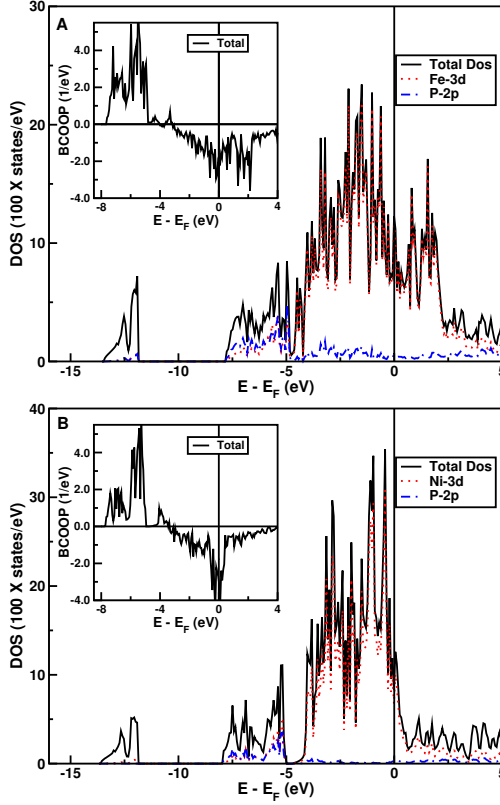
Figure 8.3. Total and projected density of states and BCOOP of Fe_4P and Ni_4P.(A) Fe_4P total density of states, Fe $3d$ and P $2p$ projected density of states and (B) Ni_4P total density of states, Ni $3d$ and P $2p$ projected density of states. The inset of A) (B) shows the total BCOOP between P $2p$ and Fe $3d$ (Ni $3d$) states (nearest-neighbors). The Fermi level is placed at $E=0$.

The inset of Fig. 8.3a (8.3b) shows the BCOOP curves between P $2p$ - Fe $3d$ (Ni $3d$) nearest-neighbors. Positive regions of the BCOOP curve represent bonding states whereas negative regions correspond to anti-bonding covalent states. The Fe_4P BCOOP curve shows that all bonding states and a fraction of the anti-bonding states are filled. In the Ni_4P BCOOP curve a similar picture is found, however with an important difference that the intensity of the binding states is smaller, and that a higher fraction of the anti-bonding states are filled, which is expected as Ni has two extra d electrons compared to Fe. The BCOOP analysis hence demonstrates that the Fe-P bond is a stronger covalent bond in comparison with the Ni-P bond, which is consistent with the analysis of the PDOS curves.
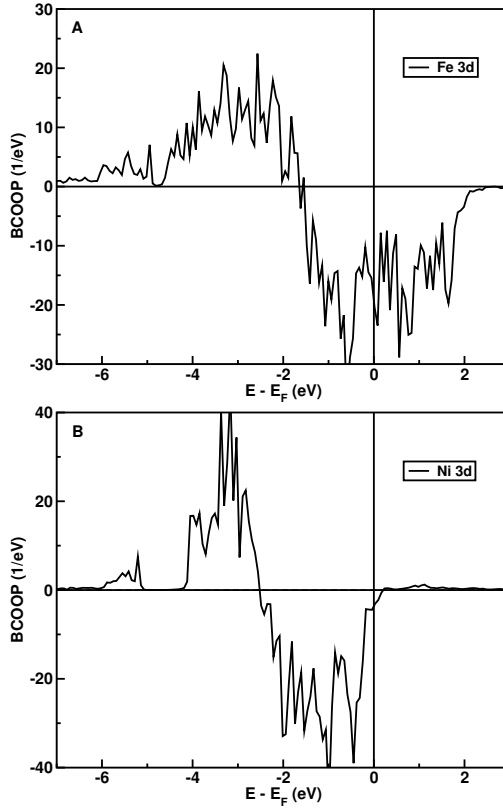
Figure 8.4. Total metal-metal BCOOP between the *d*-states of Fe (A) and Ni (B) (nearest-neighbors). The Fermi Level is placed at $E=0$.

Fig. 8.4 shows the Fe $3d$ (Ni $3d$) BCOOP curves, for the nearest-neighbors. A noticeable difference from the metal-phosphorus BCOOP (Fig. 8.3) is the intensity of the metal-metal BCOOP is higher in the last case. This difference is expected since the largest contributions for the PDOS, specially around the Fermi level, are mainly due to the Fe (Ni) $3d$ states. The Fe_4P BCOOP curve presents a similar picture to the Fe $3d$ - P $2p$ case, with all the bonding and a fraction of the anti-bonding states filled, showing a partially covalent character of the Fe-Fe bond. The Ni_4P BCOOP curve is quite different, with all bonding and anti-bonding states filled, only a small tail remains unoccupied, showing that the Ni-Ni bond has a less covalent character.

8.4 Conclusions

We have studied phase stability and chemical bonding in a recently discovered new mineral, melliniite, $(Ni,Fe)_4P$, using first princciples theory. In light of the PDOS and BCOOP analysis presented above, the twelve-fold coordination of the metal-phosphorous bond in $(Ni,Fe)_4P$ can be explained by the weak covalent nature of the Ni-P binding. The typical nine-fold coordination of the metal-phosphorous bond is found in stable compounds, with strong covalent binding. $(Ni,Fe)_4P$ is meta-stable at room temperature, due to the weakened strength of the Ni-P bond. The binding between Fe and P, in combination with finite temperature effects and configurational entropy, stabilizes the material above 540 K. The weakened nickel-phosphorous binding, however, allows for the observed, unique twelve-fold coordination of the phosphorous atom.

9. Strong Correlation of Fe Impurities on a Cs host

The magnetic properties of most elements can be drastically modified by combining them to form compounds. An example of this is the ferromagnetic compound $ZrZn_2$, which is formed by two elements that in pure form do not display any ordered magnetism [116; 117]. Another example is YCo_2, a non-magnetic compound (with a metamagnetic phase transition) [118] containing an element that in pure form is a ferromagnet with significant saturation moment and ordering temperature. Another way to influence the magnetic properties of a material is to form inclusions of one element in a host material. An example that stands out here is Fe impurities in a Pd host, where the normally non-magnetic Pd host becomes strongly spin-polarized due to the proximity to the magnetic Fe atom [119; 120; 121]. In this case a large number of Pd atoms become spin-polarized, causing every Fe atom to be associated with a large moment of 9-12 μ_B.

Recently much attention has been devoted to Fe impurities in Cs and other alkali metals. The reason for this interest is that Cs, according to the analysis of Wigner [122] and Overhauser [123], is close to a magnetic state, since it has a very small electron concentration (the r_s value is 6.6). Hence one may speculate that the inclusion of small amounts of magnetic elements in Cs, e.g. Fe or Co, could provide an exchange field that would push the host material to a magnetic ground state. Moreover, similarly to what happens for Pd, magnetic inclusions in Cs could generate a cloud of spin-polarized atoms around the magnetic impurities. This idea was indeed tested experimentally in a series of experiments of Fe and Co in Cs [124; 125; 126; 127], and large moments were reported. It was however argued that these large moments were not due to a polarization of the Cs host but more to the fact that the 3d shell of the Fe and Co impurities could assume an atomic-like electronic configuration, with atomic moments of 6 μ_B/atom [128; 129]. In fact first principles calculations, based on the density-functional theory in the local density approximation (DFT-LDA), support the fact that the polarization of the Cs host atoms is very small [129; 130]. Nevertheless, experiments for Fe and Co doped Rb and K [127] point to measured moments that are too large to be explained by atomic theory.
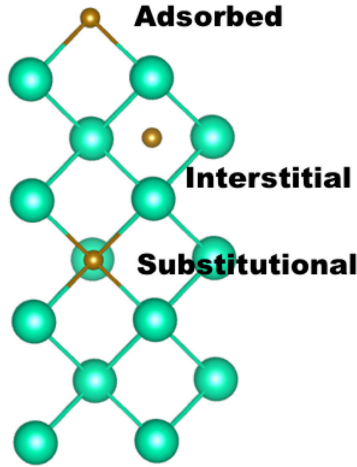
Figure 9.1. Different positions of the Fe impurity in Cs(001) host.

9.1 Breakdown of the Band Picture

These materials have also been subjected to spectroscopical studies in the form of Fe atoms adsorbed on the different alkali surfaces [131]. The investigations involved both an experimental part and a theoretical part, the latter being based on the combination of DFT-LDA and dynamical mean field theory, a computational scheme that is usually addresses as LDA+DMFT.

In this way the authors could investigate the correlated electronic structure with the inclusion of proper many-body effects. From this work it was concluded that Fe in Cs is a rather weakly hybridizing system, in which the 3d states form essentially a localized/atomic electronic configuration, a conclusion which is in line with the suggestions of Refs. [128] and [129].

In this chapter we provide a comprehensive LDA+DMFT study of the correlated electronic structure of Fe in Cs, focusing on the different positions that the Fe atoms can assume in the host: substitutional impurity in the bulk Cs, adsorbed on top of a Cs(001) surface and absorbed in an interstitial sub-surface site. The Cs bulk was considered in the bcc crystal structure [132]. The Cs(001) surface was modeled with 7 slabs and the Fe adsorbed was arbitrary relaxed to 60 % of the bulk value in the z direction, see Fig. 9.1. The smallest distance allowed between an impurity and its image was considered to be about 12 Å. A Monkhorst-Pack mesh of 7x7x7 (7x7x1) was used for the bulk (surface) calculations.

9.2 Hubbard I and Exact Diagonalization

We have performed simulations by means of a Full-Potential Linear Muffin-Tin Orbital (FP-LMTO) code [133; 134], whose LDA+DMFT implementation has been thoroughly described elsewhere [135; 136; 137; 138; 139]. In the LDA+DMFT scheme the lattice problem is mapped onto the problem of an impurity embedded in a fermionic bath, which reduces the complexity of the problem by freezing the spatial fluctuations but including all the dynamical quantum fluctuations. As a result of the mapping into an effective single impurity model, the DMFT solution is local in character, and becomes exact in the limit of infinite coordination number.

The effective impurity problem can be solved through different techniques. The choice of the solver is dependent on the system under consideration, and on the properties one wants to calculate, and on the desired accuracy. In this work the Hubbard-I approximation (HIA) and the Exact Diagonalization (ED) solver were used, and are briefly described in the following. The HIA is suited for very localized systems, where the hybridization of the atomic impurity with the fermionic bath can be totally neglected. This assumption is generally true for *f*-states, and sometimes also for *d*-states, usually in compounds like complex oxides. The ED solver can be considered as the natural extension of the HIA: the hybridization with the fermionic bath is not completely neglected but approximated by means of a few fictitious bath orbitals [139]. The Hamiltonian that describes the local problem becomes:

$$
\begin{aligned}
\hat{H} = \sum_{ij}(\hat{H}_{ij}^{LDA} - \hat{H}_{ij}^{DC})\hat{c}_i^\dagger \hat{c}_j + \sum_m \epsilon_m \hat{c}^\dagger \hat{c} \\
+\frac{1}{2}\sum_{ijkl} U_{ijkl}\hat{c}_i^\dagger \hat{c}_j^\dagger \hat{c}_k \hat{c}_l + \sum_{im}(V_{im}\hat{c}_i^\dagger \hat{c}_m + H.c.)
\end{aligned}
\tag{9.1}
$$

The indices i,j,k and l label the impurity correlated orbitals, e.g. the Fe *d*-states, while m labels the bath orbitals, e.g. the fictitious states derived from the Cs *sp*-states. The H_{ij}^{LDA} is obtained from the full LDA Hamiltonian projected on the correlated orbitals. The third term of Eq. (9.1) describes the local electron-electron interaction, and the U_{ijkl} matrix can be written in terms of the Slater integrals (F^n, n=0,2,4 for d electrons) times the Gaunt coefficients [8]. The parameters ϵ_m represent the energy positions of the bath orbitals, while V_{im} are the hybridization strengths. In the HIA the hybridization is totally neglected, therefore ϵ_m and V_{im} become trivially zero. In this case bath and localized states are decoupled, and the problem is atomic-like [138]. In ED the parameters defining the bath orbitals are chosen by means of a numerical fitting, described in detail in Ref. [139]. Once the Hamiltonian in Eq. (9.1) has

been set up, the problem can be solved exactly by calculating the ground-state many-body wavefunction. From the latter, one can finally obtain the local Green's function (and related properties) through the Lehmann representation [139]. Before describing the computational details, the double counting term H_{ij}^{DC} must be specified. This term is used to remove the contributions of the local Coulomb interaction U_{ijkl} already contained in the LDA Hamiltonian. For the HIA and the ED solver we find it convenient to use the photoemission data to set H_{ij}^{DC} manually, in order to fix the main occupied peak at the correct position.

The method described above has been used for LDA+DMFT simulations of Fe impurities in Cs, using both the HIA and the ED solver. Concerning the construction of the correlated d-orbitals, only one kinetic energy tail was used, similarly to what done in Ref. [139] for the transition metals monoxides. The Slater parameters describing the U_{ijkl} matrix were constructed by following the prescription of Ref. [131]. The Hubbard parameter U (F^0) is very sensitive to the environment, and in a free atom can be as high as 30 eV. In a solid, due to the screening effect, U ranges from 2-8 eV. As the aforementioned studies point to that Fe is in a atomic-like environment, U=8.0 eV was used. The intratomic exchange parameter J was used to construct F^2 and F^4 as in Ref. [42; 43; 44].
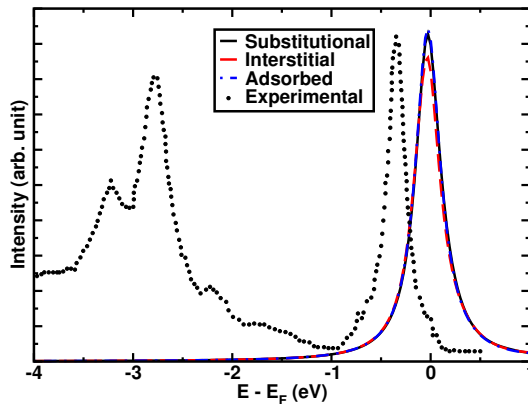

Figure 9.2. PDOS for the Fe d-states in LDA for different positions: substitutional position in the Cs bulk (solid black line), interstitial position in the first sub-layer of the Cs(001) surface (dashed red line), adsorbed position on top of the Cs(001) surface (dotted-dashed blue line). The experimental photoemission spectrum (full black circles) from Ref. [131] is also shown.

9.3 Results and Discussion

9.3.1 Spectral Properties

In Fig. 9.2 the projected density of states (PDOS) of the Fe d-states in LDA is reported, for the substitutional, interstitial and adsorbed impurities, together with experimental data from photoemission spectroscopy [131]. The aforementioned large Fe magnetic moments seems incompatible with the experimental spectrum and the Stoner criteria. As the Stoner parameter $\mathcal{I}$ is nearly independent of the environment, one should expect a large density of states at the Fermi level in order to explain the large spin moment. This apparently contradiction is a reflection of the band picture breakdown. The Stoner criteria was derived considering electrons as waves propagating through the crystal, which is not valid anymore. Nevertheless LDA shows a large value of the density of sates. It is clear that LDA does not capture the correct physics. The experimental spectrum exhibits multiplet-like features, while the LDA PDOS has only one peak just on top of the Fermi level. It is evident that the predicted spectral properties do not show any correspondence with the experimental data. To use the LDA+DMFT scheme its important to know the correct occupation of the correlated orbitals, in this case the d orbitals. Depending on the characteristic of the host, the Fe atoms can assume different electronic configurations. In the Ref.[131] the authors considered a d^7 configuration for the Fe impurity. Our LDA calculations gave an occupation of six electrons we decided to investigate both configurations.

9.3.2 Hubbard I - d^7

In Fig. 9.3 top panel, the experimental spectrum of Fig 9.2 is compared to the PDOS for the Fe d-states calculated with the LDA+DMFT scheme with the HIA. It is possible to recognize the multiplet features. The first peak (at -0.35 eV) is used to set the double counting term, as explained above, and by construction should be on top of the experimental one. The second experimental peak is at around -2.3 eV, and is visible also in the calculations. Despite its position is correctly predicted by the theory, its intensity is highly overestimated. The third peak, at -2.8 eV, shows a reasonable agreement correspondence between experiment and theory. Finally the position of the fourth peak is well reproduced by the theory, at around -3.2 eV, but its intensity is strongly underestimated. The intratomic exchange parameter J was seted to 0.9 eV.
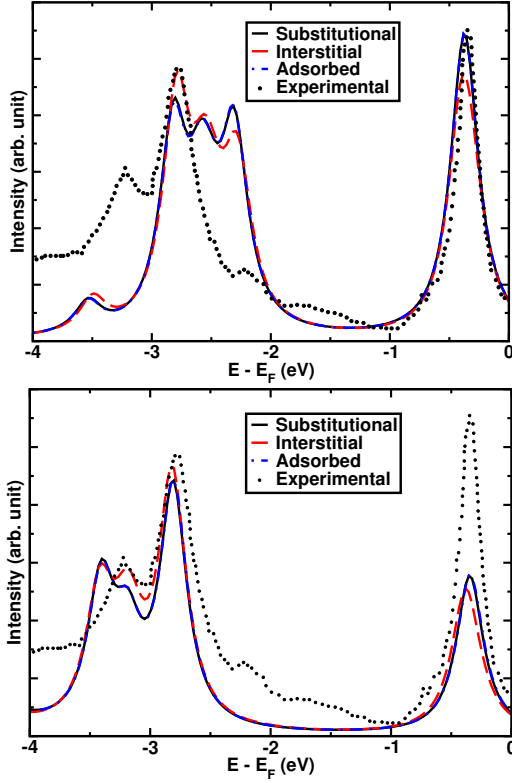
Figure 9.3. PDOS for the Fe *d*-states, in d^7 (top panel) and d^6 (bottom panel) configuration using HIA for different positions: substitutional position in the Cs bulk (solid black line), interstitial position in the first sub-layer of the Cs(001) surface (dashed red line), adsorbed position on top of the Cs(001) surface (dotted-dashed blue line). The experimental photoemission spectrum (full black circles) from Ref. [131] is also shown.

9.3.3 Hubbard I - d^6

Now we compare the experimental spectrum with the PDOS for a d^6 configuration, as showed in Fig. 9.3 bottom panel. The agreement is much better, in comparison with the d^7. The distance between the first and third peaks is in perfect agreement, nevertheless the second peak is absent in this configuration. The third peak is slight shifted to higher energies (at -3.4 eV). The intratomic exchange parameter J was seted to 0.75 eV. We should stress that the distances between the calculated peaks are in a good agreement with experiment. Probably a better agreement can be obtained for this atomic-like simulation by tweaking the exact values of the Slater parameters F^2 and F^4, but this (tedious) procedure

would not lead to any additional significant information, and therefore was not done.

Table 9.1. *Energies ϵ_m (eV) and hybridization strengths V_m (10^{-2} Ry) of the fictitious bath orbitals used in the ED solver. The last column contains the degeneracy of each orbital, this being related to the symmetry of the local Hamiltonian in the absence of spin-orbit coupling and spin-polarization.[139].*

	ϵ_m(eV)	$V_m(10^{-2}$ Ry)	DEG
Substitutional	3.373	0.529	6
	6.582	0.541	4
Interstitial	4.732	1.080	2
	4.459	0.886	4
	4.947	0.811	2
	4.721	0.491	2
Adsorbed	4.266	0.754	2
	5.489	0.617	2
	3.144	0.391	4
	2.201	0.353	2
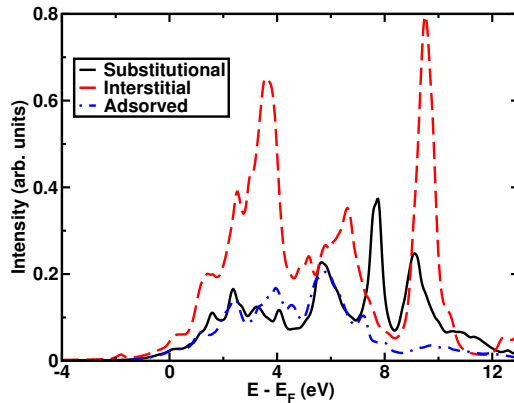
Figure 9.4. Hybridization strength of the Fe d-states in LDA for different positions: substitutional position in the Cs bulk (solid black line), interstitial position in the first sub-layer of the Cs(001) surface (dashed red line), adsorbed position on top of the Cs(001) surface (dotted-dashed blue line).

More interesting is the analysis of the effects due to the hybridization of the atomic impurity with the surrounding electrons. In Fig. 9.4 we show the strength of the hybridization of the Fe d-states, obtained from the absolute value of the trace of the imaginary part of the hybridization function $\Delta(E)$ [139] over all orbitals. As expected, the hybridization is very small for all the possible positions of the impurity, especially in the occupied part of the spectrum. In the unoccupied part, the Fe at the interstitial position shows the strongest hybridization, while the Fe at

the adsorbed position has the weakest one. The effects of the hybridization on the spectrum become clear when LDA+DMFT simulations are performed with the ED solver. The hybridization function was fitted by using 10 fictitious bath states, which are obtained through the already mentioned fitting algorithm of Ref. [139]. These orbitals are fully specified by the parameters ϵ_m and V_m, which are reported in Table 9.1.

Figure 9.5. Occupied part of the PDOS for the Fe d-states in a d^7 (top panel) and d^6 (bottom panel) configuration using ED for different positions: substitutional position in the Cs bulk (solid black line), interstitial position in the first sub-layer of the Cs(001) surface (dashed red line), adsorbed position on top of the Cs(001) surface (dotted-dashed blue line). The experimental photoemission spectrum (full black circles) from Ref. [131] is also shown.

9.3.4 Exact Diagonalization

The occupied part of the ED spectrum for the three considered impurity positions for the d^7 (d^6) configuration is shown in Fig. 9.5 top panel (bottom panel). The ED spectrum is very similar to the HIA spectrum,

except for some rigid shift for the d^7 configuration. An additional thing to notice, in relation to the previous considerations, is that for ED the double-counting correction does not fix the position of the peak exactly, but the latter one can adjust with respect to the hybridization effects.

Finally we have also investigated the unoccupied part of the spectrum, as reported in Fig. 9.6. This was motivated by the fact that in this region the hybridizations in Fig. 9.4 exhibit the largest contributions. In the inset of Fig. 9.6 the HIA results are reported. As expected no major differences can be seen, due to that the hybridization is not considered in this method. Instead, for the ED spectrum, the hybridization causes the atomic-like peaks to spread into broader structures. Significant differences appear, in particular between the adsorbed and the substitutional (or interstitial) impurities in the case of the d^7 configuration. As for the d^6 configuration the substitutional and interstitial impurities unoccupied spectrum are very similar as the adsorbed is broaded. This result is very interesting, since it offers the possibility of determining the effective position of the impurities in the host by performing an inverse photoemission experiment.

9.4   Conclusion

We performed LDA+DMFT calculations to investigate the spectral properties of Fe impurities in Cs, for both bulk and surface hosts. It was shown that pure LDA calculations lead to a very poor description of the spectral properties with respect to the experimental photoemission data. The Hubbard-I approximation is very successful in reproducing the experimental spectra, but our calculations do not show any significant difference among the impurity densities of states at the three analyzed positions within the Cs host for both configurations. These results are confirmed also in the LDA+DMFT simulations with the ED solver, where the hybridization between impurity and host is considered explicitly. Despited the better agreement of the d^6 spectrum, there are some features not captured, as the small second peak in the experimental spectrum. We speculate that the experimental spectrum could be explained by a mixed of impurities in the d^6 and d^7 configurations, further investigations are necessary. Finally we have shown that the most differences between the theoretical spectra for the different positions lay in the unoccupied part. This suggests that one can use inverse photoemission spectroscopy, which probes the unoccupied electronic excitations, to identify in which site the impurity is located.
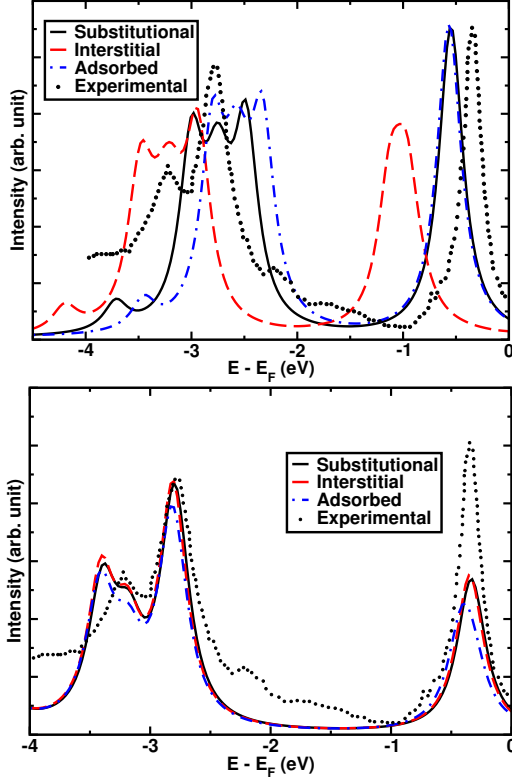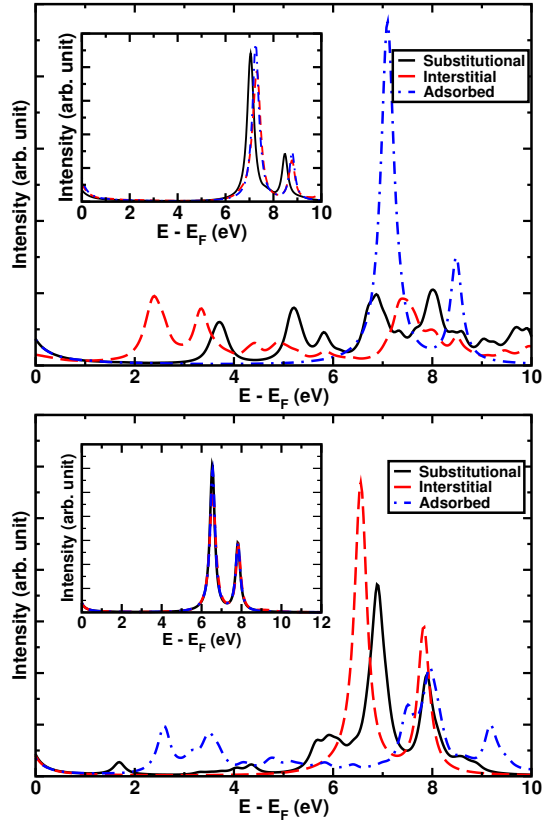
Figure 9.6. Unoccupied part of the PDOS for the Fe d-states in a d^7 (top panel) and d^6 (bottom panel) configuration using ED for different positions: substitutional position in the Cs bulk (solid black line), interstitial position in the first sub-layer of the Cs(001) surface (dashed red line), adsorbed position on top of the Cs(001) surface (dotted-dashed blue line). The inset shows the corresponding curves for the HIA in different positions.

10. Magnetism of supported clusters

Imagine the possibility of building a device atom-by-atom, with a kind of Fordism of the atomic world, one can call it molecular manufacturing or the bottom-up approach. At this point this is still a dream, despite some attempts. Nevertheless since the invention of the scanning tunneling microscope (STM), this partially became feasible. With the STM one can probe and manipulate atoms, at an extend that in 1989 researchers at IBM who manage to write the logo of the company using Xe atoms on a surface. Using the STM one can build from adatoms to elliptic corrals supported on surfaces and several other geometries. This supported clusters also draw attention from the information storage point of view, as a possible candidate for the next generation of hard drives.

In this work we investigate the magnetic configurations of supported Mn adatoms, dimers and triangular trimers. The aim of the work is to understand the role of the substrate in the final magnetic configuration. The substrates considered are non-magnetic Cu(111) or ferromagnetic Cu/Co/Cu(111) and Co/Cu(111). We considered an out-of-plane magnetization for both Co thin films [140]. We used the real space linear muffin-tin code [23], all calculations were perform with spin-orbit, e.g. the magnetic configurations are coupled to the lattice.

10.1 Adatom

We considered two magnetic configurations: Ferromagnetic (FM) and antiferromagnetic (AFM) coupling between the adatoms and the substrate. For an Mn adatom on the Cu(111) surface, states with FM and AFM coupling are degenerated. This is expected as the induced magnetic moment of the Cu atoms, in the surface, are almost zero ($=0.01\mu_\beta$)
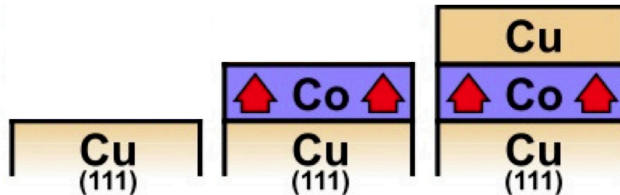

Figure 10.1. The surfaces considered a) Cu(111), b) Co/Cu(111) and Cu/Co/Cu(111).

Table 10.1. *Spin and Orbital Moments (μ_β) and J_{ij} (meV / atom) for Mn adatom. The value in parenthesis are the distance (Å) between the Mn and Co.*

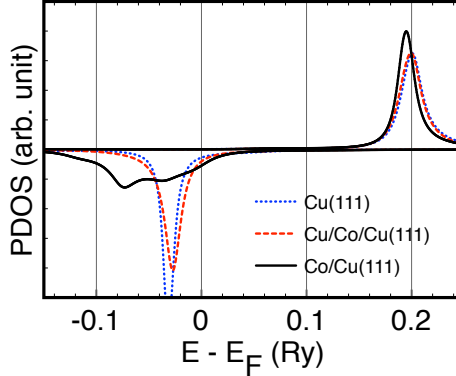|	Spin	Orbital	J_{ij}^{Mn-Co}
Cu(111)	4.37	0.04	-
Cu/Co/Cu(111)	4.37	0.04	-1.10(5.11)
Co/Cu(111)	4.28	0.02	-17.54(2.56)

Figure 10.2. Local density of states for the Mn adatom in, AFM configuration, on a Cu(111), Cu/Co/Cu(111) and Co/Cu(111) surfaces

as the orbital moments. Table 10.1 shows the values of the magnetic moment, orbital moment and the exchange coupling (J_{ij}) between the Mn and Co, the minus sign indicates an AFM coupling.

In the case of the Cu/Co/Cu(111) the Mn couples AFM to the surface. The magnetic and orbital moments have the same value of the Cu(111) surface, showing that the hybridization is most due to the Cu atoms, despite an nonzero exchange coupling to the Co layer. The same AFM coupling is observed for the Co/Cu(111) surface, but now the magnetic and orbital moment decreases, this is expected due to a higher hybridization with the Co atoms.

The local density of states (LDOS) for a Mn adatom is showed in Fig. 10.2 a). One can see a larger broadening in the d-resonance for the Co/Cu(111) surface. This can be explained by the *d-d* hybridization of the Mn and Co atoms in the first layer. The hopping between the full occupied majority Mn *d*-band (spin down character) and the half-filled minority Co *d*-band, of the same spin character, showed at Fig. 10.3 is increased as the bands have the same spin character. In principle one should have expected lower the spin moment for the adatoms but as the bands of Mn and Co have the same spin character a level repulsion will appear, pushing these bands to lower energies not allowing them to cross the Fermi level [141].
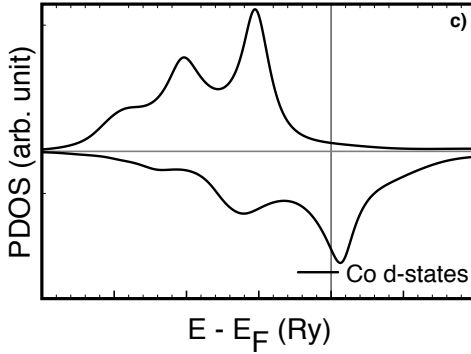
Figure 10.3. Local density of states for one Co atom of the Co/Cu(111) surface.

Table 10.2. *Spin and Orbital Moments (μ_β) and J_{ij} (meV / atom) for Mn dimer. The value in parenthesis are the distance (Å) between the Mn and Co.*

	Spin	Orbital	J_{ij}^{Mn-Mn}	J_{ij}^{Mn-Co}
Cu(111)	4.33	0.04	-41.82	-
Cu/Co/Cu(111)	4.33	0.04	-41.89	-2.26(4.43)
Co/Cu(111)	4.22	0.05	-40.43	-23.34(2.56)

10.2 Dimers

We performed collinear and noncollinear calculations for Mn dimers, since it was recently reported by S. Lounis *et. al.* an noncollinear state for Mn dimers on Ni(111) surfaces [142]. For the collinear calculations three magnetic configurations were considered: FM were the adatoms couples ferromagnetic between each other and with the surface, AFM where the adatoms couples ferromagnetic between each other and antiferromagnetic with the surface and a ferri where the adatoms couples antiferromagnetic between each other.

For an Mn dimer the ferri state was found to be more stable for the Cu(111) and Co/Cu(111). As for the Co/Cu(111) surface the AFM collinear states is obtained. In the case of Cu(111) and Cu/Co/Cu(111) two degenerate states were found, with the spins parallel and perpendicular to the plane. In all cases collinear solutions was found.

10.3 Triangular Trimers

For triangular trimers the picture changes, as in general Mn nearest neighbors atoms couples AFM , an phenomenon known as magnetic frustration [143; 144; 145] will play a role, in this triangular shape it is not possible for the Mn atoms been AFM with its neighbors, so the mini-

Table 10.3. *Spin and Orbital Moments (μ_β) and J_{ij} (meV / atom) for Mn timer in a triangular shape. The value in parenthesis are the distance (Å) between the Mn and Co.*

	Spin	Orbital	J_{ij}^{Mn-Mn}	J_{ij}^{Mn-Co}
Cu(111)	4.26	0.045	-47.45	-
Cu/Co/Cu(111)	4.33	0.04	-45.02	-2.22 (4.43)
Co/Cu(111)	4.28	0.02	-40.26	-19.65 (2.56)

mum energy is a solution with the magnetic moments forming and 120° for each pair of atoms, this is the case for Mn on the Cu(111) surface as showed in Fig. 10.4 a). Such noncollinear states was reported for an monolayer (ML) of Mn on Ag(111) using an spin-polarized scanning tunneling microscopy (Sp-STM) [146]. An frustrated state is also observed for the Cu/Co/Cu(111) surface, in this case there is a competition between the intra-cluster exchange coupling (J_{intra}) and the coupling of the atoms cluster with the Co monolayer J_{Co}. The Table 10.3 shows the values for the J_{ij} for the Mn trimers, the intra-cluster exchange coupling is much higher for the Cu/Co/Cu(111), this is reflected in final magnetic configuration being very similar to the Cu(111), see Fig 10.4 b).

For the Co/Cu(111) the situation gets more interesting, an magnetic profile where the moments are forming an angle of $\sim 10.6°$, between the Mn atoms, pointing into the surface Fig 10.4 c). Once again the magnetic frustration plays a role, only now the exchange coupling with the Co ML is relevant, the J_{Co} is about half of J_{intra} and this competition gives rise to such configuration.

10.4 Conclusion

We showed that the well known magnetic frustration in Mn triangular trimers is suppressed when these trimers are direct contact with the Co monolayer. The competition between the Mn-Mn and Mn-Co AFM coupling is the responsible for the magnetic profile showed at Fig. 10.4 b). The LDOS of the Mn adatoms shows a very narrow band, for the Cu(111) and Co/Cu(111) surfaces. It would be interesting to investigate how a proper treatment of the strong correlations, associated with these narrow bands, would change the above results.
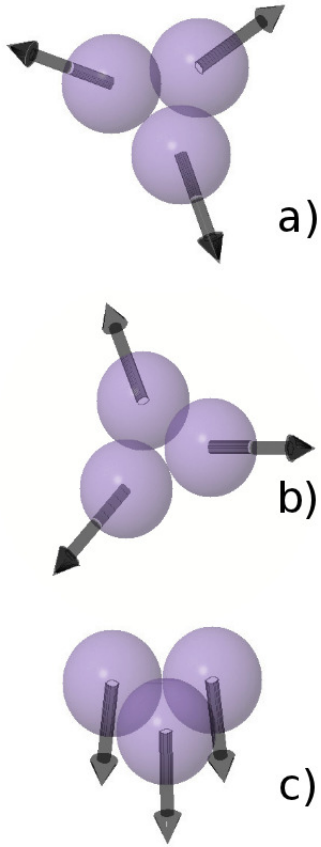
Figure 10.4. Magnetic ordering for an Mn trimer on a) Cu(111), b) Cu/Co/Cu(111) and c) Co/Cu(111) surfaces.

11.   Magnetic Structure of Mn₃Rh Alloys

The present chapter is based on the following publication:

1. S. Ganguly, M. Costa, A. B. Klautau, A. Bergman, B. Sanyal, A. Mookerjee and O. Eriksson. "Augmented space recursion formulation of the study of disordered alloys with noncollinear magnetism and spin-orbit coupling: Application to MnPt and Mn₃Rh". Phys. Rev. B **83,** 094407 (2011).

11.1   Introduction

Anti-ferromagnetic materials have attracted attention because of their potential candidature for giant magneto-resistance (GMR) devices. From a microscopic viewpoint, it is interesting to examine how lattice structure, composition, long-ranged disorder and short-range ordering determine the magnetic structure of anti-ferromagnetic alloys. In many random alloys with closed packed lattice configurations, magnetic structures can become quite complex as compared to the simple collinear anti-ferromagnetic picture usually assumed. Atomic arrangement and randomness may introduce frustration effects in such alloys. Neutron diffraction experiments have often suggested complex magnetic alignments in mostly Mn-based disordered alloys like FeMn, MnPt, Mn₃Pt and Mn₃Rh due to the presence of almost half-filled Mn 3d orbitals. Non-collinear magnetism has been studied within the density functional theory in formalisms, where the energies are functionals not of charge density but density matrices in spinor space. This has been done for ordered alloys [7; 147], amorphous materials [148; 149] and disordered alloys [150; 151] based on both the Korringa-Kohn-Rostocker (KKR) and linear muffin-tin orbitals (LMTO) methods, coupled with the single-site coherent potential approximation (CPA) to deal with disorder.

In this work we propose to generalize the augmented space recursion[152] (ASR) based on the tight-binding version of the LMTO (TB-LMTO) so that it is capable of describing non-collinear magnetism. It was shown earlier [153; 154] that the CPA appears as a specific approximation within the augmented space formalism, so that in usual cases the ASR will subsume the CPA. However, wherever effects of statistical clustering[155],
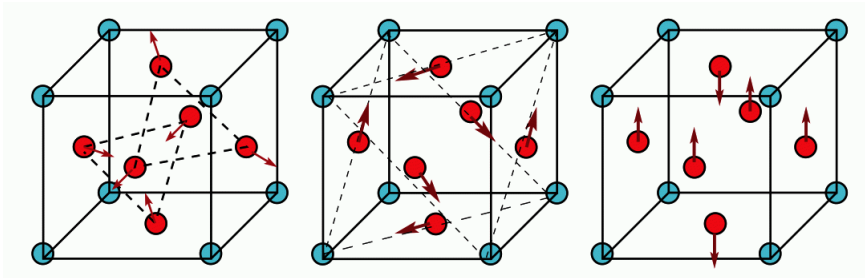
Figure 11.1. (Left) The $T1$ structure of $L12$ Mn$_3$Rh. (Center) The $T2$ structure of $L12$ Mn$_3$Rh. (Right) The collinear AFM structure of $L12$ Mn$_3$Rh. Red (dark gray) atoms are Mn and blue (light gray) atoms are Rh.

short-ranged order [156; 157], partial disorder [158] and local lattice distortions due to large size mismatch of constituent atoms in the alloy [159] become important, the ASR provides an analyticity and symmetry preserving generalization to the CPA capable of addressing these situations accurately.

11.2   Results and discussion

The magnetic structure of ordered $L12$ Mn$_3$Rh is a complex triangular ($T1$) type shown in the left panel of Fig. 11.1. The structure was shown to be a stable structure of ordered Mn$_3$Rh by Kübler *et. al.* [160]. The central panel shows another coenergetic structure $T2$ while the right panel shows a collinear antiferromagnetic like structure. Like the earlier work of Kübler *et. al.*, it was found that the $T1$ and $T2$ structures have the same DOS, total energies, and magnetic moments.

As stated in that earlier work, this is expected since our theory does not couple magnetic moments to the underlying crystal lattice. What we focus on is the relative orientation of the moments. In this sense the $T1$ and $T2$ structures are identical. A similar argument was put forward by Bertaut and Fruchart [161] based on Heisenberg models for the $T1$ and the $T2$ structures. These are identical in the absence of anisotropy. We have therefore reported only the results for the $T1$ structure in what follows. The top panel of Fig. 11.2 shows the variation of the total energy with respect to the lattice constant. The figure shows that the $T1$ structure with a = 3.62 Åis the stable ordered structure for Mn$_3$Rh. This is in consonance with the earlier work of Kübler *et. al.* The bottom panel of Fig. 11.2 shows the PDOS for Mn and Rh in the $T1/T2$ and collinear AFM structures. Both (particularly $T1$) indicate a pseudo-gap just above the Fermi level. Otherwise the two PDOS
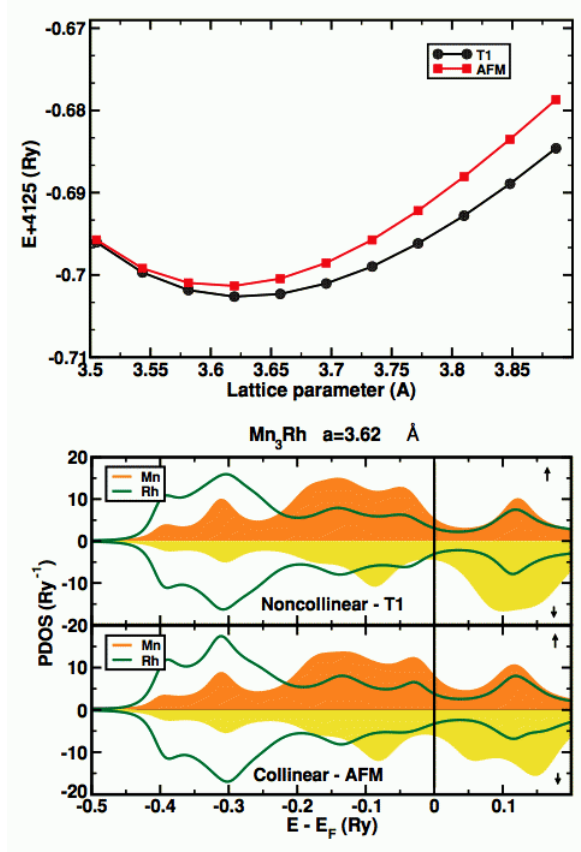
Figure 11.2. (Top) Total energy vs lattice constant for $T1$ and AFM structures for Mn_3Rh. (Bottom) PDOS for Mn and Rh for $T1/T2$ and collinear AFM Mn_3Rh.

are not very different from each other. Figure 11.3 shows the variation of magnetic moment with lattice constant for the $T1/T2$ and collinear AFM structures. The decrease of magnetic moment with lattice constant agrees with the Stoner criterion (since the closer the atoms, more is the overlap of electronic wave functions leading to a wider band and a lower DOS at the Fermi level). This indicates that these alloys exhibit itinerant magnetism. The estimate of the magnetic moment of $T1$ at equilibrium lattice constant is not far from Sakuma *et al.*, [162] but smaller than that of Kübler *et al.* Figure 11.5 shows a rather interesting fact: The exchange energy changes sign on lattice expansion, going from antiferromagnetic to a ferromagnetic transition. The $T1$ arrangement at equilibrium lattice constant (3.62 Å) sits almost at the edge of this transition. Figure 11.6 shows the PDOS for Mn and Rh in Mn_3R in the

93

Figure 11.3. Magnetic moment variation with lattice constant for $T1/T2$ and collinear AFM Mn$_3$Rh.

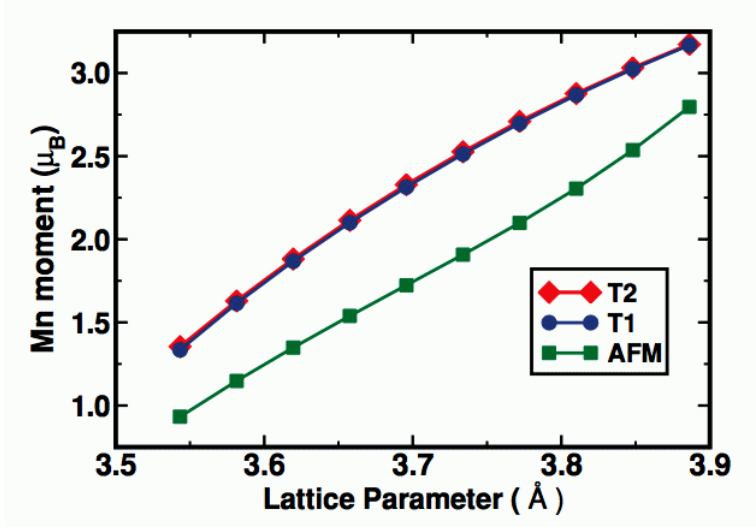| Spin Structure	M^b_{Mn} (μ_B)	M^p_{Mn} (μ_B)	M^b_{Rh} (μ_B)	M^p_{Rh} (μ_B)
1Q	2.57	2.54	0.04	-0.01
2Q	2.62	2.74	0.07	0.02
3Q	2.66	2.83	0.08	0.04

Table 11.1. *Magnetic moments obtained from TB-LMTO-CPA and TB-LMTO-ASR. ^{b} and ^{p} refer to the TB-LMTO-CPA work by Sakuma et.al. [163] and the present work respectively.*

$1Q$, $2Q$, and $3Q$ arrangements. The PDOS were calculated from the TB-LMTO-ASR using six nearest-neighbor shells in augmented space. The recursions were carried out exactly till 11 steps after which the Beer-Pettifor terminator was used to terminate the continued fraction. We show in Fig. 11.4 the convergence of the first four PDOS moments for Mn in $1Q$ Mn$_3$R. Those for $2Q$ and $3Q$ magnetic structures are qualitatively similar. In this alloy system the convergence is good after 11 recursion steps and the fluctuation in moments is of the order of 5%. A glance at Fig. 11.6 indicates that in all the three disordered alloys, there is no vestige of a pseudogap near the Fermi level. Again, random substitution of Mn with Rh disrupts the $L12$ arrangement in the ordered structures and hence disrupting the effect of the staggered field.

Table 11.1 shows the results for magnetic moments from our work and compares them with the CPA. The magnetic moments from the ASR agree well with the CPA results. Rh, unlike Pt, now carries a small

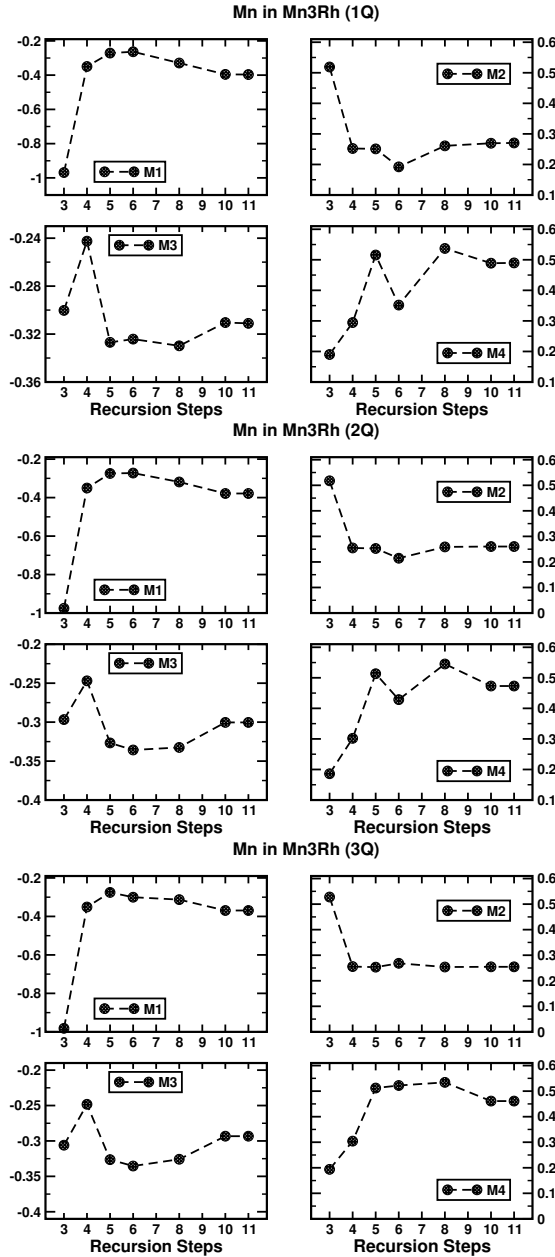*Figure 11.4.* Variation of the first four moments of the partial DOS of Mn in Mn$_3$Rh in the (top,left) 1Q (top,right) 2Q and (bottom) 3Q magnetic structures. The variation is with the number of recursion steps after which the asymptotic part of the continued fraction expression for the Green function is replaced by a Beer-Pettifor Terminator. The units for the moments M_n are $(\mathrm{Ry})^n$.
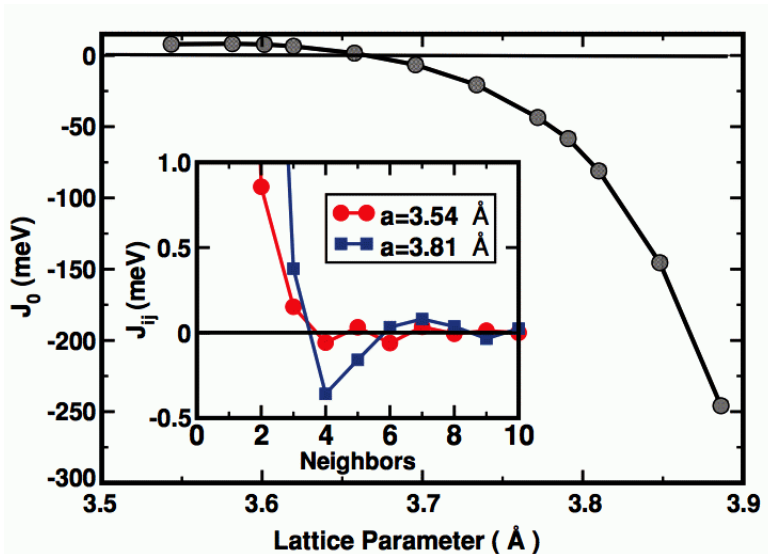
Figure 11.5. Exchange energy as a function of the lattice constant in $T1$ Mn_3R.

induced moment. However, while the CPA predicts stability in the order $3Q$, $2Q$, and $1Q$, the ASR predicts stability in the order $1Q$, $2Q$, and $3Q$. As we discussed earlier, these small energy differences between different magnetic structures are in the limits of our accuracy. Again, although we are confident that the ASR with recursion carried up to 11 steps before termination is more accurate than the single-site CPA, it would be useful to have definitive and transparent experimental results before we can make reliable statements.

11.3   Conclusion

We have set up a computational framework for the study of noncollinear magnetic phases in disordered alloys based on the marriage of three distinct techniques: the TB-LMTO, the recursion method, and the augmented space formalism. The ASR allows us to go beyond the single-site CPA and include effects of disorder in the local environment accurately. This is important, since the immediate environment of a magnetic atom in a solid has a significant impact on its local magnetic moment.

We have used our formalism to study disordered Mn_3R alloys. Our ASR results are different from the earlier CPA, specially in the energy ordering of different noncollinear states. The very small energy differences between different noncollinear phases means that our error window should be very narrow. The augmented space formalism is formally
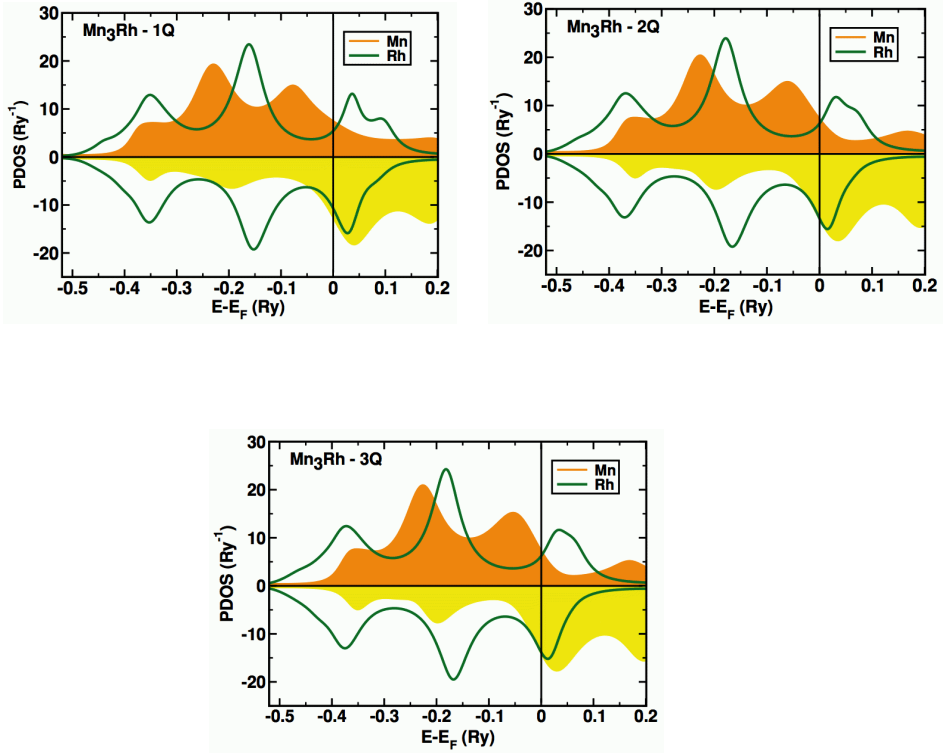
Figure 11.6. PDOS for the disordered Mn₃Rh alloy (top) 1Q structure (middle) 2Q structure and (bottom) 3Q structure.

exact; therefore, the error arises in the recursion method and the TB-LMTO. Errors in the former are controlled and can be estimated. The main source of error is in the TB-LMTO. A way out is either to replace TB-LMTO with the more accurate TB-KKR. This would lead to energy-dependent potential parameters and hence energy-dependent recursion. This was developed by Mookerjee *et. al.* [164]. Alternatively, we can use the full-potential LMTO. However, in that case, the Hamiltonian is not sparse and we have to have a relook at the errors in the recursion method.

12. *Non-Newtonian* Magnetization Dynamics, a Way to Accelerate the Switching of Logical Units

The present chapter is based on the following publication:

1. C. Etz, M. Costa, O. Eriksson and A. Bergman."*Non-Newtonian* magnetization dynamics, a way to accelerate the switching of logical units" *Submited to Nature Nanotechnology.*

12.1 Introduction

Magnetic nanoclusters deposited on surfaces present intriguing properties, especially when probing their response to an external magnetic field, by following their magnetization dynamics. We use in this work, an atomistic description of magnetization dynamics of such clusters, in which density functional theory is used to determine the parameters for the atomistic spin dynamics simulations. The magnetization dynamics of clusters supported on non-magnetic substrates is demonstrated to exhibit an unprecedented complex response when subjected to external magnetic fields. We demonstrate that, provided the energy landscape of the magnetic interactions of the cluster is sufficiently complex, the well established dependency between the applied force and the resulting speed seem not to apply. We find for these clusters that a stronger driving force in the form of an increased applied field strength, will only slow down the magnetization dynamics. This *non-Newtonian* magnetization dynamics is analysed in detail and proposed as an enabler in technological applications, since much faster switching of magnetic units can be obtained with weaker force, whether it is in form of an applied magnetic field or provided by a spin-transfer torque.

Magnetization dynamics has recently been the focus of several theoretical and experimental investigations, both for bulk-like systems [165; 166; 167; 168; 169; 170; 171; 172; 173; 174] as well as nano-sized objects [175; 176; 177; 178; 179]. From a technological point of view it is the switching of magnetic logical units that is of interest, since storing binary code information in a magnetic medium as fast and reliably as

Figure 12.1. high-symmetry anisotropy landscape

Figure 12.2. low-symmetry anisotropy landscape

top layer   bottom layer
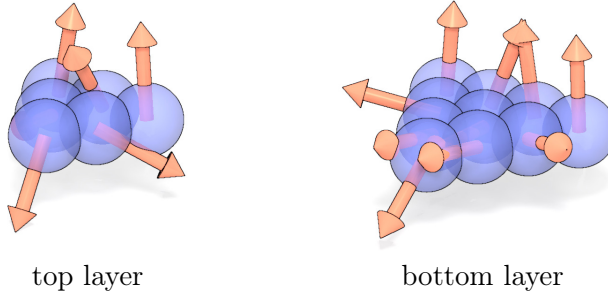
Figure 12.3. Atom-projected uniaxial anisotropy axes: Illustrative representation for the different orientations of the easy magnetization axes in the high-symmetry (top figure) and low-symmetry scenarios (bottom figure), for both top and bottom layers of the Co nanoisland.

possible stands out as being crucial. In many of the investigations published so far, fundamental new knowledge of magnetization dynamics and the magnetism of nano-sized objects have been discovered. An example of this is the possibility of magnetization reversal on femtosecond time-scales, as reported in Ref.[165], the breakdown of the macrospin model [180] as well as the possibility to achieve all-spin-based logic operations on an atomic level [181].

Typically, one observes one of the two known types of magnetization reversal: mono-domain switching or domain wall motion [182]. In both cases, the time it takes for the magnetization to reverse its direction, i.e. the switching time, is reduced when the strength of the applied field is increased. This is natural since a stronger field provides a stronger driving force to reverse the magnetization direction.

We present here magnetization dynamics in nano-sized clusters, which under special conditions deviate from well established connections between force and speed, thus seemingly disobeying classical laws of physics.

Our findings have no previous counterpart in the field of magnetism, but analogies can be drawn to so called *non-Newtonian* fluids [183] (e.g. of colloids in suspension) which demonstrate a highly non-linear response to an external stimulus.

Discrepancies between the properties of nano-sized materials compared to their bulk counterpart are known for some time. There are several reasons why nano-sized objects can behave so differently compared to the bulk materials, e.g. due to quantum confinement effects and the fact that the surface to volume ratio is very large. A good example of this are metallic nano-particles which can have a completely different optical response compared to the corresponding bulk or thin-film systems. This is also illustrated by the famous Lycurgus cup from the Roman era, where gold nano-particles included in glass create a unique luster [184].

In the present study we have investigated theoretically the magnetization dynamics of nano-islands supported on a non-magnetic substrate. We are in particular interested in the switching behavior of the magnetization direction of such nano-particles, under the influence of an external magnetic field. The magnetic islands are composed of 16 up to 111 Co atoms deposited on a Cu substrate. We have investigated the switching behavior of these islands in the presence of a static external magnetic field. The Cu substrate is a very suitable choice for the study of magnetic nanostructures supported on its surface, since it is rather *inert* to polarization effects due to its completely filled d-shell and its weak spin-orbit coupling. Hence, in a spin-Hamiltonian only the Co nano-particle has to be considered, albeit with appropriate parameters that come from a first principles theory which includes also effects of the substrate.

12.2 Theory

The systems we study consist of two atomic-layers high Co islands (in fcc-stacking) deposited on a Cu(111) substrate. The nanostructures are triangularly-shaped. The fact that the system is finite and has a low symmetry is reflected in the electronic structure and magnetic properties, fact that has already been proven in a previous work [185]. As a consequence, the spin and orbital moments as well as the exchange interactions and the magnetocrystalline anisotropy have a non-uniform spatial distribution within the nanostructures. Since it is well known that the magnetic properties depend strongly on the individual atoms' local environment [186], we take into account the edge effects, which have an increasing weight the smaller the system is.

As a first step, we performed a thorough *ab initio* investigation of the islands' electronic and magnetic structure, using a Green's function formalism within relativistic density functional theory (DFT), as im-

plemented in SKKR (screened Korringa-Kohn-Rostocker) [26] and RS-LMTO-ASA (real-space linear muffin-tin orbitals within atomic sphere approximation) [23]. After having obtained the *ab initio* site-resolved quantities, such as magnetic moments, interatomic exchange parameters and magnetic anisotropies, we continue with the investigation of the spin dynamics in these nanostructures by means of the atomistic spin dynamics package UppASD [187]. As discussed above we do not consider the Cu substrate in the spin dynamics simulations, since the spin and orbital polarization is negligibly small (of the order of 0.005 μ_B/atom). Hence the tiny induced moments in the Cu substrate and the very weak exchange coupling with the Co atoms do not influence in any way the dynamics of the Co system.

Using all site-resolved quantities determined from first-principles as initial parameters, we investigate the magnetization dynamics of the system under the influence of external magnetic fields. The time evolution of the magnetization, as described by the Landau-Lifshitz-Gilbert (LLG) equation:

$$\frac{\partial \mathbf{m}}{\partial t} = -\gamma \mathbf{m} \times \mathbf{B} + \frac{\alpha}{m} \mathbf{m} \times \frac{\partial \mathbf{m}}{\partial t} \tag{12.1}$$

where the first term is the so called precession term and the second is the damping term. The damping torque is perpendicular to the precession torque. Since the damping parameter α entering the LLG equation was not obtained from first-principles, its value has been varied within reasonable limits without noticeable effects on the behavior of the switching process. The presented results were obtained for a damping α=0.1.

12.3 Results and Discussion

As will be shown later on, the most important quantities that determine the switching behavior are in fact the atom-projected magnetocrystalline anisotropy energies (MAE). From the *ab initio* calculations results we find that the direction of the easy axes and the anisotropy strengths depend on the atoms positions in the cluster. It is possible to map the *ab initio* calculated anisotropy energies to an effective Hamiltonian where each atom has a unique uniaxial anisotropy. Combined, the local uniaxial anisotropies yield a complex anisotropy energy landscape of the cluster, which has a net out-of-plane easy axis. A depiction for the directions of the site-projected easy magnetization axes for the low-symmetry case can be seen in Fig. 12.3. In addition to the direct fit from the *ab-inito* results (Fig. 12.1), where each easy axis direction points toward the corresponding global minima of the anisotropy energy for each specific atom, we have also considered a slightly altered anisotropy energy configuration (Fig. 12.2). In the second scenario (Fig. 12.2), we have taken for the
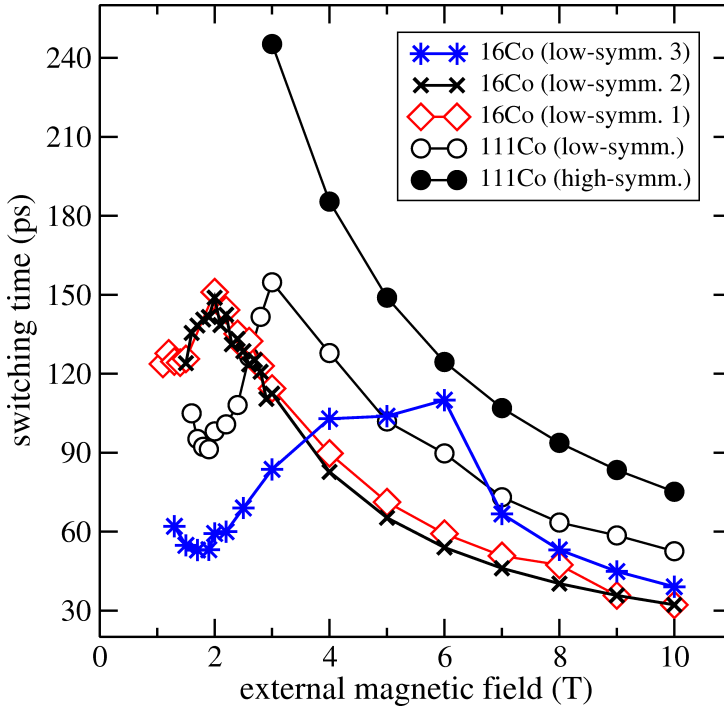
Figure 12.4. Switching time dependence on the strength of the external magnetic fields for the low-symmetry anisotropy landscape of Fig. 12.2 (empty circles), illustrating a non-monotonous relationship between switching time and field strength. Same behaviour for two test cases with random directions of the easy axes (empty triangles). Filled symbols represent the monotonous dependence of the switching times w.r.t field strengths, for an anisotropy landscape that reflects a higher symmetry of the island (Fig. 12.1).

atoms situated on one of the edges, the easy magnetization axes pointing along local minima directions in the three-dimensional (3D) anisotropy energy landscape. In this case the symmetry is lower than what was obtained from the ab-inito calculations. This latter configuration that will be called the low-symmetry case in the discussion below, can be seen as an effort to make a realistic emulation of symmetry-breaking effects that might occur for these supported nano-islands, i.e. geometrical distortions or chemical intermixing. Before performing the magnetization dynamics simulations, the equilibrium magnetic structure is obtained by allowing the magnetic moments to relax in this anisotropy landscape. This results in an essentially collinear magnetic ordering pointing out of plane. For the low-symmetry case a small deviation from the surface normal, up to 6° in terms of the polar angle θ was found.

We investigate next the reversal mechanism of the magnetization, under the influence of an applied magnetic field, in these magnetic nanoislands. In the following we will focus our attention only on small islands (16 and 111 Co atoms) since the behavior they exhibit is analogous to all sufficiently small island sizes, i.e. where edge effects are large and the size of the cluster does not allow domain formation. We study the switching dynamics of the magnetic system under the driving force of external magnetic fields $\vec{B}_{ext}$ of different intensities, pointing along the surface normal and having an opposite direction to the magnetic moments' orientation, $\vec{B}_{ext} = \begin{pmatrix} 0, & 0, & -B^z \end{pmatrix}$.

During the application of the magnetic field, we follow the time evolution of the average magnetization. We let the system evolve for 180 ps and we probe the changes in the magnetization's orientation each 100 attoseconds. Following the change in the orientation of the average magnetization's z-component we determine the switching times (t_{sw}) corresponding to different field intensities (the switching is achieved when the z-component of the average magnetization is flipped by 180° with respect to its initial orientation). Despite the fact that the values of the magnetic moments, anisotropies and exchange interactions are not homogeneously distributed over the island, a coherent magnetization reversal takes place for all systems studied. The nanoislands behave and switch essentially as a mono-domain as long as the temperature is low enough. Even though the magnitude of the spin moments differ within the island, since they remain parallel during the whole dynamical process, one may regard them as a collection and, for simplicity, we refer to all these collinear spins as *macro-spin* in the following.

First we perform the switching simulations for the high-symmetry case (shown in Fig. 12.1) and find that as the applied field increases, the observed switching times decrease in a monotonic fashion for these clusters (shown as filled squares in Fig. 12.2). This is an expected result [182], as the driving force for the switching is stronger when the field strength increases.

Next we consider the clusters where the symmetry of the magnetic anisotropy landscape has been reduced (Fig. 12.2). For the 16 atoms island, the switching occurs only for a field larger than ~ 1.1 T and it takes roughly 120 ps after its application, before the magnetization is reversed (Fig. 12.2). This is considerably faster compared to the switching time of clusters with a symmetric magnetic anisotropy landscape (Fig. 12.2). When increasing the strength of the external field, the torque driving the switching increases, which is expected to lead to shorter switching times. In a certain range, we find however that the switching times actually become longer the stronger the magnetic field is. For example, for a field of 2 T, the switching time is roughly 30 ps longer than for $B_{ext} = 1.5$ T.
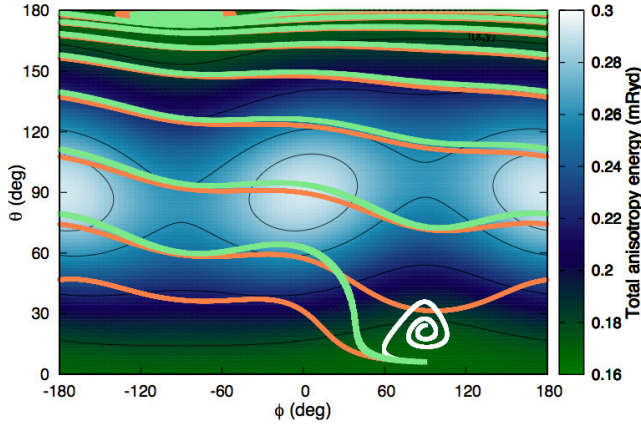
Figure 12.5. Trajectories of the 16 Co atoms *macro-spin*, in the magnetocrystalline anisotropy energy landscape, under the influence of a 1 T (yellow line), 1.5 T (black line) and 2 T (red line) external field, respectively. The color scale indicates the strength of the anisotropy energy (mRyd), showing that $\theta=90°$ represents the hard magnetization plane (i.e. the island's plane).

When increasing the applied field further (above 2 T), the switching times get shorter the stronger the field is. We probed the magnetization dynamics up to very strong magnetic fields (up to B_{ext}=10 T, Fig. 12.2). The non-monotonous dependence of the switching times on the external magnetic fields is quite pronounced for $B_{ext} \leqslant 2$ T for 16 Co atoms and for $B_{ext} \leqslant 3$ T for 111 Co atoms (see Fig. 12.2). Comparing the switching times of islands with high-symmetric energy landscape with those of low-symmetric landscapes (Fig. 12.2) one notices that the latter reverse their magnetization direction faster. For low external fields, the difference is very large.

The fact that we observe an increase in switching times with increasing field strength, i.e. a process analogous to *non-Newtonian* dynamics of colloids in suspension, only when the symmetry of the magnetic anisotropy energy is low, gives strong evidence that it is in fact the complex anisotropy landscape that causes this non-monotonous behavior (see Fig. 12.2). In order to elucidate this phenomenon, we now proceed with a detailed analysis of the magnetization reversal process for clusters with a low-symmetry magnetic anisotropy. Since there is a coherent magnetization reversal present, all the spins in the nano-isalnd remain parallel (within very small deviations) during the switching process. In Fig. 12.5, the spin trajectories for all the atoms within an island would overlap, but for clarity we chose to represent only one spin-trajectory for each case. We start by investigating the change in the trajectory of the *macro-spin*, projected onto the anisotropy energy landscape (Fig. 12.5). We plot (in a

map view) in Fig. 12.5, the three dimensional (3D) magnetic anisotropy landscape in polar coordinates, together with the paths taken by the magnetization vector for different field strengths. Note that Fig. 12.5 shows the 3D energy landscape in a top-view projection, as a function of polar angles, θ and ϕ, and that higher magnetic anisotropy regions are shown in yellow/bright color and lower anisotropy energy regions are shown in purple/dark color. The changes in the polar angle θ represent a variation in the out-of-plane component of the magnetization, while changes in ϕ show variations in the in-plane component.

The energy landscape shows a maximum in the anisotropy energy at coordinates $\theta=90°$ and $\phi=0°$ and $180°$, which represents the hard-magnetization region. The fine contour lines mark equi-energy lines in the anisotropy energy landscape. Fig. 12.5 clearly shows that the energy landscape is not independent of the azimuthal angle ϕ which would be the case for a single uniaxial anisotropy of the nano-island. The largest energy barrier to overcome is in the surface plane, which is the hard-magnetization plane. Fig. 12.5 shows an important result, namely the marked difference in the paths that the nanoisland's *macro-spin* takes, under the influence of different strengths of the applied external magnetic field (illustrated for three field strengths: 1.0 T yellow line, 1.5 T black line, 2 T red line).

In Fig. 12.5, it can be seen that the reason for the faster switching in the 1.5 T field is that this trajectory "skips" a precession and approaches much faster the hard magnetization plane. Translated in terms of the 3D anisotropy energy profile, this means that the resulting effective field acting on the *macro-spin* moves it to a region of the MAE landscape where the energy has its maximum value. Under the stronger field (e.g. 2 T), on the other hand, the spins follow the expected precessional movement around the resulting effective field's axis.

The question why the *macro-spin* approaches the magnetically hard plane of the energy landscape quicker for the 1.5 T case compared to the 2 T field, can be explained from the trajectories shown in Fig. 12.5. For comparison, we start by describing the well-known case of coherent switching of a *macro-spin* in a single uniaxial anisotropy [188] environment, under the influence of an antiparallel external field. In that case, the resulting effective field acting on the *macro-spin*, will always have a constant direction along the easy magnetization axis. Thus, the switching will be determined solely by the damping torque from the effective field and the switching time will decrease with increasing field strengths. If the external field is weak, the torques generated by it will be counter-balanced by torques induced by the anisotropy field and the magnetization reversal will not occur. In this case, the equilibrium direction of the *macro-spin* will still be along the easy axis.

In our system with a low symmetry of the MAE landscape (Fig. 12.2), the picture is more complicated. The applied field will still give rise to precessional and damping torques, but the contribution from the anisotropy field is significantly more complex. Due to the competition between the different site-projected magnetic anisotropies in the cluster, the anisotropy fields will cause precessional and damping torques albeit not in the same directions as the torques derived exclusively from the applied field. This can be seen very clearly in the trajectory for the B_{ext}=1.0 T (yellow/light-coloured line in Fig. 12.5) where the *macro-spin* makes only a small curled movement to a new static equilibrium position, without a magnetization reversal. For an intermediate field, such as B_{ext}=1.5 T, there is a delicate balance between the different torques. The precessional torque from the anisotropy field becomes parallel to the damping torque of the applied field. This results in the sharp turn of the trajectory for this *macro-spin* towards the magnetically hard region of the anisotropy landscape. If the applied field is increased even more (see B_{ext}=2.0 T in Fig. 12.5), the precessional torque from the applied field dominates over all other torques. The *macro-spin* will, in this case, essentially be driven by the torque originating from the applied field, which dictates a precession movement. Instead of being rapidly forced by the *anisotropy torque* towards the magnetically hard region, the *macro-spin* makes an additional revolution around the z-axis.

Even inside the high anisotropy energy region (i.e. for values of θ close to 90°), the ratio between the applied field and the anisotropy field differs between the B_{ext}=1.5 T and 2.0 T cases, even though the difference is not as drastic as in the early stage of the switching process. Both trajectories follow here roughly parallel paths (see Fig. 12.5) but we find that the trajectory under the stronger field is delayed further in this region due to the fact that it actually crosses over the highest peak of the anisotropy energy landscape. On the other hand, the torque exerted by the lower field on the moments is not strong enough to overcome the highest anisotropy barrier. Once the moments have passed the magnetically hard region, they proceed with their precessional and damped motion towards the z-direction without significant differences between the two paths.

The shorter switching time with a weaker field is found for islands of different size (the largest island we took into consideration for our study contains 111 Co atoms) and for several choices of the anisotropy energy landscape. Hence we investigated also other cases besides the one depicted in Fig. 12.2 and obtained similar results (these are shown in Fig 12.2). All simulations show an increase of the switching time with increasing field up to a certain field strength, after which the switching time decreases with increasing fields. The only pre-requisite for this to

happen, is the presence of a sufficiently low-symmetry distribution of the anisotropy over the island.

So far, we have not discussed the effect of the exchange interactions on the complex magnetization dynamics shown in Fig. 12.2. We note however, that the exchange interactions obtained from our first principles calculations are strong enough to maintain a collinear arrangement, forming a *macro-spin*, during the studied switching scenarios and thus their relative strengths are not as important for the switching as the individual anisotropy energies. However, the complex connection between switching time and strength of the external magnetic field is present even when reducing the exchange interaction strength by a factor of 100 (data not shown here). Although, in this case, the island does not switch as a *macro-spin* anymore, but exhibits in fact an even more complicated dynamical response to the applied field. Finally, we note that at sufficiently high temperature both the *macro-spin* picture and the reported switching behavior breaks down into a more stochastic behavior (data not shown), but the effect reported here is stable up to 1 K. On general grounds larger magnetic units, with a similar energy landscape as the cluster in Fig.1b, are expected to exhibit a *non-Newtonian* magnetisation dynamics up to even higher temperatures.

12.4 Conclusion

The dynamics of the magnetic clusters with a low symmetric energy landscape have, for a certain range of parameters, a dynamical response that suggests that well established relations between speed and force, which are common knowledge under the laws of physics, seem not to apply. Stronger driving forces will in certain cases only slow down the dynamics. The possibility to use this fact in technological applications is obvious, since faster switching of magnetic units can be obtained with weaker applied fields, whether it is a magnetic field or a torque provided by a spin-transfer torque.

We have illustrated a highly complex (and fast) switching behavior for several selected cases of supported nano-clusters and we argue that this behavior should be present in a wide range of systems, even large systems containing thousands of atoms. Since the driving force is the individual atom's contribution to the total magnetic anisotropy landscape, which is known to be very sensitive to the local environment [186], this effect is likely to be enhanced even further by tailoring specific clusters with respect to both geometry and chemical alloying. This can be achieved, for example, by considering clusters of mixed chemical composition, where local anisotropy axes are expected to cause an even more asymmetric total energy landscape of the magnetic anisotropy. An alternative would

be to grow clusters on random alloy substrates, e.g. $Cu_xAg_{(1-x)}$. It is known that ligand states from nearest neighboring atoms influence the local anisotropy [189], hence a Co atom neighboring a Ag atom will have different easy axis direction than a Co neighboring a Cu atom. Finally, we point out that the *non-Newtonian* magnetization dynamics can also be realized by using a spin-transfer torque as the driving force of the switching.

13. Outlook and Future Perspectives

The DFT framework has proven to be accurate and flexible to be applied in several different systems. Several improvements on DFT has been proposed, including LDA+U, the GW method, hybrid functionals and LDA+DMFT. We have investigated the magnetic anisotropy energy (MAE) of the compound Fe2P. It has been proposed that alloying these material with Si could give the possibility to stabilize the magnetic order and the MAE up to room temperature. The next step would be to calculate the MAE for these alloys, using a method like the augmented recursion space (ASR) or the coherent potential approximation (CPA) to get a proper treatment of the chemical disorder. It would also be interesting to see an experimental confirmation of our findings. The magnetic anisotropy is very difficulty property to calculate. In this work we obtained a good agreement with the experimental value. Nevertheless this is not the case in general. When the MAE is very small, as is the case with Ni, then not even the correct easy axis can be obtained. Also for compounds with rare-earth f-shells the agreement is not good in general. The cause of this failure is that LDA does not treat localized systems properly. A proper treatment of the f-shells can be achieved by using LDA+DMFT, nevertheless calculating the MAE in this scheme is both computationally and conceptual challenging, since the double counting term in the DMFT part is poses a problem. So work on this direction would be very interesting. Also we should continue the implementation of the DMFT scheme in the RS-LMTO-ASA code, where we need to solve some problems regarding the continued fraction terminator to obtain a correct DOS. With this implementation one could calculate magnetic exchange parameters for systems showing strong correlations. With the exchange parameters one can estimate the Curie temperature. The investigation of the spin dynamics for Co islands should be extended to other transition metals with complex compositions. I think we are in a good position to continue studying the effects of strong correlation using the LDA+DMFT implementation in the FP-LMTO.

14. Svensk Sammanfattning

Vetenskapsmän söker efter teorier som kan förklara och förutsäga hur naturens lagar beter sig. En av de mest framgångsrika teorier som mänskligheten lyckats frambringa är Kvantmekaniken, som startade med Plancks energikvantisering, som infördes för att lösa den så kallade ultravioletta katastrofen för svartkroppsstrålning. Kärnan av kvantmekaniken beskrivs av Schrödingerekvationen som föreslogs 1926 och som beskriver hur vågfunktioner beter sig i tid och rum. Eftersom kvantmekaniken framgångsrikt kunde förklara flera tidigare oförklarliga mikroskopiska fenomen så blev den accepterad av det vetenskapliga samhället trots sin icke-deterministiska natur. Trots att teorin tillämpades framgångsrikt på flera system var den också väldigt komplex så att det största system som kunde lösas exakt var väteatomen. På grund av denna komplexitet begränsades teorin till små system, även om många försök till att lösa de komplicerade ekvationerna har gjorts genom historien. Med upptäckten av transistorn, som gjordes av Bardeen och hans medarbetare utifrån en kvantmekanisk formalism så kom också utvecklingen av moderna datorer igång. Datorernas ständigt ökande beräkningskraft möjligjorde att större problem kunde angripas. Men med de förenklingar av teorin som på den tiden behövdes för att kunna begränsa komplexiteten på ekvationerna så höll bara teorin för kvalitativa beskrivningar. En vågfunktion har 3N frihetsgrader och dessa frihetsgrader är dessutom kopplade till varandra vilket ger vågfunktionen sin mångkropparsnatur. Knappt 40 år efter Schrödingers prestation så kunde Hohenberg och Kohn presentera två teorem som satte grunden för den så kallade täthetsfunktionalteorin, förkortat DFT. DFT formulerar om problemet från Schrödingers ekvation från att söka efter vågfunktionen för ett givet system till att ta fram tätheten rho, vilket är ett mycket enklare problem då antalet frihetsgrader minskas till 3. Deras teorem visade rigoröst på en formell ekvivalens mellan de två olika tillvägagångssätten. även om DFT var formellt exakt så var teorin inte speciellt tillämpbar men 1965 föreslog Kohn och Sham ett mer praktiskt tillvägagångssätt och lade fram de så kallade Kohn-Sham ekvationerna som är giltiga för vilken kvantmekanisk entitet som helst, som elektroner, neutroner osv. Egenskaperna hos ett material bestäms främst av dess elektroniska struktur, därför kommer uttrycket täthet framöver hänvisa till elektrontäthet. En av de viktigaste egenskaperna hos elektronerna i ett material är att de är korrelerade, vilket betyder att rörelsen för varje enskild elektron påverkar, och

110

påverkas av, alla andra elektroner. Det är viktigt att poängtera att DFT är en enpartikelteori där mångkropparseffekter endast kommer in som en medelfältseffekt i teorin genom Exc. Denna egenskap återspeglas i formalismen för DFT genom en funktional innehållande energin för elektronernas korrelation kombinerat med en energi för elektronernas utbytesväxelverkan som är den energi som krävs för byta plats på två elektroner. Denna utbytes- och korrelationsfunktional är orsaken till den största approximationen inom DFT. Om funktionalen vore exakt känd skulle även teorin vara exakt. Det finns två dominerande approximationen till denna funktional, dels lokala täthetsapproximationen (LDA) och den generaliserade gradientapproximationen (GGA). Trots sin framgång så har DFT inte förmåga att behandla alla system. Ett av de mest framstående problemen är att kunna beskriva starkt korrelerade system. Stark korrelation är en effekt av rumslig lokalisering av elektrontillstånd d.v.s. elektronerna är begränsade till vissa regioner runt atomernas kärnor, ett fenomen som oftast uppkommer hos elektroner med 3d och f tillstånd. Orenheter bestående av övergångsmetaller begravda i en alkalimetall uppvisar sådan stark korrelation, t.ex. hos Fe orenheter i Cs. Gitterparametern för Cs är ca. två gånger större än för Fe. När en Fe atom sitter som en orenhet i Cs så blir överlappet mellan vågfunktionerna för elektronerna hos Fe atomen och angränsande Ce atomerna väldigt litet, d.v.s. sannolikheten att en elektron på Fe atomen ska hoppa till en Cs atom är väldigt låg. Det leder till att elektronerna blir väldigt lokaliserade på Fe atomen. För detta system så misslyckas DFT-LDA med att beskriva de experimentellt uppmätta spektrala egenskaperna. Vi har dock visat att man kan introducera korrektioner till teorin för att förbättra överensstämmelsen med experimenten. Det gjordes genom att använda den så kallade dynamiska medelfältsteorin (DMFT). För att kunna studera kemiskt oordnade system med komplex magnetisk ordning har vi vidareutvecklat en avancerad formalism, augmenterad rymdrekursion (ASR), som kan studera just kemiskt oordning på ett kraftfullt sätt, så att godtyckliga icke-kolinjära magnetiska ordningar kan behandlas inom detta ramverk. Metoden har sedan använts för att studera magnetismens inverkan på stabiliteten hos oordnade och ordnade Mn-baserade legeringar, MnPt och Mn3Rh. Ett ämne som studerats flitigt är permanentmagneter fria från sällsynta jordartsmetaller. I industrin finns det gott om användningsområden för permanentmagneter, från vindkraftturbiner till hårddiskar, och de flesta av dessa permanentmagneter innehåller i dag sällsynta jordartsmetaller. De senaste åren har dock priset på de metaller som behövs i magneterna skjutit i höjden. Det har dels berott på den ökade efterfrågan men beror även på att Kina har ett monopol på tillgångarna av dessa sällsynta jordartsmetaller. Mycket uppmärksamhet har inom detta område ägnats åt fosfider. En av nyckelegenskaperna hos permanentmagneter är den starka magne-

tokristallina anisotropin, vilket ger en föredragen riktning hos de magnetiska momenten i ett material jämfört med materialets kristallstruktur. Vi har undersökt orsaken till den starka magnetokristallina anisotropienergin (MAE) hos dijärnfosfid Fe2P. Fe2P har en experimentellt upmätt MAE på 500 mueV per formelenhet. Den beräknade MAEn är 664 mueV per formelenhet vilket avviker circa 30% från det uppmätta värdet. En sådan avvikelse är inte oväntad då MAEn är en väldigt subtil och svårberäknad effekt. Vi har också visat att det går att öka MAEn med upp till 15% genom att sträcka ut materialet. Dessutom har vi föreslagit att genom att legera Fe2P med 10% Si på fosforpositionen i materialet så kan det kanske bli möjligt att realisera att materialets magnetiska tillstånd kan överleva i rumstemperatur. Vi har även studerat andra, besläktade Fe-P system där vi kunnat förklara den ovanliga ikosahedriska metalfosfor koordineringen i ett nytt mineral melliniite, som påträffats i en meteorit från nordvästafrika, 1054 Acapulcoite. Mineralet har en ideal kemisk sammansättning (Ni,Fe)4P med uppskattningsvis 58% Ni och 42% Fe på metallpositionen. Det oväntade med detta mineral var att fosforatomerna uppvisade en tolvfaldig koordinering, hittills har maximalt tiofaldig koordinering hos fosfor observerats, i Co2P. Genom att använda den så kallade Koherenta potentialapproximationen (CPA) och den balanserade kristallorbitalöverlappspopulationen (BCOOP) kunde vi visa att bindningen mellan Fe och P, i kombination med temperatureffekter och konfigurationell entropi, stabiliserar materialet vid temperaturer över 540 K. Den försvagade Ni-P bindningen bidrar däremot till den observerade tolvfaldiga koordinationen av fosforatomerna. Vi har vidare studerat system bestående av kluster på magnetiska metallytor. De senaste åren har sådana kluster pekats ut som intressanta dels för att de ofta har magnetiska egenskaper som inte kan återskapas i större bulkmaterial och dels för att de har potential för att användas som extremt små informationsbärare i framtida magnetisk datalagringstekniker så som morgondagens hårddiskar. Främst har de magnetiska växelverkningrna mellan de magnetiska momenten i dessa kluster och i de underliggande ytlagren studerats. Här har vi undersökt små Co kluster på kopparbaserade ytor i form av Co/Cu(111), Cu/Co/Cu(111) och Cu(111). Här användes en icke-kollinjär DFT formalism och vi visade att den förväntade magnetiska frustrationen hos triangulära Mn kluster kan undertryckas genom växelverkningar med Co atomer på Co/Cu(111)-ytan. Dessa resultat öppnar up för möjligheten att kunna skräddarsy de magnetiska egenskaperna för sådana kluster. I ett närliggande arbete har vi påvisat ett oväntat beteende för spinndynamiken hos Co kluster liggandes på en Cu(111) yta, nämligen att för vissa intervall av styrkan på ett pålagt magnetisk fält kan magnetiseringen hos klustret ändra riktning snabbare om det magnetiska fältet minskar i intensitet. Det strider helt mot den gängse uppfattningen att starkare drivkraft ger större respons.

Vi benämner denna magnetiseringsdynamik för icke-Newtonsk då fenomentet påminner om hur icke-Newtonska vätskor som blir trögare vid högre tryck beter sig.

15. Resumo em Português

Em geral cientistas procuram por teorias que possam explicar e prever a natureza. A mecânica quântica é uma das teorias mais bem sucedidas já produzidas. Planck introduziu a quantização da energia para resolver o problema da catástrofe do ultravioleta, e 1926 Schrödinger porpôs a sua famosa equação. Devido a sua natureza contra intuitiva a mecânica quântica sofreu de uma certa resistência da comunidade científica. Porém devido a o sucesso da teoria em explicar a estabilidade atômica e outros fenômenos esta acabou sendo aceita. Um dos pontos que encontrou mais resitência é a sua interpretação probabilística. Apesar do sucesso, as equações envolvidas são de uma enorme complexidade, somente sendo possível encontrar soluções pra problemas simples, como o átomo de hidrogêneo. Com o advento dos computadores modernos, soluções numéricas para sistemas grandes começaram a ser possíveis. Porém ainda assim obter uma função de onda $\Psi(\vec{r}_1, ..., \vec{r}_N)$, com $3N$ graus de liberdade é uma tarefa impossível. A maior dificuldade na solução da equação de Schrödinger é devido ao efeito de muitos corpos. Em 1964 Hohenberg e Kohn propuseram dois teoremas que fundamentaram a teoria do funcional da densidade (DFT em inglês), esta teoria que é utilizada nesta tese.

Na teoria do funcional da densidade ao invés de calcularmos a função de onda, o observável fundamental envolvido é a densidade $\rho(\vec{r})$, que é uma função de 3 variáveis, muito mais simples que a função de onda. Estes teoremas mostram a equivalência entre os dois métodos, e em 1965 Kohn e Sham propuseram as chamadas equações Kohn-Sham e o funcional de correlação e troca ($E_{XC}[\vec{r}]$). Este último contém todas as informações sobre os efeitos de muitos corpos, com o conhecimento da forma exata do funcional de correlação e troca a DFT seria uma teoria exata. Naturalmente isto não é possível e aproximações são inevitáveis. A primeira aproximação proposta, foi a cahmada aproximação da densidade local (LDA em inglês). A LDA introduz os efeitos de correlação e troca através do mapeamento da correlação e troca de um gás de eletrons homogêneo. Apesar do sucesso obtido pela LDA, esta aproximação falha para alguns sistemas, chamados de fortemente correlacionados. Em geral estes sistemas estão relacionados a funções de onda espacialmente localizadas, estados $3d$ e f. Neste trabalho investigamos o caráter fortemente correlacionado de impurezas de Fe em Cs. O Cs tem um parâmetro de rede 2 vezes maior que o do Fe, com isso a sobreposição das funções

de onda do Fe e Cs é pequena. E isto leva a a localização espacial dos eletrons da impureza de Fe. A LDA é incapaz de reproduzir as propriedades espectrais do Fe. Neste trabalho utilizamos a chamada teoria dinâmica de campo médio (DMFT em inglês) para introduzir correções a LDA.

Investigamos também a possibilidade de se obter um magneto permanente duro não baseado em terras raras. Inúmeras aplicações industriais utilizam magnetos permanentes duros de tubinas eólicas a discos rígidos. E muitos destes dispositivos utilizam magnetos baseados em terras raras como Nd e Sm. Porém nos últimos anos o preço destas commodities tem aumentado vertiginosamente. Este aumento é devio ao crescimento da demanda e, em maior parte, devido ao "monopólio" Chines na mineração destes materiais. Atualmente a China produz 97 % das terras raras consumidas no mundo. Existem minas de terras raras em diversas partes do mundo, porém no início dos anos 2000 estas foram fechadas devido aos baixos preços e a pressões dos ambientalistas. O que é um tanto quanto contraditório, tendo em vista que a maioria das tecnologias para a geração de energia limpa se utiliza de terras raras. Uma das características necessárias para se obter um magneto permanente duro é que este possua um alto valor da energia de anisotropia magnética (MAE em inglês). A MAE do composto Fe_2P determinada experimentalmente é de 500 $\mu eV/f.u.$, o que é muito incomum para materias a base de Fe. Em nosso cálculo obtemos um valor de 664 $\mu eV/f.u.$, uma diferença de 32 %. Um acordo aceitável entre teoria e experimento, tendo em vista a delicada natureza da MAE. Mostramos também como é possível aumentar a MAE aplicando tensão ao material. Obtemos um aumento de até 15 % no valor da MAE.

Em um tópico relacionado, investigamos um meteorito melliniite, que foi encontrado no norte da Africa. Neste meteorito foi encontrado átomos de fósforo coordenados por 12 átomos metálicos (Fe,Ni), na forma de um icosaedro. Antes desta descoberta a máxima coordenação encontrada para o P era de 10 átomos em um composto Co_2P. A composição do melliniite é (Ni,Fe)$_4$P, com 58% de Ni e 42% de Fe. Calculamos a energia de formação deste composto, utilizando a aproximação do potencial coerente (CPA em inglês) para tratar a desordem. Fizemos uma analise das ligações metal-fósforo através do método *balanced crystal overlap population* (BCOOP). Mostramos que o composto é estável para temperaturas acima de 540K.

Investigamos *clusters* (aglomerados) adsorvidos em superfícies metálicas e magnéticas. Nos últimos anos estas estruturas tem sido alvo de intensas pesquisas. Uma das possíveis aplicações é sua utilização como base da próxima geração de discos rígidos. Mostramos que a competição entre exchange inter-atômico entre átomos de Mn no *clusters* e os átomos da superfície leva a supressão do fenômeno chamado frustração mag-

nética. Em um trabalho relacionado, revelamos um comportamento inesperado da dinâmica de spin de *clusters* de Co sobre uma superfície de Cu(111). Para certas valores do campo magnético aplicado, a magnetização do *clusters* muda de direção mais rapidamente se o campo magnético diminui em intensidade. Denominado um comportamento Não-Newtoniano.

Para estudarmos sistemas com desordem e um perfil magnético complexo, desenvolvemos um avançado formalismo, chamado *augmented space recursion* (ASR). Este método foi aplica no estudo de ligas de Mn como MnPt e Mn_3Rh.

16. Acknowledgement

This work is a Brazilian-Swedish collaboration. It is 4-year-work and so many people have participated in this process that to a proper acknowledgement it would take a few pages, but i will try my best in a few lines.

I would like to thank my supervisors. From the Brazilian side, Pedro for introducing me to the field and being supportive during this period. Anders for helping me with every single detail during my time in Sweden from physics to renting. Thank you very much for all your support. Olle, thank you for giving me the opportunity to work on your group and to learn so much from you. Angela, thank you very much for everything and for making possible my coming to Sweden, send my regards also to Crispino and Bella. Thank you Biplab for helping with the projects and discussions.

I Also have to thanks people from our division at UFF: Bechara, Toninho, Andreia, Daniel, Dionizio, Marciano, Alvaro, Filipe e Carlos. In Sweden I worked with so many people, but I have to give an special thank to Igor, Patrik and Oscar for all the help with the DMFT, the codes and for discussions in general. I would like to show my appreciation for people from the group specially Attila (thanks for the help with the thesis), Misha, Baotian, Corina, Krisztina. Sorry for not citing everyone.

My officemates from the Brazilian side Flávio and André. Despite of your terrible taste for football team it was a pleasure sharing the office with you guys. In the Swedish side Martin, Mikael, Peter and Iulia thank you for everything.

Now in portuguese....

Eu gostaria de agradecer todo o suporte dado pela minha família. Meus pais Jorge e Conceição apesar da distância estivemos sempre juntos. Mario e Julia os únicos que vieram nos visitar. Meus sogros Luis e Teresa que devem estar chegando em alguns dias. Felipe, Fernanda e Rafael, que chegou a pouco tempo mas que já nos alegra imensamente. Também a meus amigos que ficaram no Brasil na torcida especialmente Jonas, Filipi e Telma.

Um agradecimento especial ao Moyses, uma pessoa extremamente generosa e que me ajudou muito desde a minha chegada, me apresentou toda a "gangue" de brasileiros em Uppsala. Muito obrigado a todos, nossos encontros foram fundamentais para aguentar o inverno.

Quando a minha vinda para a Suécia se confirmou a princício eu viria sozinho, felizmente mudamos de idéia. Teresa largou tudo no Brasil, emprego, família, um apartamento e veio passar frio e fazer inúmeras mudanças. Tenho certeza absoluta que não conseguiria passar por isso tudo sem você. Teresa muito obrigado por tudo. Eu te amo muito.

References

[1] D. Schüler, M. Buchert, R. Liu, G. S. Dittrich, and C. Merz. Study on rare earths and their recycling. 2011.

[2] A. Einstein. Über einen die erzeugung und verwandlung des lichtes betreffenden heuristischen gesichtspunkt. *Annalen der Physik*, 322:132, 1905.

[3] I. L. de Broglie. A tentative theory of light quanta. *Phil.Mag.*, 47:411, 1924.

[4] E. Schrödinger. Quantisierung als eigenwertproblem. *Annalen der Physik*, 385:437, 1926.

[5] M. E. Peskin and D. V. Schroeder. *An Introduction To Quantum Field Theory (Frontiers in Physics)*. Westview Press, 1995.

[6] P A M Dirac. The Quantum Theory of the Electron. *Proceedings of the Royal Society A: Mathematical, Physical and Engineering Sciences*, 117:610, 1928.

[7] J. Kübler. *Theory of Itinerant Electron Magnetism*. Oxford Press, 1995.

[8] R. M. Martin. *Electronic Structure : Basic Theory and Practical Methods*. Cambridge University Press, 2008.

[9] M. Born and R. Oppenheimer. Zur quantentheorie der molekeln. *Annalen der Physik*, 389:457, 1927.

[10] Carl Eckart. The kinetic energy of polyatomic molecules. *Phys. Rev.*, 46:383, 1934.

[11] R. G. Parr and W. Yang. *Density-Functional Theory of Atoms and Molecules*. Oxford University Press, 1995.

[12] D. M. Vianna, A. Fazzio, and S. Canuto. *Teoria quantica de sólidos e moléculas*. Livraria da Fisica, 2004.

[13] E. Fermi. Un Metodo Statistico per la determinazione di Alcune priorieta dell' atome. *Rend. Accad. Naz. Lincei*, 6:602, 1927.

[14] L. H. Thomas. The calculation of atomic fields. *Mathematical Proceedings of the Cambridge Philosophical Society*, 23:542, 1927.

[15] P. Hohenberg and W Kohn. Inhomogeneous electron gas. *Phys Rev*, 136:B864, 1964.

[16] W Kohn. Enrico Fermi. *Proceedings of the International School of Physics*, Course LXXXIX:4, 1985.

[17] W. Kohn and L. J. Sham. Self-consistent equations including exchange and correlation effects. *Phys. Rev.*, 140:A1133, 1965.

[18] D. M. Ceperley and B. J. Alder. Ground state of the electron gas by a stochastic method. *Phys. Rev. Lett.*, 45:566, 1980.

[19] J. P. Perdew and A. Zunger. Self-interaction correction to density-functional approximations for many-electron systems. *Phys. Rev. B*, 23:5048, 1981.

[20] J. Perdew, K. Burke, and M. Ernzerhof. Generalized gradient approximation made simple. *Phys. Rev. Lett.*, 77:3865, 1996.

[21] O. K. Andersen. Linear methods in band theory. *Phys. Rev. B*, 12:3060, 1975.

[22] H. L. Skriver. *The LMTO Method*. Springer-Verlag, 1984.

[23] S. Frota-Pessoâ. First-principles real-space linear-muffin-tin-orbital calculations of 3 d impurities in Cu. *Phys. Rev. B*, 46:14570, 1992.

[24] T. Morya. *Spin Fluctuations in Itinerant Spin Electron Magnetism*. Springer-Verlag, 1985.

[25] A.I. Liechtenstein, M.I. Katsnelson, V.P. Antropov, and V.A. Gubanov. Local spin density functional approach to the theory of exchange interactions in ferromagnetic metals and alloys. *J. Mag. and Mag. Mat.*, 67:65, 1987.

[26] L. Szunyogh J. Zabloudil, R. Hammerling and P. Weinberger. *Electron Scattering in Solid Matter*. Springer-Verlag, 2005.

[27] S. Frota-Pessoa, R. B. Muniz, and J. Kudrnovsky. Exchange coupling in transition-metal ferromagnets. *Phys. Rev. B*, 62:5293, 2000.

[28] F. López-Aguilar and J. Costa-Quintana. A first-principles pseudopotential model for the strong intrasite interaction applied to the 4f13 configuration (yb2o3). *physica status solidi (b)*, 123:219, 1984.

[29] J. P. Perdew and A. Zunger. Self-interaction correction to density-functional approximations for many-electron systems. *Phys. Rev. B*, 23:5048, 1981.

[30] V. I. Anisimov, J. Zaanen, and O. K. Andersen. Band theory and mott insulators: Hubbard U instead of stoner I. *Phys. Rev. B*, 44:943, 1991.

[31] V. I. Anisimov and O. Gunnarsson. Density-functional calculation of effective coulomb interactions in metals. *Phys. Rev. B*, 43:7570, 1991.

[32] F. Aryasetiawan, M. Imada, A. Georges, G. Kotliar, S. Biermann, and A. I. Lichtenstein. Frequency-dependent local interactions and low-energy effective models from electronic structure calculations. *Phys. Rev. B*, 70:195104, 2004.

[33] O. Gunnarsson. Calculation of parameters in model hamiltonians. *Phys. Rev. B*, 41:514, 1990.

[34] J. Hubbard. Electron correlations in narrow energy bands. *Proc. Roy. Soc. A*, 276:238, 1963.

[35] J. Hubbard. Electron correlations in narrow energy bands. ii. the degenerate band case. *Proc. Roy. Soc. A*, 277:237, 1964.

[36] J. Hubbard. Electron correlations in narrow energy bands. iii. an improved solution. *Proc. Roy. Soc. A*, 281:401, 1964.

[37] J. W Negele and H. Orland. *Quantum Many-Particle Systems.* Addison-Wesley, 1988.

[38] Quasiparticle calculations in solids. volume 54 of *Solid State Physics.* Academic Press, 1999.

[39] L. Hedin. New method for calculating the one-particle green's function with application to the electron-gas problem. *Phys. Rev.*, 139:A796, 1965.

[40] M. Casula, A. Rubtsov, and S. Biermann. Dynamical screening effects in correlated materials: Plasmon satellites and spectral weight transfers from a green's function ansatz to extended dynamical mean field theory. *Phys. Rev. B*, 85:035115, 2012.

[41] W. Metzner and D. Vollhardt. Correlated lattice fermions in $d = \infty$ dimensions. *Phys. Rev. Lett.*, 62:324, 1989.

[42] A. Georges, G. Kotliar, W. Krauth, and M. J. Rozenberg. Dynamical mean-field theory of strongly correlated fermion systems and the limit of infinite dimensions. *Rev. Mod. Phys.*, 68:13, 1996.

[43] K. Held. Electronic structure calculations using dynamical mean field theory. *Advances in Physics*, 56:829, 2007.

[44] G. Kotliar, S. Y. Savrasov, K. Haule, V. S. Oudovenko, O. Parcollet, and C. A. Marianetti. Electronic structure calculations with dynamical mean-field theory. *Rev. Mod. Phys.*, 78:865, 2006.

[45] P. W. Anderson. Localized magnetic states in metals. *Phys. Rev.*, 124:41, 1961.

[46] O. Grånäs. *Theoretical Studies of Magnetism and Electron Correlation.* Acta Universitatis Upsaliensis Uppsala, 2012.

[47] J. M. D. Coey, editor. *Rare-Earth Iron Permanent Magnets.* Oxford University Press, 1996.

[48] D. Kramer. Concern grows over China's dominance of rare-earth metals. *Phys. Today*, 63:22, 2010.

[49] B. Sanyal, C. Antoniak, T. Burkert, B. Krumme, A. Warland, F. Stromberg, C. Praetorius, K. Fauth, H. Wende, and O. Eriksson. Forcing Ferromagnetic Coupling Between Rare-Earth-Metal and 3d Ferromagnetic Films. *Phys. Rev. Lett.*, 104, 2010.

[50] S. Bhandary, O. Grånäs, L. Szunyogh, B. Sanyal, L. Nordström, and O. Eriksson. Route towards finding large magnetic anisotropy in nanocomposites: Application to a W_(1-x)Re_(x)/Fe multilayer. *Phys. Rev. B*, 84, 2011.

[51] T. Burkert, O. Eriksson, S. Simak, A. Ruban, B. Sanyal, L. Nordström, and J. Wills. Magnetic anisotropy of L$_{10}$ FePt and Fe$_{(1-x)}$Mn$_{(x)}$Pt. *Phys. Rev. B*, 71:134411, 2005.

[52] G. Daalderop, P. J. Kelly, and M. F. H. Schuurmans. Magnetocrystalline anisotropy and orbital moments in transition-metal compounds. *Phys. Rev. B*, 44:12054, 1991.

[53] J. B. Staunton, S. Ostanin, S. S. A. Razee, B. Gyorffy, L. Szunyogh, B. Ginatempo, and E. Bruno. Long-range chemical order effects upon the magnetic anisotropy of FePt alloys from an *ab initio* electronic structure theory. *J. Phys.: Condens. Matter*, 16:S5623, 2004.

[54] S. Sun, C. B. Murray, D. Weller, L. Folks, and A. Moser. Monodisperse FePt Nanoparticles and Ferromagnetic FePt Nanocrystal Superlattices. *Science*, 287:1989, 2000.

[55] T. Burkert, L. Nordström, O. Eriksson, and O. Heinonen. Giant Magnetic Anisotropy in Tetragonal FeCo Alloys. *Phys. Rev. Lett.*, 93:027203, 2004.

[56] G. Andersson, T. Burkert, P. Warnicke, M. Björck, B. Sanyal, C. Chacon, C. Zlotea, L. Nordström, P. Nordblad, and O. Eriksson. Perpendicular Magnetocrystalline Anisotropy in Tetragonally Distorted Fe-Co Alloys. *Phys. Rev. Lett.*, 96:037205, 2006.

[57] Chad D. Graham Sõshin Chikazumi. Physics of ferromagnetism. *Oxford Science Publication*, 1999.

[58] J. M. D. Coey and R. Skomski, editors. *Permanent Magnetism*. Studies in Condensed Matter Physics. Taylor and Francis, 1999.

[59] H. Brooks. Ferromagnetic Anisotropy and the itinerant electron model. *Phys. Rev.*, 58:909, 1940.

[60] C. T. Chen, Y. U. Idzerda, H. J. Lin, N. V. Smith, and G. Meigs. Experimental Confirmation of the X-Ray Magnetic Circular Dichroism Sum Rules for Iron and Cobalt. *Phys. Rev. Lett.*, 75:152, 1995.

[61] S. Rundqvist and F. Jellinek. The Structures of Ni6Si2B, Fe_2P and Related Phases. *Acta Chemica Scandinavica*, 13:425, 1959.

[62] B. Carlsson, M. Gölin, and S. Rundqvist. Determination of the homogeneity range and refinement of the crystal structure of Fe_2P. *J. Solid State Chem.*, 8:57, 1973.

[63] H. Fujii, S. Komura, T. Takeda, and T. Okamoto. Polarized neutron diffraction study of Fe_2P single crystal. *Journal of the Physical Society of Japan*, 46, 1979.

[64] P. Dera, B. Lavina, L. A. Borkowski, V. B. Prakapenka, S. R. Sutton, M. L. Rivers, R. T. Downs, N. Z. Boctor, and C. T. Prewitt. High-pressure polymorphism of Fe_2P and its implications for meteorites and Earth's core. *Geophys. Res. Lett.*, 35:L10301, 2008.

[65] H. Scott, B. Kiefer, C. D. Martin, N. Boateng, M. Frank, and Y. Meng. P-V equation of state for Fe_2P and pressure-induced phase transition in Fe_3P. *High Pressure Research*, 28:375, 2008.

[66] R. Chandra, S. Bjarman, and T. Ericsson. A Mössbauer and X-ray study of $Fe_2P_{(1-x)}B_{(x)}$ compounds (x < 0.15). *Journal of Solid State*

Chemistry, 34:389, 1980.

[67] O. Eriksson and A. Svane. Isomer shifts and hyperfine fields in iron compounds. *J. Phys.: Condens. Matter*, 1:1589, 1989.

[68] H. Fujji, T. Hokabe, T. Kamigaichi, and T. Okamoto. Magnetic-Properties of Fe_2P Single-Crystal. *J. Phys. Soc. Jpn.*, 43:41, 1977.

[69] R. Wappling, L. Häggström, T. Ericsson, S. Devanarayanan, E. Karlsson, B. Carlsson, and S. Rundqvist. First-Order Magnetic Transition, Magnetic-Structure, and Vacancy Distribution in Fe_2P. *J. Solid State Chem.*, 13:258, 1975.

[70] T. Moriya and K. Usami. Coexistence of ferro-and antiferromagnetism and phase transitions in itinerant electron systems. *Solid State Communications*, 23:935, 1977.

[71] E. P. Wohlfarth. First and second order transitions in some metallic ferromagnets. *J. Appl. Phys.*, 50(B11):7542, 1979.

[72] O. Eriksson, J. Sjöström, B. Johansson, L. Häggström, and H. L. Skriver. Itinerant ferromagnetism in Fe_2P. *J. Magn. Magn. Mater.*, 74:347, 1988.

[73] S. Ishida, S. Asano, and J. Ishida. Electronic-Structures and Magnetic-Properties of Mn2p, Fe_2P, Ni_2P. *J. Phys. F. Met. Phys.*, 17:475, 1987.

[74] K. H. J. Buschow, editor. volume 6 of *Handbook of Magnetic Materials*. Elsevier, 1991.

[75] H. Fujii, .T Hokabe, T. Kamigaichi, and T. Okamoto. Magnetic Properties of Fe_2P Single Crystal. *J. Phys. Soc. Jpn.*, 43:41, 1977.

[76] D. Scheerlinck and E. Legrand. Neutron diffraction study of the magnetic structure of Fe_2P. *Solid State Communications*, 25:181, 1978.

[77] M I Katsnelson and A I Lichtenstein. Lda++ approach to the electronic structure of magnets: correlation effects in iron. *Journal of Physics: Condensed Matter*, 11:1037, 1999.

[78] J. Braun, J. Minár, H. Ebert, M. I. Katsnelson, and A. I. Lichtenstein. Spectral function of ferromagnetic $3d$ metals: A self-consistent LSDA + DMFT approach combined with the one-step model of photoemission. *Phys. Rev. Lett.*, 97:227601, 2006.

[79] H. J. F. Jansen. Magnetic anisotropy in density-functional theory. *Phys. Rev. B*, 59:4699, 1999.

[80] C. Andersson, B. Sanyal, O. Eriksson, L. Nordström, O. Karis, D. Arvanitis, T. Konishi, E. Holub-Krappe, and J. Dunn. Influence of ligand states on the relationship between orbital moment and magnetocrystalline anisotropy. *Phys. Rev. Lett.*, 99, 2007.

[81] J. Trygg, B. Johansson, O. Eriksson, and J. M. Wills. Total-Energy Calculation of the Magnetocrystalline Anisotropy Energy in the Ferromagnetic 3d Metals. *Phys. Rev. Lett.*, 75:2871, 1995.

[82] D. Wang, R. Wu, and A. J. Freeman. First-principles theory of surface magnetocrystalline anisotropy and the diatomic-pair model. *Phys. Rev. B*, 47(22):14932, 1993.

[83] C. Abache and J. Oesterreicher. Magnetic anisotropies and spin reorientations of $R_2Fe_{14}B$-type compounds. *J. Appl. Phys.*, 60:3671, 1986.

[84] V. Moggi-Cecchi, G. Pratesi, and L. Mancini. NWA 1052 and NWA 1054: two new primitive achondrites from north west africa, 2005. XXXVI Lunar and Planetary Sciences Conference, abstract 1808.

[85] P. Pratesi, L. Bindi, and V. Moggi-Cecchi. Icosahedral coordination of phosphorus in the crystal structure of melliniite, a new phosphide mineral from the Northwest Africa 1054 acapulcoite. *Am. Mineral.*, 91:451, 2006.

[86] S. N. Britvin, N. S. Rudashevsky, S. V. Krivovichev, P. C. Burns, and Y. S. Polekhovsky. Allabogdanite, $(Fe,Ni)_2P$, a new mineral from the Onello meteorite: The occurrence and crystal structure. *Am. Mineral.*, 87:1245, 2002.

[87] S. Rundqvist. Binary transition metal phosphides and crystal-chemical relations between them and transition metal compounds with other nonmetals of small atomic radius. *Ark. Kemi.*, 20:67, 1962.

[88] M. A. Pasek, V. D. Smith, and D. S. Lauretta. Meteorites as a supplement and/or source of phosphorus for the origin of life. *Abstr. Pap. Am. Chem. Soc.*, 228:34, 2004. 228th National Meeting of the American-Chemical-Society, Philadelphia, PA, AUG 22-26, 2004.

[89] S. N. Britvin, V. D. Kolomensky, M. M. Boldyreva, A. N. Bogdanova, Yu L Kretser, O N Boldyreva, and N S Rudashevskii. Nickelphosphide, $(Ni,Fe)_3P$, the nickel analog of schreibersite. *Proc. Russian Mineral. Soc.*, 128:64, 1999.

[90] P. R. Buseck. Phosphide from meteorites: Barringerite, a new iron-nickel mineral. *Science*, 165:169, 1969.

[91] A. V. Ivanov, M. E. Zolensky, A. Saito, K. Ohsumi, S. V. Yang, N. N. Kononkova, and T. Mikouchi. Florenskyite, FeTiP, a new phosphide from the Kaidun meteorite. *Am. Mineral.*, 85:1082, 2000.

[92] J. L. Calais. Band-structure of transition-metal compounds. *Adv. Phys.*, 26:847, 1977.

[93] A. Neckel. Recent investigations on the electronic-structure of the 4th-group and 5th-group transition-metal monocarbides, mononitrides, and monoxides. *Int. J. Quantum Chem.*, 23:1317, 1983.

[94] K. Schwarz. Band-structure and chemical bonding in transition-metal carbides and nitrides. *CRC Crit. Rev. Solid State Mat. Sci.*, 13:211, 1987.

[95] L. I. Johansson. Electronic and structural-properties of transition-metal carbide and nitride surfaces. *Surf. Sci. Rep.*, 21:179, 1995.

[96] W. S. Williams. Physics of transition-metal carbides. *Mat. Sci. Eng. A*, 105:1, 1988.

[97] C. D. Gelatt, A. R. Williams, and V. L. Moruzzi. Theory of bonding of transition metals to nontransition metals. *Phys. Rev. B*, 27:2005, 1983.

[98] J. Zhao, Q. Huang, C. de la Cruz, S. Li, J. W. Lynn, Y. Chen, M. A. Green, G. F. Chen, G. Li, Z. Li, J. L. Luo, N. L. Wang, and P. Dai. Structural and magnetic phase diagram of $CeFeAsO_{1-x}F_x$ and its relation to high-temperature superconductivity. *Nature Mat.*, 7:953, 2008.

[99] O. Tegus, E. Brück. H. J. Buschow, and F. R. de Boer. Transition-metal-based magnetic refrigerants for room-temperature applications. *Nature*, 415:150, 2002.

[100] A. Grechnev, R. Ahuja, and O. Eriksson. Balanced crystal orbital overlap population - a tool for analysing chemical bonds in solids. *J. Phys. Cond. Mat.*, 15:7751, 2003.

[101] T. Hughbanks and R. Hoffmann. Chains of trans-edge-sharing molybdenum octahedra: metal-metal bonding in extended systems. *J. Am. Chem. Soc.*, 105:3528, 1983.

[102] J. P. Perdew, A. Ruzsinszky, G. I. Csonka, O. A. Vydrov, G. E. Scuseria, L. A. Constantin, X. Zhou, and K. Burke. Restoring the density-gradient expansion for exchange in solids and surfaces. *Phys. Rev. Lett.*, 100:136406, 2008.

[103] L. Vitos, H. L. Skriver, B. Johansson, and J. Kollár. Application of the exact muffin-tin orbitals theory: the spherical cell approximation. *Comp. Mat. Sci.*, 18:24, 2000.

[104] L. Vitos. Total-energy method based on the exact muffin-tin orbitals theory. *Phys. Rev. B*, 64:014107, 2001.

[105] O. K. Andersen, O. Jepsen, and G. Krier. *in: V. Kumar, O. K. Andersen, A. Mookerjee, Editors, Lectures on Methods of Electronic Structure Calculation.* World Scientific, Singapore, 1994. pp. 63-124.

[106] P. Soven. Coherent-potential model of substitutional disordered alloys. *Phys. Rev.*, 156:809, 1967.

[107] B. L. Gyorffy. Coherent-potential approximation for a nonoverlapping-muffin-tin-potential model of random substitutional alloys. *Phys. Rev. B*, 5:2382, 1972.

[108] L. Vitos, I.A. Abrikosov, and B. Johansson. Anisotropic lattice distortions in random alloys from first-principles theory. *Phys. Rev. Lett.*, 87:156401, 2001.

[109] K. Kádas, L. Vitos, B. Johansson, and R. Ahuja. Stability of body-centered cubic iron-magnesium alloys in the Earth's inner core. *Proc. Natl. Acad. Sci. USA*, 106:15560, 2009.

[110] S. Rundqvist. X-ray investigations of ternary system Fe-P-B - Some features of systems Cr-P-B, Mn-P-B, Co-P-B and Ni-P-B. *Acta Chem.*

Scand., 16:1–19, 1962.

[111] R Skála and M Drábek. Powder data for synthetic analogue of a mineral nickelphosphide. *Powder Diffr.*, 17:322, 2002.

[112] P. Franke and D. Neuschütz. *Fe-P*, volume 19B3. SpringerMaterials - The Landolt-Börnstein Database, 2011.

[113] K J Lee and P Nash. *Ni-P (Nickel-Phosphorus) in: Binary Alloy Phase Diagrams.* Materials Park, Ohio: ASM International, Ohio, 1990.

[114] H. Okamoto. Ni-P (Nickel-Phosphorus). *J. Phase Equilib.*, 21:210, 2000.

[115] H. L. Skriver. Crystal structure from one-electron theory. *Phys. Rev. B*, 31:1909, 1985.

[116] S. Foner, E. J. McNiff, and V. Sadagopan. Magnetic Moment of $ZrZn_2$ up to 150 kG: is "Pure" $ZrZn_2$ Ferromagnetic? *Phys. Rev. Lett.*, 19:1233, 1967.

[117] S. Ogawa and N. Sakamoto. Magnetic Properties of $ZrZn_2$—Itinerant Electron Ferromagnet. *Journal of the Physical Society of Japan*, 22:1214, 1967.

[118] K. Schwarz and P. Mohn. Itinerant metamagnetism in YCO_2. *Journal of Physics F: Metal Physics*, 14:L129, 1984.

[119] G G Low and T M Holden. Distribution of the ferromagnetic polarization induced by iron and cobalt atoms in palladium. *Proceedings of the Physical Society*, 89:119, 1966.

[120] G. Nieuwenhuys. Magnetic behavior of cobalt, iron and manganese dissolved in palladium. *Advances in Physics*, 24:515, 1975.

[121] M. Pärnaste, M. Marcellini, E. Holmström, N. Bock, J. Fransson, O. Eriksson, and B. Hjörvarsson. Dimensionality crossover in the induced magnetization of Pd layers. *Journal of Physics: Condensed Matter*, 19:246213, 2007.

[122] E. Wigner. Effects of the electron interaction on the energy levels of electrons in metals. *Trans. Farad. Soc.*, 34:678, 1938.

[123] A. W. Overhauser. Charge-density waves and isotropic metals. *Adv. Phys.*, 27:343, 1978.

[124] D. Garrett G. Bergmann, D. Frank. Super strong effect of surface impurities on the resistance and Hall effect of quench condensed Cs films. *Eur. Phys. J. B*, 5:345, 1998.

[125] Weak localization in thin Cs films, author = Beckmann, H. and Fulmer, T. and Garrett, D. and Hossain, M. and Bergmann, G. *Phys. Rev. B*, 59:7724, 1999.

[126] D. Riegel, H. J. Barth, L. Büermann, H. Haas, and Ch. Stenzel. Fully Localized 3d-Shell Behavior of Fe Ions in Alkali-Metal Hosts. *Phys. Rev. Lett.*, 57:388, 1986.

[127] M. Hossain and G. Bergmann. Giant moments of Fe and Co on and in rubidium aaand potassium films. *The European Physical Journal B -*

126

Condensed Matter and Complex Systems, 26:7, 2002.

[128] M. Gruyters and D. Riegel. Comment on "Mystery of the Alkali Metals: Giant Moments of Fe and Co on and in Cs Films". *Phys. Rev. Lett.*, 85:1582, 2000.

[129] P. Mohn, P. Weinberger, B. Ujfalussy, O. Eriksson, G. Gutierrez, R. Ahuja, and B. Johansson. Comment on "Mystery of the Alkali Metals: Giant Moments of Fe and Co on and in Cs Films". *Phys. Rev. Lett.*, 85:1583, 2000.

[130] G. Y. Guo. Giant orbital moments of Fe and Co in alkali metals Cs, Rb, and K. *Phys. Rev. B*, 62:R14609, 2000.

[131] C. Carbone, M. Veronese, P. Moras, S. Gardonio, C. Grazioli, P. H. Zhou, O. Rader, A. Varykhalov, C. Krull, T. Balashov, A. Mugarza, P. Gambardella, S. Lebègue, O. Eriksson, M. I. Katsnelson, and A. I. Lichtenstein. Correlated Electrons Step by Step: Itinerant-to-Localized Transition of Fe Impurities in Free-Electron Metal Hosts. *Phys. Rev. Lett.*, 104:117601, 2010.

[132] C. Ortiz, O. Eriksson, and M. Klintenberg. Data mining and accelerated electronic structure theory as a tool in the search for new functional materials. *Computational Materials Science*, 44:1042, 2009.

[133] J. M. Wills and B. R. Cooper. Synthesis of band and model Hamiltonian theory for hybridizing cerium systems. *Phys. Rev. B*, 36:3809, 1987.

[134] J. M. Wills, M. Alouani, P. Andersson, A. Delin, O. Eriksson, and A. Grechnev. *Full-Potential Electronic Structure Method, Energy and Force Calculations with Density Functional and Dynamical Mean Field Theory*, volume 167. Springer Series in Solid-State Sciences, 2010.

[135] A. Grechnev, I. Di Marco, M. I. Katsnelson, A. I. Lichtenstein, John Wills, and Olle Eriksson. Theory of bulk and surface quasiparticle spectra for Fe, Co, and Ni. *Phys. Rev. B*, 76:035107, 2007.

[136] P. Thunström, I. Di Marco, A. Grechnev, S. Lebègue, M. I. Katsnelson, A. Svane, and O. Eriksson. Multiplet effects in the electronic structure of intermediate-valence compounds. *Phys. Rev. B*, 79:165104, 2009.

[137] O. Grånäs, I. Di Marco, P. Thunström, L. Nordström, O. Eriksson, T. Björkman, and J.M. Wills. Charge self-consistent dynamical mean-field theory based on the full-potential linear muffin-tin orbital method: Methodology and applications. *Computational Materials Science*, 55:295, 2012.

[138] A. I. Lichtenstein and M. I. Katsnelson. Ab initio calculations of quasiparticle band structure in correlated systems: LDA++ approach. *Phys. Rev. B*, 57:6884, 1998.

[139] P. Thunström, I. Di Marco, and O. Eriksson. Electronic entanglement in late transition metal oxides. *http://arxiv.org/abs/1202.3975v1*, 2012.

[140] M. Zheng, J. Shen, J. Barthel, P. Ohresser, Ch. V. Mohan, and J. Kirschner. Growth, structure and magnetic properties of Co ultrathin

films on Cu(111) by pulsed laser deposition. *Journal of Physics: Condensed Matter*, 12:783, 2000.

[141] P. Mavropoulos, S. Lounis, and S. Blügel. Exchange coupling in transition-metal nanoclusters on Cu(001) and Cu(111) surfaces. *phys. stat. sol. (b)*, 247:1187, 2010.

[142] S. Lounis, Ph. Mavropoulos, P. H. Dederichs, and S. Blügel. Noncollinear Korringa-Kohn-Rostoker Green function method: Application to 3d nanostructures on Ni(001). *Phys. Rev. B*, 72:224437, 2005.

[143] S. T. Bramwell and M. J. P. Gingras. Spin Ice State in Frustrated Magnetic Pyrochlore Materials. *Science*, 294:1495, 2001.

[144] A. J. Heinrich, J. A. Gupta, C. P. Lutz, and D. M. Eigler. Single-Atom Spin-Flip Spectroscopy. *Science*, 306:466, 2004.

[145] Anders Bergman, Lars Nordström, Angela Burlamaqui Klautau, Sonia Frota-Pessôa, and Olle Eriksson. Magnetic structures of small Fe, Mn, and Cr clusters supported on Cu(111): Noncollinear first-principles calculations. *Phys. Rev. B*, 75:224425, 2007.

[146] W. Wulfhekel and C. L. Gao. Investigation of non-collinear spin states with scanning tunneling microscopy. *Journal of Physics: Condensed Matter*, 22:084021, 2010.

[147] M. Uhl, L. M. Sandratskii, and J. Kübler. Spin fluctuations in γ-Fe and in Fe$_3$Pt Invar from local-density-functional calculations. *Phys. Rev. B*, 50:291, 1994.

[148] R. Lorenz and J. Hafner. Noncollinear magnetic structures in amorphous iron and iron-based alloys. *Journal of Magnetism and Magnetic Materials*, 139:209, 1995.

[149] Y. Kakehashi, S. Akbar, and N. Kimura. Molecular-dynamics approach to itinerant magnetism with complex magnetic structures. *Phys. Rev. B*, 57:8354, 1998.

[150] T. C. Schulthess, W. H. Butler, G. M. Stocks, S. Maat, and G. J. Mankey. Noncollinear magnetism in substitutionally disordered face-centered-cubic FeMn. *Journal of Applied Physics*, 85:4842, 1999.

[151] A. Sakuma. First-Principles Study on the Non-Collinear Magnetic Structures of Disordered Alloys. *Journal of the Physical Society of Japan*, 69:3072, 2000.

[152] A. Mookerjee. Averaged density of states in disordered systems. *Journal of Physics C: Solid State Physics*, 6:1340, 1973.

[153] A. Mookerjee. The Economou-Cohen localization criterion: effect of clusters and a reappraisal. *Journal of Physics C: Solid State Physics*, 7:4069, 1974.

[154] S. S. A. Razee, A. Mookerjee, and R. Prasad. On the augmented-space cluster coherent-potential approximation and its analytic properties.

Journal of Physics: Condensed Matter, 3:3301, 1991.

[155] V. Kumar, A. Mookerjee, and V. K. Srivastava. Electronic structure of disordered alloys I. Self-consistent cluster CPA incorporating off-diagonal disorder and short-range order. *Journal of Physics C: Solid State Physics*, 15:1939, 1982.

[156] A. Mookerjee and R. Prasad. Generalized augmented-space theorem for correlated disorder and the cluster-coherent-potential approximation. *Phys. Rev. B*, 48:17724, 1993.

[157] T. Saha, I. Dasgupta, and A. Mookerjee. Augmented-space recursive method for the study of short-ranged ordering effects in binary alloys. *Phys. Rev. B*, 50:13267, 1994.

[158] A. Chakrabarti and A. Mookerjee. Augmented-space recursion for partially disordered systems. *Journal of Physics: Condensed Matter*, 13:10149, 2001.

[159] T. Saha and A. Mookerjee. The effects of local lattice distortion in non-isochoric alloys: CuPd and CuBe. *Journal of Physics: Condensed Matter*, 8:2915, 1996.

[160] J. Kubler, K. H. Hock, J. Sticht, and A. R Williams. Density functional theory of non-collinear magnetism. *Journal of Physics F: Metal Physics*, 18:469, 1988.

[161] F. F. Bertaut and D. Fruchart. Magnetic moment rotation of manganese in Mn_3NiN. *Int. J. Magn.*, 2:259, 1972.

[162] A. Sakuma. Electronic structures and magnetism of cuau-type mnni and mnga. *Journal of Magnetism and Magnetic Materials*, 187:105, 1998.

[163] A. Sakuma, R. Y. Umetsu, and K. Fukamichi. Magnetic structures and their stability in Mn_3Rh ordered and disordered alloys. *Phys. Rev. B*, 66:014432, 2002.

[164] S. Ghosh, N. Das, and A. Mookerjee. *Int. J. Mod. Phys. B*, 21:723, 1999.

[165] E. Beaurepaire, J.-C. Merle, A. Daunois, and J.-Y. Bigot. Ultrafast Spin Dynamics in Ferromagnetic Nickel. *Phys. Rev. Lett.*, 76:4250, 1996.

[166] K. Vahaplar, A. M. Kalashnikova, A. V. Kimel, D. Hinzke, U. Nowak, R. Chantrell, A. Tsukamoto, A. Itoh, A. Kirilyuk, and Th. Rasing. Ultrafast Path for Optical Magnetization Reversal via a Strongly Nonequilibrium State. *Phys. Rev. Lett.*, 103:117201, 2009.

[167] Sebastian Loth, Susanne Baumann, Christopher P. Lutz, D. M. Eigler, and Andreas J. Heinrich. Bistability in Atomic-Scale Antiferromagnets. *Science*, 335:196, 2012.

[168] G. Malinowski, F. Dalla Longa, J. H. H. Rietjens, P. V. Paluskar, R. Huijink, H. J. M. Swagten, and B. Koopmans. Control of speed and efficiency of ultrafast demagnetization by direct transfer of spin angular momentum. *Nat. Phys.*, 4:855, 2008.

[169] J.-Y. Bigot, M. Vomir, and E. Beaurepaire. Coherent ultrafast magnetism induced by femtosecond laser pulses. *Nat. Phys.*, 5:515, 2009.

[170] C. Stamm, N. Pontius, T. Kachel, M. Wietstruk, and H. A. Dürr. Femtosecond x-ray absorption spectroscopy of spin and orbital angular momentum in photoexcited Ni films during ultrafast demagnetization. *Phys. Rev. B*, 81:104425, 2010.

[171] C Boeglin, E Beaurepaire, V Halté, V López-Flores, C Stamm, N Pontius, H A Dürr, and J Y Bigot. Distinguishing the ultrafast dynamics of spin and orbital moments in solids. *Nature*, 2010.

[172] Satadeep Bhattacharjee, Anders Bergman, Andrea Taroni, Johan Hellsvik, Biplab Sanyal, and Olle Eriksson. Theoretical Analysis of Inertia-like Switching in Magnets: Applications to a Synthetic Antiferromagnet. *Phys. Rev. X*, 2:011013, 2012.

[173] Andrea Taroni, Anders Bergman, Lars Bergqvist, Johan Hellsvik, and Olle Eriksson. Suppression of Standing Spin Waves in Low-Dimensional Ferromagnets. *Phys. Rev. Lett.*, 107:037202, 2011.

[174] K. Vahaplar, A. M. Kalashnikova, A. V. Kimel, D. Hinzke, U. Nowak, R. Chantrell, A. Tsukamoto, A. Itoh, A. Kirilyuk, and Th. Rasing. Ultrafast Path for Optical Magnetization Reversal via a Strongly Nonequilibrium State. *Phys. Rev. Lett.*, 103:117201, 2009.

[175] S. Krause, G. Herzog, A. Schlenhoff, A. Sonntag, and R. Wiesendanger. Joule Heating and Spin-Transfer Torque Investigated on the Atomic Scale Using a Spin-Polarized Scanning Tunneling Microscope. *Phys. Rev. Lett.*, 107:186601, 2011.

[176] S. Krause, G. Herzog, T. Stapelfeldt, L. Berbil-Bautista, M. Bode, E. Y. Vedmedenko, and R. Wiesendanger. Magnetization Reversal of Nanoscale Islands: How Size and Shape Affect the Arrhenius Prefactor. *Phys. Rev. Lett.*, 103:127202, 2009.

[177] Anders Bergman, Björn Skubic, Johan Hellsvik, Lars Nordström, Anna Delin, and Olle Eriksson. Ultrafast switching in a synthetic antiferromagnetic magnetic random-access memory device. *Phys. Rev. B*, 83:224429, 2011.

[178] D Böttcher, A Ernst, and J Henk. Atomistic magnetization dynamics in nanostructures based on first principles calculations: application to Co nanoislands on Cu(111). *Journal of Physics: Condensed Matter*, 23:296003, 2011.

[179] C. Haase and U. Nowak. Role of dipole-dipole interactions for hyperthermia heating of magnetic nanoparticle ensembles. *Phys. Rev. B*, 85:045435, 2012.

[180] J. Hellsvik, B. Skubic, L. Nordström, and O. Eriksson. Simulation of a spin-wave instability from atomistic spin dynamics. *Phys. Rev. B*, 79:184426, 2009.

[181] Alexander Ako Khajetoorians, Jens Wiebe, Bruno Chilian, and Roland Wiesendanger. Realizing All-SpinÐBased Logic Operations Atom by Atom. *Science*, 332:1062, 2011.

[182] J.Stöhr and H.C.Siegmann. Magnetism: from fundamentals to nanoscale dynamics. *Springer*, 2008.

[183] Daniel J. Lacks. Energy Landscapes and the Non-Newtonian Viscosity of Liquids and Glasses. *Phys. Rev. Lett.*, 87:225502, 2001.

[184] U. Leonhardt. *Nature Photonics*, 1:207, 2009.

[185] H. Oka, P. A. Ignatiev, S. Wedekind, G. Rodary, L. Niebergall, V. S. Stepanyuk, D. Sander, and J. Kirschner. Spin-Dependent Quantum Interference Within a Single Magnetic Nanostructure. *Science*, 327:843, 2010.

[186] S. Rusponi, T. Cren, N. Weiss, M. Epple, P. Buluschek, L. Claude, and H. Brune. The remarkable difference between surface and step atoms in the magnetic anisotropy of two-dimensional nanostructures. *Nature Materials*, 2:546, 2003.

[187] B Skubic, J Hellsvik, L Nordström, and O Eriksson. A method for atomistic spin dynamics simulations: implementation and examples. *Journal of Physics: Condensed Matter*, 20:315203, 2008.

[188] E. C. Stoner and E. P. Wohlfarth. A Mechanism of Magnetic Hysteresis in Heterogeneous Alloys. *Phil. Trans. R. Soc. London A*, 240:599, 1948.

[189] C. Andersson, B. Sanyal, O. Eriksson, L. Nordström, O. Karis, D. Arvanitis, T. Konishi, E. Holub-Krappe, and J. Hunter Dunn. Influence of Ligand States on the Relationship between Orbital Moment and Magnetocrystalline Anisotropy. *Phys. Rev. Lett.*, 99:177207, 2007.